



IntechOpen

Applications in Water Systems Management and Modeling

Edited by Daniela Malcangio



APPLICATIONS IN WATER SYSTEMS MANAGEMENT AND MODELING

Edited by **Daniela Malcangio**

Applications in Water Systems Management and Modeling

<http://dx.doi.org/10.5772/intechopen.68457>

Edited by Daniela Malcangio

Contributors

Juan Antonio Garcia Aragon, Humberto Salinas Tapia, Victor Diaz Palomarez, Klever Izquierdo-Ayala, Takaaki Uda, Masumi Serizawa, Shiho Miyahara, Lubo Liu, Eyal Brill, Barak Brill, Gurudeo Tularam, Omar Moalin Hassan, Zati Sharip, Shahirwan Aman Shah, Aminuddin Jamin, Juhaimi Jusoh, Daniela Malcangio

© The Editor(s) and the Author(s) 2018

The rights of the editor(s) and the author(s) have been asserted in accordance with the Copyright, Designs and Patents Act 1988. All rights to the book as a whole are reserved by INTECHOPEN LIMITED. The book as a whole (compilation) cannot be reproduced, distributed or used for commercial or non-commercial purposes without INTECHOPEN LIMITED's written permission. Enquiries concerning the use of the book should be directed to INTECHOPEN LIMITED rights and permissions department (permissions@intechopen.com). Violations are liable to prosecution under the governing Copyright Law.



Individual chapters of this publication are distributed under the terms of the Creative Commons Attribution 3.0 Unported License which permits commercial use, distribution and reproduction of the individual chapters, provided the original author(s) and source publication are appropriately acknowledged. If so indicated, certain images may not be included under the Creative Commons license. In such cases users will need to obtain permission from the license holder to reproduce the material. More details and guidelines concerning content reuse and adaptation can be found at <http://www.intechopen.com/copyright-policy.html>.

Notice

Statements and opinions expressed in the chapters are these of the individual contributors and not necessarily those of the editors or publisher. No responsibility is accepted for the accuracy of information contained in the published chapters. The publisher assumes no responsibility for any damage or injury to persons or property arising out of the use of any materials, instructions, methods or ideas contained in the book.

First published in London, United Kingdom, 2018 by IntechOpen

eBook (PDF) Published by IntechOpen, 2019

IntechOpen is the global imprint of INTECHOPEN LIMITED, registered in England and Wales, registration number: 11086078, The Shard, 25th floor, 32 London Bridge Street
London, SE19SG – United Kingdom

Printed in Croatia

British Library Cataloguing-in-Publication Data

A catalogue record for this book is available from the British Library

Additional hard and PDF copies can be obtained from orders@intechopen.com

Applications in Water Systems Management and Modeling

Edited by Daniela Malcangio

p. cm.

Print ISBN 978-1-78923-044-4

Online ISBN 978-1-78923-045-1

eBook (PDF) ISBN 978-1-83881-321-5

We are IntechOpen, the first native scientific publisher of Open Access books

3,400+

Open access books available

109,000+

International authors and editors

115M+

Downloads

151

Countries delivered to

Our authors are among the
Top 1%

most cited scientists

12.2%

Contributors from top 500 universities



WEB OF SCIENCE™

Selection of our books indexed in the Book Citation Index
in Web of Science™ Core Collection (BKCI)

Interested in publishing with us?
Contact book.department@intechopen.com

Numbers displayed above are based on latest data collected.
For more information visit www.intechopen.com



Meet the editor



Daniela Malcangio is an academic researcher (assistant professor with tenure) in Hydraulics at the Department of Civil, Environmental, Land, Building Engineering and Chemistry (DICATECh), Polytechnic University of Bari, Italy, since May 2012. She graduated in Civil Engineering at the same university in April 2000 with highest grade (110/110). In 2004, she obtained her PhD degree in

Waste Disposal and Environmental Protection from the same university.

Her main research interests include:

- Turbulent jets and plumes
- Hydrodynamic interaction between jets and plumes and vegetation
- Circulation of marine currents offshore and onshore
- Diffusion and dilution of discharges in the sea

She is the author or coauthor of publications on these topics published in international, peer-reviewed ISI-JCR journals, book chapters, and conference proceedings and reviewer for some ISI-JCR journals.

Contents

Preface XI

- Chapter 1 **Introductory Chapter: Applications in Water Systems 1**
Daniela Malcangio
- Chapter 2 **The Effects of Climate Change on Rural-Urban Migration in Sub-Saharan Africa (SSA)—The Cases of Democratic Republic of Congo, Kenya and Niger 3**
Omar Moalin Hassan and Gurudeo Anand Tularam
- Chapter 3 **Identifying Water Network Anomalies Using Multi Parameters Random Walk: Theory and Practice 33**
Eyal Brill and Barak Brill
- Chapter 4 **Segmentation of Water Body and Lakeshore Changes behind an Island Owing to Wind Waves 49**
Takaaki Uda, Masumi Serizawa and Shiho Miyahara
- Chapter 5 **Assessing the Hydrodynamic Pattern in Different Lakes of Malaysia 71**
Zati Sharip, Shahirwan Aman Shah, Aminuddin Jamin and Juhaimi Jusoh
- Chapter 6 **Application of a Hydrodynamic and Water Quality Model for Inland Surface Water Systems 87**
Lubo Liu
- Chapter 7 **Optical Methods Applied to Hydrodynamics of Cohesive Sediments 111**
Juan Antonio Garcia Aragon, Salinas Tapia Humberto, Diaz Palomarez Victor and Klever Izquierdo Ayala

Preface

From a scientific point of view in the general field of hydraulics, the study of natural and artificial water systems is the most widespread approach for the correct management of such a vital resource for the human species as water. However, it is very difficult to give a holistic view of the different reference areas of this kind of study. Indeed, a “holistic approach” means an “integrated” intervention, able to exploit the strengths of different disciplines: physical, biological, chemical, oceanographic, etc. It is an approach that is by nature flexible as it uses different techniques and methodologies, and it is utilized in an extremely wide application field. The difficulty experienced by the operators in studying a process with water as its object is therefore considerable and it requires undoubtedly the collaboration of several figures with different specializations.

This multidisciplinary book has the ambition of bringing together various studies on different water systems to demonstrate the vastness of the topic. In this way, the reader, researcher or professional, can range from one field to another, always having in mind as a guiding thread the matter “water,” with the aim to better comprehend water body modeling techniques and the solution of the most varied problems. It is designed for those working in the field of environmental engineering and environmental sciences to integrate their knowledge on different scientific and practical approaches to water systems, all through practical experience.

Daniela Malcangio, PhD

Department of Civil, Environmental, Land, Building Engineering and Chemistry
(DICATECh)

Polytechnic University of Bari, Italy

Introductory Chapter: Applications in Water Systems

Daniela Malcangio

Additional information is available at the end of the chapter

<http://dx.doi.org/10.5772/intechopen.76639>

1. Introduction

Water is, without doubt, an essential and basic resource for the existence of life on the planet, as it is the primary component of the ecosystem and is used for many purposes, three of which are of main importance, that is, irrigation, industry, and domestic application. Therefore, water security challenges may affect the environmental, economic, and social stability of the world. The seriousness of these conditions highlights the need to examine the impact of climate change acting at the planetary level on water security and people movement. This topic is addressed in Chapter 1, which investigates the effect of rainfall and temperature, which are climate change variables, on water security and people movement in three Sub-Saharan African countries. The study reveals increasing rural-urban migrations in the next decade in the selected countries due to high rainfall variabilities and increasing temperatures, using VAR and granger causality tests. There will be a large number of rural communities leaving from their villages to urban areas due to water availability conditions and poor agricultural production levels, with all that follows.

With the evolution of urbanization, industrialization, and intensive agricultural practices, one of the most damaged natural elements is water, and then the aquatic environment. Therefore, the need to pay more attention to the quality of all types of water bodies including river reaches, lakes, reservoirs, estuaries, and coastal waters, to analyze the effects and locate the causes of their pollution and to manage it, has led to the development of water quality models. Since pollutants, which flow into the water bodies are transferred by both advection and diffusion and react chemically and biologically, the priority is to configure the hydrodynamic processes that occur in the target area. Thus, hydrodynamic models able to simulate circulation and currents are jointly needed. Two different applications of hydrodynamic modeling in similar water bodies, i.e. lakes, are presented in this book. Chapter 2 concerns the study of the effect of wind waves, when the probability of occurrence of the wind direction is given by a circular or elliptic distribution, on the shape of shallow water bodies, initially rectangular or triangular. The segmentation of these water bodies into circular or elliptic lakes is predicted

in each case using the BG model. Chapter 3 aims to improve understanding of the hydrodynamic characteristics in different tropical lakes located in Malaysia, for which current knowledge remains inadequate due to the absence of long-term monitoring data. Chapter 4 focuses on the fundamental concepts and principles of surface water analysis, and the application of a model that combines hydrodynamics and water quality. The fundamentals of surface water hydrodynamics and quality including water properties, hydrodynamic processes, governing equations, the fate of contaminants, and their transport are reviewed. Two case studies, the hydrodynamic and quality modeling of a lake and a river, are presented in this section to show how the respective models are applied for different kinds of water bodies. The aim is to help improve the understanding of the different hydrodynamic processes involved in nature, in order to facilitate decision making in real surface water systems management.

Another important aspect of environmental hydraulics is the solid transport. Suspended sediment transport in large rivers is constituted mainly by cohesive sediments, which form aggregates or flocs. The removal of cohesive sediments in aquaculture tanks that are close to these water bodies is a difficult problem. Due to its size, density, and shape, the hydrodynamic behavior of flocs is very different from that of noncohesive sediments as they depend on the interaction with the water column. Chapter 5 shows a model to estimate the floc settling velocity using the fractal theory and by including an adequate definition of the drag coefficient for permeable flocs. The goodness of the results is validated using experiments with flocs from aquaculture recirculation tanks that cultivate trout. The most suitable methods for analyzing the size and the settling velocity of flocs are shown to be the optical methods, because they do not destroy flocs and allow for microscopic analysis.

The management of water quality concerns the control of pollution caused by human activity, so that the water is not degraded to the point that it is no longer suitable for planned uses. If this happens when the use is drinking, it becomes essential to establish an alarm situation that blocks the supply of water. Chapter 6 describes an interesting methodology for abnormality detection in water network. More specifically, a noise pattern analysis is used (i) to demonstrate how water quality events can be classified and then (ii) to reduce the level of false alarms in the monitoring system. The analysis carried out in this section, assisted by practical examples, can also assist control systems in regard to the automatic classification process of observed events, in order to reduce the level of false alarms in water monitoring systems.

Finally, I would like to express my personal appreciation to all the authors who have contributed to giving life to this book. I am sure that all the contributions can give interesting insights to the scientific world inherent in the field of Hydraulics and Environmental Engineering.

Author details

Daniela Malcangio

Address all correspondence to: daniela.malcangio@poliba.it

Department of Civil, Environmental, Land, Building Engineering and Chemistry (DICATECh), Polytechnic University of Bari, Italy

The Effects of Climate Change on Rural-Urban Migration in Sub-Saharan Africa (SSA)—The Cases of Democratic Republic of Congo, Kenya and Niger

Omar Moalin Hassan and Gurudeo Anand Tularam

Additional information is available at the end of the chapter

<http://dx.doi.org/10.5772/intechopen.72226>

Abstract

Water is essential for the existence of living organisms including humans. Water is needed in farms to grow crops, firms and manufacturing industry to produce products and services. This chapter examines water resources availability and management in Sub-Saharan Africa (SSA) in climate change perspective using vector auto-regression (VAR) time series analysis. Water is known to be unevenly distributed among countries and continents around the world, particularly in Sub-Sahara Africa; the water availability varies between member countries and regions in the individual country, water supply systems experience enormous pressure to make water accessible to people in both rural and urban communities. Water security remains to be an integral part of the SSA's effort to achieve food security and supply, halve poverty and eradicate hunger. This chapter more importantly aims to investigate impact of rainfall and temperature issues—that are climate change proxy variables—on water security and people movement in three Sub-Saharan African countries that are Democratic Republic of Congo, Kenya and Niger. This article assesses some possible causes of migration from rural to urban area using VAR and granger causality tests; this process involves four variables namely Rural Migration 'MR', Urban Migration 'MU', Rainfall 'Rain' and Temperature 'Temp'. The model predicts rainfall and temperature across 10 years and examines how these changes impact water availability and people movement in relevant countries. This study finds that some countries are experiencing water security challenges upon which large numbers migrate to urban areas. The study reveals that variations in rainfall and temperature have compounded people movements from rural areas. It is noted that the agricultural production in SSA have not improved over time and in fact, it has further decreased due to the move away from rural areas by many farmers.

Keywords: Sub-Saharan African, climate change, rainfall, temperature, VAR analysis, rural-urban migration

1. Introduction

Not only countries from Sub-Saharan Africa (SSA) are experiencing water security challenges, other developing countries in the world are also facing water security problems. Water security challenges may affect the environmental, economic and social stability and wellbeing in these countries particularly those in SSA regions. The seriousness of these circumstances highlights the need to examine the impact of climate change factors—rain and temp— that may have water security and people movement in SSA. Water security in SSA has been an essential part of the SSA's attempt to achieve sustainable food security and the aim is to eradicate hunger and halve poverty. The chapter selects three Sub-Saharan African countries on the grounds of geographical location, population size and growth rates, people migration, climatic change conditions, current and projected water resources in terms of renewable fresh water resources ($\text{m}^3/\text{capita}/\text{yr}$), as well as economic stability and development.

Water is essential for the existence of life on the planet, it is the primary component of the ecosystem and is used for many purposes [1–3]. The three main purposes are agriculture, industry and domestic, water is also utilized in energy production, transport and recreation. Economic activities, agricultural development and environmental systems could only exist when there is water available to them [4–8]. Nelson Mandela said *“Among the many things that I learnt as president was the centrality of water in the social, political and economic affairs of the country, the continent and the world”* [9, 6, 10]. Lack of the necessary water infrastructure appears to be a major challenge faced in the developing countries, particularly those in SSA [11]. In SSA, water availability and accessibility processes are complicated and time consuming; for instance, in some SSA regions where hours are spent each day by household members to collect water for domestic consumption. It is estimated that a round trip takes an average of 36 min to collect drinking water [5]. The amount of fresh water per capita in the SSA has declined; it dropped about 30% since 1990 [11]. According to [12], 30% of world population lives in dry lands that have only 8% of the total renewable freshwater resources. Climate change is expected to exacerbate water security situation in these areas that are already under water stress. **Figure 1** presents world's environmental hotspots and migration.

To describe water scarcity, there have been several definitions that were in use in recent decades, while majority of these definitions did not receive an unreserved recommendation; however, there has been common view of the primary requirements of water scarcity definition. One of the main requirements of water scarcity definition is that it must suggest possible ways to conduct both quantitative and qualitative assessments. The World Water Development Report listed some of these definitions and defines water scarcity as *“The point at which the aggregate impact of all users impinges on the supply or quality of water under prevailing institutional arrangements to the extent that the demand by all sectors, including the environment, cannot be satisfied fully, a relative concept that can occur at any level of supply or demand. Scarcity may be a social construct (a product of affluence, expectations and customary behaviour) or the consequence of altered supply patterns stemming from climate change. Scarcity has various causes, most of which are capable of being remedied or alleviated”* [13–15].

Water scarcity is the situation where the available fresh water per capita is less than 1000 m^3 per annum—in other words, the minimum agreed amount of fresh water for human survival

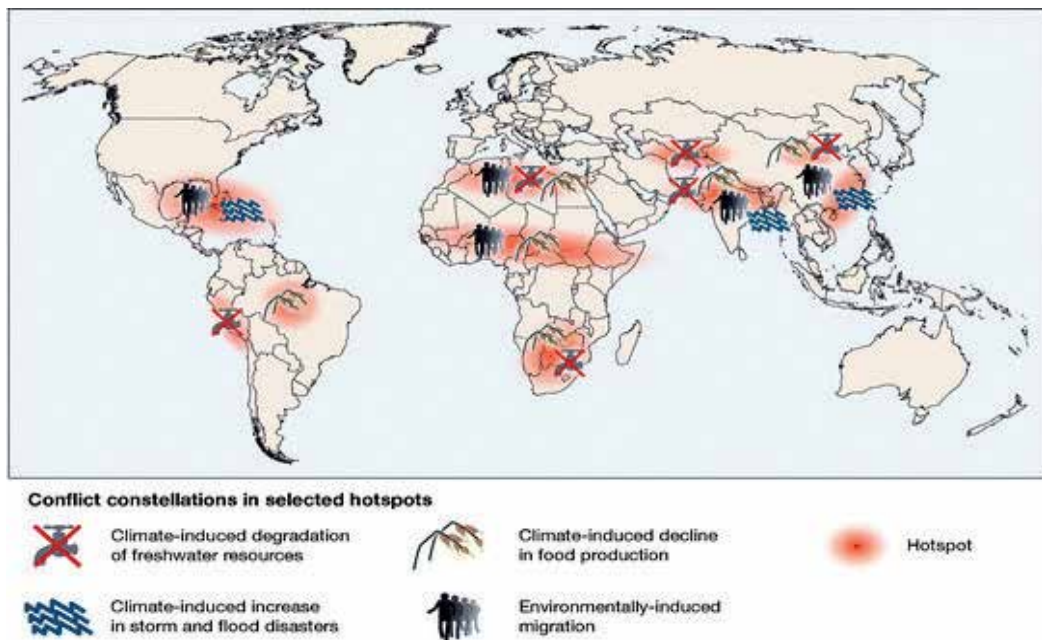


Figure 1. Environmental hotspots and migration [13].

is around 35,318.3 ft³/yr or 1000 m³/yr [7, 14, 15]. Further, a water stress situation exists when the available fresh water per capita per annum is higher than 1000 m³/capita/yr and less than 1700 m³/capita/yr [14–17]. On the other hand, water shortage is defined as the ratio of the total fresh water withdrawal to the available rainfall [18]. The condition of water scarcity (WSC) can also exist when the demand of fresh water (WD) exceeds the fresh water supply (WS) available in a certain period and/or place, that is, when water requirements of some sectors are not met. Water scarcity can also be expressed as a formula: $WSC = WD \geq WS$; [13]. **Figure 2** presents water availability for some African countries in 1999 and 2025. In fact, the World Bank reported that Niger has been under water scarcity condition since 1962 and had 183 m³ of renewable internal freshwater resources per capita in 2014, therefore water availability condition shown for Niger in **Figure 2** seems to be incorrect.

Despite that Sub-Saharan African region appears to have enough water resources all around the year [20], these waters are unevenly distributed between member states. There has been sufficient rainfall in Central Africa region due to the humid and semi-humid weather conditions, these favourable rainfall conditions resulted in water resource abundance in this region. In contrast, there have been considerable rainfall fluctuations in dry and semi-dry regions that experience temperate and semi-temperate climates. The precipitation in these regions characterizes high intensity but occurs within short periods of time; often producing floods and rainwater runoff washing fertile topsoil to downstream [21]. Moreover, Zambia, Angola and Mozambique experienced intense rainfalls in 2000 that caused subsequent floods. However, such heavy rainfalls seem not to have improved the water availability. In fact they have all experienced droughts over the past three decades [22]. The SSA rainfall fluctuation, frequency and amount are met by similar increases in levels of dryness in the region [23]. A period of

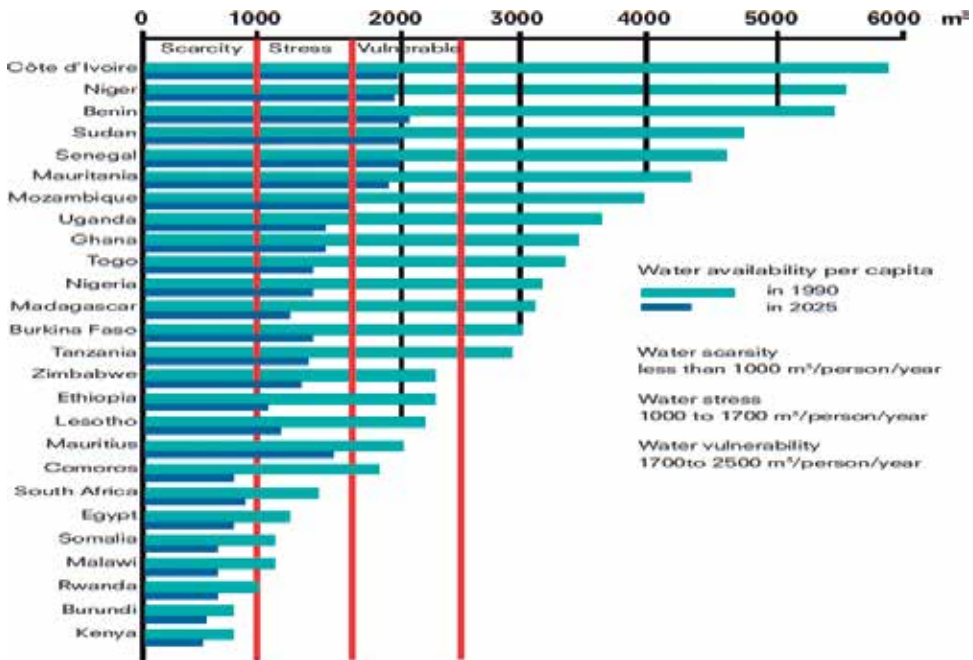


Figure 2. Water availability for some African countries in 1999 and 2025 [19].

low rainfall means a period of scarcity of both feed and water, and an increase in distances to suitable grazing areas [24]; this study also notes that among small-scale farmers, rainfall is the most important climatic factor that is critical to their survival, particularly for crop growth and livestock herds. Geographically, SSA falls below the Sahara Desert and consists of the vast majority of African countries. The countries that fall in the Northern Africa region that are Egypt, Libya, Tunisia, Algeria and Morocco are not in SSA [25]. SSA has an estimated land area of 24.24 million km² [26].

In this chapter, authors critically review the water security and migration situation in SSA region by using a country by country analysis of three selected countries from SSA region. The main aim of this study is to examine water resources availability and accessibility and how rainfall and temperature variations and distributions have impacted water security and people urban migration in the region. The study attempts to identify pull and push factors that appear to affect the people movement from rural to urban areas in SSA. The selected SSA countries are Democratic Republic of Congo (DRC), Kenya and Niger. This study uses VAR and Granger causality methods to analyse rainfall and temperature and their impact on rural/urban migration.

2. Background

Africa is considered to be the second driest continent in the world after Australia [27, 28]. It is predicted that 25 countries in Africa may experience water stress condition by the year 2025 [29, 30]. Nevertheless, world's longest rivers flow within Africa, the Nile River followed

by other main rivers in SSA regions such as the Congo, Zambezi and Niger Rivers. In addition to that, SSA has Lake Victoria, which is the second largest lake in the world [29, 31, 32]. Approximately 53% of Africa is believed to be water abundant and about 61% of the total population live in this region which also holds about 95% of the total renewable water resources of the continent [31]. Nonetheless, it is predicted that by 2025 Africa’s water abundance area may shrink to 35 and 24% of the population that will inhabit in water abundance areas that holds 78% of available renewable water resources. In contrast, the combined water scarcity and deficit areas is expected to increase from 47% of (2000) to 65% in 2025, holding only 22% of the total renewable water resources; so 76% of Africa’s population will live in water scarcity and deficit areas in 2025 as shown in **Table 1**.

Sub-Saharan Africa has 24.24 million km² [26, 32] that is equal to 18% of the world’s land [33] and the average annual rainfall of SSA is estimated to around 815 mm/yr. However, there have been considerable variations of rainfall amounts in SSA’s sub regions; that may be due to climatic differences [34]. Compounding rainfall fluctuation will be the anticipated effects of climate change that will cause more challenges that are yet to be seen. For instance, this may include sudden and large increase in rainfall fluctuations and distribution in the SSA region, creating natural disasters such as floods and droughts have been noted [2, 6, 35, 36]. For instance, annual rainfalls in Sierra Leone, Liberia, Seychelles and Mauritius may reach 2000 mm/yr [34]. In contrast, parts of South Africa and eastern Namibia the annual rainfall is less than 100 mm/yr. Further rainfall in northern Niger may be as low as 10 mm/yr [34]. Hell et al. [37] reported that rainfall in the African is unevenly distributed and added that fewer people live regions that often receive higher rainfall compared to overpopulated regions that receive lower rainfall. According to Temesgen [38], in 2009 around 260 million people in SSA (41% of SSA’s population) lived in dry areas that are vulnerable to drought.

Faurès and Santini [34] reported that production factors such as land and water resources may be abundant in SSA but the region continues to experience a falling GDP of 0.6% since 2004 [38]. Agriculture remains to be the main source of food to SSA’s low socioeconomic communities; rainfed agriculture is anticipated to be the dominating food production system in SSA in foreseeable future. Number of people living under poverty level and undernourished worldwide has been falling in recent decades in general and in Asia in particular. In SSA, the number of people living under the poverty line has not decreased considerably compared to other world regions. Further, SSA has made limited progress in improving the lives of poor

Countries with water	2000			2025		
	Area %	Population %	Water %	Area %	Population %	Water %
Abundance	52.5	60.8	95.2	34.7	23.9	78.3
Scarcity	26.0	24.3	4.4	39.1	57.3	20.6
Deficit	21.5	14.9	0.4	26.2	18.8	1.1
Total African population	786 million			1428 million		

Ashton [31].

Table 1. Water availability projections according to three different conditions in Africa 2000–2025.

people and reducing the number of people living under the poverty line. In fact, number of people living below the poverty line in SSA has risen considerably due to the implementation of the new definition for poverty, where the \$1.00/day has increased to \$1.25/day [39]. In 2014, SSA had 214 million undernourished people (26.6% of the population) [40]. In 1990, East Asia/the Pacific and SSA's contribution to the total number of people living under poverty line in the world were 52 and 15% respectively; after 23 years and in 2013, the percentage of the East Asia/the Pacific has dropped to 9%, while SSA's contribution has increased to 51% in the same period. **Table 2** shows percentage of people living on less than \$1.25/day by world region between 1981 and 2005.

According to Faurès and Santini [34], SSA boasts more than 3880 km³/yr of internal renewable water resources. Central Africa Republic, Guinea, Madagascar and Democratic Republic of Congo are among water rich countries in SSA; in 2014 these countries had 28,776, 17,924, 13,906 and 11,648 m³/yr of internal renewable water resources, respectively. The per capita internal renewable water resources of these countries have fallen from 90,559, 61,230, 56,106 and 62,955 m³/yr in 1962, respectively. Central Africa Region receives about 40% of the annual rainfall in SSA around 7500 km³/yr and only 23% of the SSA population inhabit this region. Indraratna et al. [41] suggested that the uneven distribution of rainfall in SSA necessitates the implementation of suitable policies and water supply systems to enhance the sustainability of water usage in the region. Efficient water supply systems may enable local communities to get social stability, economic development and more importantly to achieve sustainable agricultural production [42]. According to Temesgen [38], there has been number rainwater harvesting initiatives and water management systems in SSA; practices such as in situ and micro catchment are more popular than rainwater irrigation methods. The per capita share of internal

Region	1990	1993	1996	1999	2002	2005	2008	2010	2011	2012	2013
East Asia and the Pacific	966	877	684	669	535	349	288	218	167	142	71
Eastern Europe and Central Asia	9	25	34	37	29	23	15	14	13	12	10
Latin America and the Caribbean	71	68	71	72	71	61	42	39	36	34	34
Middle East and Northern Africa	14	14	12	10	10	9	7	7	7	6	6
South Asia	505	541	517	532	552	508	465	400	328	293	256
Sub-Saharan Africa (SSA)	276	323	346	371	391	382	389	399	396	393	389
SSA (percent to total)	15	17	21	22	25	29	32	37	42	45	51
World	1840	1849	1664	1692	1588	1332	1205	1077	946	880	766

Roser and Ortiz-Ospina [42].

Table 2. People living on less than \$1.25/day by world region 1990–2013 (million).

renewable water resources in SSA has experienced a substantial decline from 16,500 m³ per inhabitant in 1960 to 5500 m³ per capita in 2005; about 65% fall [34, 42], this falling trend is mainly due to the significant increase of SSA's population during this period. In some cases, countries like Niger, Ivory Coast and Uganda, the decline has been more dramatic, **Table 3** shows changes in available renewable internal freshwater resources per capita of six selected countries and SSA between 1962 and 2014.

Table 4 presents changes in per capita water availability by region for five decades between 1950 and 2000. Africa's per capita renewable internal freshwater resources shows the most significant decline, shrinking from 20,000 m³ of water per person in 1950 to 5100 m³ in 2000; this means that each person living in Africa lost about three quarters of their share of available water in just 50 years (**Table 4**). **Figure 3** illustrates that the fresh water per capita share around the world has been decreasing since and predicts a continuous fall until 2050; even though water resources per capita have declined significantly in many world regions such as the Caribbean, Latin America and Northern America since 1950s, the United Nations predicts that people living in Africa and Asia will get the least share of water resources (per capita basis) by 2050.

Despite the rainfall fluctuations, SSA experiences higher temperatures that impact on agricultural production in many parts of the region [44, 45]. Africa is a continent which is experiencing warmer seasons as part of the trend of global warming. It is predicted that temperatures will continue to rise and a growing threat to food production systems in SSA is imminent [44, 45]. In March 2013, the temperature in South Africa's Vioolsdrif village recorded its hottest day ever measured on the area at 47.3°C. Similarly, the temperature in Navrongo, Ghana, reached 43°C on March 6, 2013, the hottest ever recorded. According to Fabusoro et al. [46], the patterns of rainfall and temperatures in the studied area appear to be following a similar upward trend, with temperatures rising at about 0.4°C/month/decade in southwest Nigeria. World average temperatures have increased about 0.85°C between 1886 and 2012, and it is anticipated that average global temperature will continue to increase, reaching around 1.5°C by the middle of the twenty-first century [24]. In the face of such evidence, we must acknowledge that the effects of climate change are real. In the Sub-Saharan African region, where the average temperature is rising, it is claimed by many that climate change is already affecting agriculture and production levels [24, 47]. Between 1980 and 2000, the temperature records from the majority of weather stations in the SSA sub regions revealed progressive warming. Because of this rise in temperature, small farmers could grow crops which are tolerant to higher temperatures [24]. As shown in **Figure 4**, the annual average temperatures of three Sub-Saharan African countries considered in this study have shown a fluctuating trend between 1900 and 1960. More importantly, annual average temperatures of these countries have been rising significantly since 1960 until 2015. It is predicted that average temperatures in these countries will continue to increase.

2.1. People movement and water security in SSA

Population in Sub-Saharan Africa has been growing rapidly since mid-twentieth century, it grew from 228 million in 1962 to reach 911 million in 2012 [14, 15]. In contrast, productive lands have been shrinking and the fast population growth led that SSA's renewable fresh

Year	1962	1967	1972	1977	1982	1987	1992	1997	2002	2007	2012	2014
DRC	56,105	48,971	42,613	37,117	32,471	28,544	24,099	20,534	18,059	15,406	13,048	12,208
KEN	2399	2039	1713	1425	1179	980	829	715	623	544	474	450
NER	973	845	736	639	556	484	415	348	290	241	198	183
NIG	975	845	734	637	552	478	409	344	287	239	197	183
SOM	2088	1858	1727	1243	893	855	801	737	627	544	470	444
ZAF	2445	2149	1887	1659	1464	1300	1159	1044	977	916	853	827
SSA	18,301	16,200	14,259	12,409	10,729	9329	8133	6559	5752	5028	4210	3985

Table 3. Renewable internal freshwater resources per capita (cubic meters) in some SSA countries.

Region	1950	1960	1970	1980	2000
Africa	20.0	16.5	12.7	9.4	5.1
Asia (excluding Oceania)	9.6	7.9	6.1	5.1	3.3
Europe (excluding the Soviet Union)	5.9	5.4	4.9	4.6	4.1
North America and Central America	37.2	30.0	25.2	21.3	17.5
South America	105.0	80.2	61.7	48.8	28.3

Rosegrant [43].

Table 4. Water availability per capita by region, 1950–2000 (1000 m³).

water resources (m³/capita/yr) to decline significantly. The interaction of these circumstances have resulted a large scale people movement in SSA, where people living in rural SSA has decreased from 85% in 1962 to 63% in 2012 [14, 15]. It is predicted that 50% of SSA population will live in urban areas by 2020 thus may lead to major problems for the cities in SSA [14, 15]. There is now evidence that suggests that SSA agriculture has been suffering from multiple difficulties including water shortages, shortage of farm workers and poor productive lands over recent times. In addition to this, there is now evidence that more SSA people are leaving from their rural areas to cities in significant numbers; a phenomenon which was predicted by [1]. **Figure 5** shows the current and projected populations of the world by region.

Tularam and Hassan [14, 15] stated that decreasing water security condition in SSA will represent a major factor that causes human migration in the region. At present, SSA cities appear to be incapable to meet expectations of people migrating from their rural villages to urban areas; this led people to consider other regional and international destination. Europe remains to be the number one destination for SSA migrants crossing the Mediterranean Sea, thus refugee crisis in Europe in recent times shows that the longer term impacts of water insecurity in SSA is yet unpredictable and if major underpinning factors of the water insecurity situation in SSA are not addressed properly, there is going to be undesirable consequences in the future. It is predicted

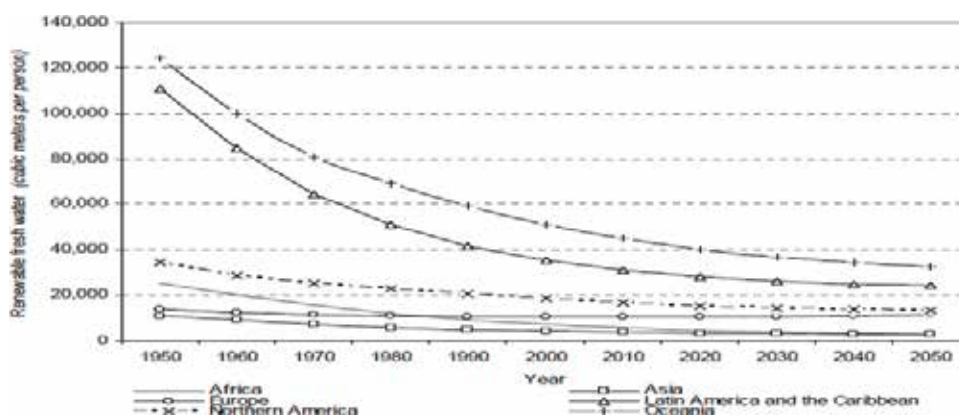


Figure 3. Water availability per capita in major world areas 1950–2050 [44].

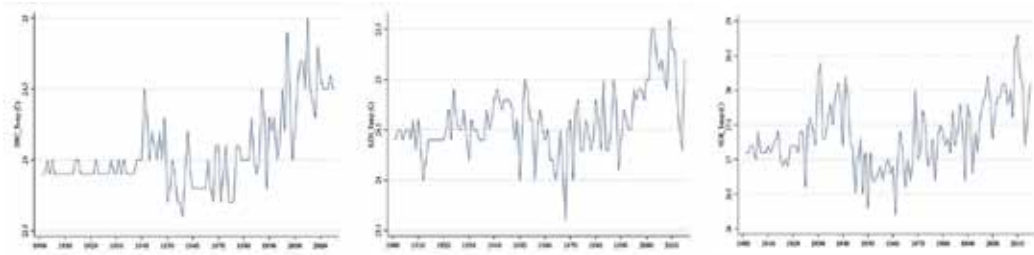


Figure 4. Average annual temperatures of Democratic Republic of Congo, Kenya and Niger 1901–2015.

that Europe may see further waves of SSA migrants coming to the advanced economies, and it is almost unquestionable that SSA migrants arriving Europe will have significant implications to the service delivery systems in place in Europe, particularly in Italy, that represents the major transit hub for SSA migrants. Likewise, other major destinations of SSA migrants include Indonesia, where in recent years migrants from several SSA countries including Sudan and Somalia as well as other migrants from other Asian countries such as Iran, Iraq, Afghanistan, Myanmar, Bangladesh and Sri Lanka are used as a major transit hub on their way to Australia.

2.2. Environmental refugees

Climate change factors such as changing rainfall and temperature have impacted rural communities of SSA and limited people’s ability to establish a meaningful livelihood from their lands [52]. Norman [53] reported that the environmental refugee phenomenon emerged during twentieth century and environmental refugees are defined as *people who are forced to leave their original habitat because of some sort of environmental difficulty* [54]. As noted in [55], the term “environmental refugees” was first used by Essam El-Hinnawi in 1985 where he defined environmental refugees as “those people who have been forced to leave their traditional habitat, temporarily or permanently, because of a marked environmental disruption (natural and/or triggered by people) that jeopardized their existence and/or seriously affected the quality of their life” [56]. Since 1985, researchers and experts in the people migration field have developed similar definitions

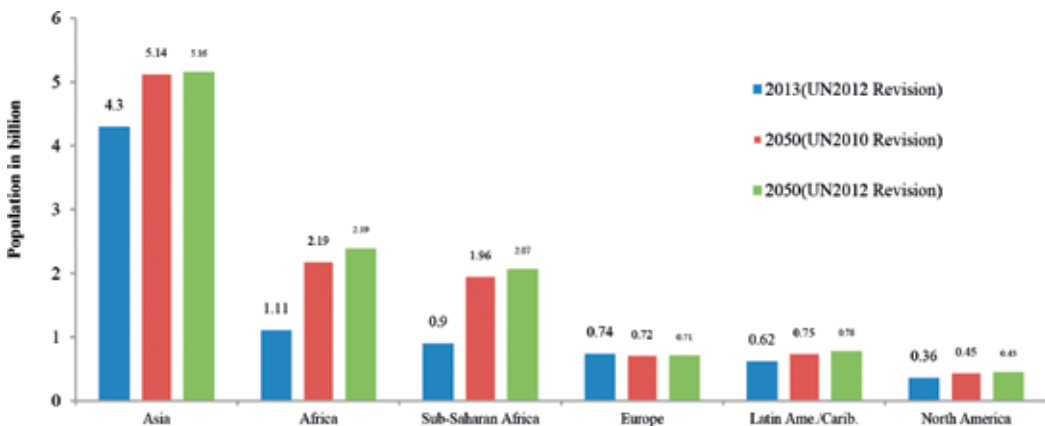


Figure 5. Current and projected populations of the world by region [49–51].

of the environmental refugee [57, 58]. Environmental refugees are those “*persons who no longer gain a secure livelihood in their traditional homelands because of environmental factors of unusual scope, notably drought, desertification, deforestation, soil erosion, water shortages and climate change, also natural disasters as cyclones, storm surges and floods*” [57, 58]. On the other hand, the United Nations High Commissioner for Refugees (UNHCR) has adapted a new term “*environmentally displaced persons*” aiming to minimize the use of the term “*refugee*” and refers environmentally displaced persons as those “*who are displaced from or who feel obliged to leave their usual place of residence, because their lives, livelihoods and welfare have been placed at serious risk as a result of adverse environmental, ecological or climatic processes and events*” [57]. About 50 million environmental refugees were recorded in 2010 and it is projected that the number of environmental refugees will increase to 200 million by the year 2050 [54, 58]. SSA appears to be a major contributor to the number of the environmental refugees in the world, and remains to hold a prime position [53]. It is crucial to adapt economic and social development strategies in SSA to improve the livelihood of SSA rural communities and to reduce poverty levels [59].

This chapter critically reviews water security and human migration issues of selected Sub-Saharan African countries. Changes in water security and human migration patterns are investigated with respect to the climate change variables of rainfall and temperature using time series framework. The authors analyse the water and population-related statistics of several SSA countries with respect to the rates of population growth, availability and accessibility of water resources, and assess possible effects of climate change factors (Rain and Temp); with regard to water resources availability and usage. Rural and urban migrations of these countries are also analysed to identify migration push and pull factors. A special consideration will be given to the migration patterns recently observed and the likelihood of water scarcity or stress in the future. In the following section, information about Democratic Republic of Congo (DRC), Kenya (KEN) and Niger (NER) is presented followed by methodology, then results and discussion and finally conclusion of the chapter.

2.3. Democratic Republic of Congo (DRC)

The Democratic Republic of Congo (DRC) also referred as Zaire, locates in the African Great Lakes region of Central Africa and borders with nine Sub-Saharan African countries namely Angola, Zambia, Tanzania, Burundi, Rwanda, Uganda, South Sudan, Central African Republic and Congo-Brazzaville. DRC is the largest country in SSA and has 2.34 million km² of land and considered to have large deposits of many natural resources such as oil, diamonds, copper and cobalt. Moreover, DRC is also known to as Africa’s water rich country, it holds 23 and 52% of Africa’s internal renewable water resources and surface water reserves, respectively [60]. DRC is the third most populated country in SSA after Nigeria and Ethiopia. Similar to most of SSA countries, the DRC population is growing fast and increased from 16.2 million in 1962 to about 69.57 million in 2012 [61]. A significant composition change in the population was noted where in 2012 around 45% of the DRC population was below the age of 15 years and only about 3% of the population was 65 years and over. In contrast, poverty is widespread in DRC and about 60% of the population lives below the poverty line (\$1.25/day), and it is ranked as one of the world’s poorest countries and positions number 186 out of 186 countries also co-held by Niger another in SSA country [62]. Two-thirds the country falls to the south of the Equator and one-third to the north [63]. The climate in DRC is cool and dry in the southern

highlands with a cold, alpine climate in the Rwenzori Mountains and hot and humid in the river basin [64]. South of the Equator, the rainy season starts in October and lasts until May and in the north of the Equator, rain starts April and continues until November. In addition to this, rainfall is fairly regular throughout the year along the Equator [65]. The annual average rainfall in DRC ranges from 1000 to 1700 mm and average annual temperatures ranges 18–32°C. DRC experiences periodic climatic events such as seasonal flooding in the east and droughts in the south. These events are may be directly related to the significant variations of the rainfall in DRC abundance or lack of precipitation.

AGRA [24] and Chijioke et al. [44, 48] reported that the average temperature is increasing in the Sub-Saharan African region. They also noted that climate change is already affecting agriculture and production levels. Between 1980 and 2000, the temperature records from the majority of weather stations in the SSA sub regions revealed progressive warming. In line to these conditions, food security appears to be a major concern in DRC. There have been constant food insecurities in as much of DRC's rural communities and this may have resulted people movement from rural to urban areas. According to Alinovi et al. [66], the number of undernourished people in DRC has tripled from 12 to 36 million, and the prevalence increased from 31 to 72% of the population. In 2002, about 80% of the Congolese population lived below the poverty line of around US\$0.2 per day [67]. Climate change also causes major events in DRC, for example, between 1974 and 2003, 19 natural disasters were recorder in DRC. Lukamba [68] noted that the Congo River of 4700 km length crosses the country from East to West and its water levels have been increasing steadily and posed risk to communities on its path including the 12 million people living in the capital Kinshasa. DRC is considered to be one of the most vulnerable and affected countries natural disasters. In some occasions, these climatic conditions trigger communities to mobilize and move to other locations seeking better food security conditions. In the following section, people movement in rural and urban areas as well as rainfall and temperature in DRC will be analysed and changes on these factors will be predicted in the next decade.

2.4. Kenya

Kenya is situated in the Eastern Africa region and borders Somalia, Ethiopia, South Sudan, Uganda, Tanzania and the Indian Ocean. Kenya has a 582,646 km² of land including 11,230 km² of water covered land. About 16% of Kenya's land is potentially suitable for agriculture, where 84% of the land is arid and semi-arid that is suitable for livestock or irrigated agriculture [69]. Kenya has dry and humid climates; that is probably the reason Kenya experiences critical water crisis. In Kenya, there has been a high variability of rainfall in terms of time and place and hence this had undesirably affected agricultural production. Presently Kenya is under water scarcity situation and the renewable fresh water per capita is 718.1 m³/yr [61] stating that total internal renewable water resources per capita has dropped from 3558 m³/yr in 1962 to 484.2 m³/yr in 2011. Not surprisingly, it is predicted that the renewable freshwater per capita in Kenya will fall to 235 m³/yr by the year 2025. UNEP (United Nations Environmental Programme) has announced the water crisis in Kenya as critical water scarce [70]. Kenya had a population of around 41 million in 2010 and it has been growing rapidly [71]. Nyanchaga [69] noted that Kenyan population has increased from 5.4 million in 1948 to 42 million in 2011. Rainfall in Kenya is highly variable and the annual average rainfall in the country is 630 mm.

Marshall [71] reported that the annual rainfall in Mt. Kenya reached 1800 mm and that the rainfall in the northern regions of the country is below 200 mm. Rainfed agriculture is the major contributor of the Kenyan economy as to the most of SSA countries [71].

2.5. Niger

Niger is another West African country used in this study. The country borders with Algeria, Benin, Burkina Faso, Chad, Libya, Mali and Nigeria. Country has around 1.3 million km² of land and 15% of arable land [61]. It had a population of about 17.15 million in 2012 [72]. Niger is one the fastest growing countries in SSA in terms of population. The World Bank [72] reported that the population has quintupled within five decades, increasing from 3.33 million in 1960 to 17.15 million in 2012. Beside this population growth, Niger is the poorest country in the world out of 186 countries and positions the 186th place with DRC [62]. Approximately 61% of the population is classified as poor and live with less than \$1/day. In line with other SSA countries, agriculture remains the dominant sector of the economy and accounts for 39% of the GDP in the year 2009. This means that agricultural production levels have significant impact to the annual economic growth. In fact, economic growth in Niger has been highly volatile due to the unfavourable farming conditions. EPRI [73] has noted that the economic growth rates were 3.2, 9.3 and -1.2% in 2007, 2008 and 2009, respectively. Climate change implications have affected Niger and the two main factors that affect the agricultural production are desertification and frequent drought conditions [73]. On the contrary to other SSA countries, during the past 50 years urban population has been growing slowly in Niger, while the rural population increased considerably during the same period. For the past 40 years Niger has experienced a 0.6°C increase of the average temperature with a declining annual average rainfall. Niger has total internal renewable water resources (TRWR) of 3.5 km³; the TRWR per capita has dropped considerably from 973 m³/yr in 1962 to 183 m³/yr in 2014, this appears to have an inverse relationship to the rapidly growing population. Niger withdraws around 2.9% of the actual renewable water resources per year and this has affected the pressure on freshwater withdrawal. In contrast to other SSA countries, Niger has higher percentages of people with access to clean water. In 2015, 100% of people living in urban areas and 48.6% of rural populations had access to clean water sources in Niger. In fact, 58.2% of the total population has access to clean water in Niger.

3. Methodology

3.1. Data sources and procedures

Three Sub-Saharan African countries were selected to test how climate change factors and population growth have impacted people movement (rural-urban migration). The Sub-Saharan African countries involved in this study are Democratic Republic of Congo (DRC), Kenya (KEN) and Niger (NER). The data collected was over 56 year period from 1960 to 2015. The climate change proxy variable (rainfall and temperature) and the data were collected on monthly bases from the National Oceanic and Atmospheric Administration (NOAA) of USA,

and then converted to annual terms (1901–2015). Due to migration, data availability issues, the annual population data (rural, urban and total populations) was collected from the World Bank. The vital statistics method has been used to indirectly measure the net internal migration (rural-urban) of these countries. The yearly natural growth rate of the population in each country accounted for and through this process the migration data were obtained. The time series data in this model consist of four variables that are Rural Migration (MR), Urban Migration (MU), Rainfall (Rain) and Temperature (Temp). The data were initially prepared in excel spreadsheets and then transferred to Stata. Stata is a comprehensive, integrated statistical software package that is used for data management, data analysis and to produce graphics to visualize the data; Stata was developed in 1985 by Stata Corporation. Hashizume et al. [74] has utilized Stata software for rainfall and temperature time series analyses, similarly Ebrahim et al. [75] has suggested the appropriateness of Stata software for the analyses of migrations time series data.

3.2. Multivariate time series analysis: (VAR)

The vector auto-regression (VAR) model is among the most flexible multivariate analysis, well established, and proven models in multivariate time series analysis. Ideally, the model provides a natural extension from the univariate autoregressive models to multivariate models that include deterministic, endogeneous and exogeneous variables. The VAR has a multivariate advantage, for the forecasts developed can be made conditional on the potential future trends in the other given variables. The proposed study will centre on the analysis of covariance stationary multivariate time series using VAR models. Suppose that $Y_t = (Y_{1,t}, Y_{2,t}, \dots, Y_{n,t})'$ represents a time series variable vector ($k \times 1$) then an autoregressive model of the basic vector, having order p , VAR (p) becomes:

$$Y_t = \mu_1 + \alpha_{11}Y_{t-1} + \alpha_{12}Y_{t-1} + \dots + \alpha_{1p}Y_{t-p} + \beta_{11}X_{t-1} + \beta_{12}X_{t-1} + \dots + \beta_{1p}X_{t-p} + u_t \quad (1)$$

$$X_t = \mu_2 + \alpha_{21}Y_{t-1} + \alpha_{22}Y_{t-1} + \dots + \alpha_{2p}Y_{t-p} + \beta_{21}X_{t-1} + \beta_{22}X_{t-1} + \dots + \beta_{2p}X_{t-p} + u_t \quad (2)$$

OR

$$Y_t = c + \Pi_1 Y_{t-1} + \Pi_2 Y_{t-2} + \dots + \Pi_p Y_{t-p} + u_t \quad (3)$$

where $t = 1, \dots, T$ and $(k \times 1)$ and Π_i are coefficient matrices, c a $(k \times 1)$ constant vector and u_t a $(k \times 1)$ vector process for white noise with an unobservable zero mean, with Σ covariance matrix. The Stata software was used to determine the VAR lags most appropriate for each country. The lag selection process was performed using VAR diagnostics and tests method that enables to postestimate the VAR lag order of the time series data. VAR (3) has been the best fit in most cases.

3.3. Granger causality test

A key part of the use of a VAR model is in its use for forecasting. Its structure gives information on the ability of variables or variable groups to forecast other variables. Granger [76] introduced this intuitive notion of a variable's ability to forecast. Should Y_1 variable or variable

groups be instrumental in another Y_2 variable's or variable group's prediction, then Y_1 Granger causes Y_2 . In the opposite case, Y_1 does not Granger cause Y_2 if for all $s > 0$ the mean squared error of a forecast of $Y_{2,t+s}$ based on $(Y_{2,t'}, Y_{2,t-1'}, \dots)$ is the same as the mean squared error of a forecast of $Y_{2,t+s}$ based on $(Y_{2,t'}, Y_{2,t-1'}, \dots)$ and $(Y_{1,t'}, Y_{1,t-1'}, \dots)$. It is worth noting that Granger's causality notion only suggests the ability to influence another variable.

A VAR(p) bivariate model for $Y_t = (Y_{1t}, Y_{2t})'$, can be used to identify the failure of Y_2 to Granger cause Y_1 , given that all p VAR matrices of coefficients are lower triangular. The Wald statistic can test p linear restrictions on coefficients. The coefficient matrices of VAR are diagonal in the event that both Y_2 and Y_1 fail to Granger cause each other. It is important to note that Granger causality is rather useful in finance and continues to be extensively used because it shows bi-directional as well as uni-directional causal nature of the time series data. In essence, how and in what manner the other variables contribute to the prediction process of a given variable; that is, which variables or which information is crucial for the prediction process.

4. Results and discussion

Descriptive statistics briefly summarizes the rural and urban migration, rainfall and temperature time series data (1962–2015) of Democratic Republic of Congo, Kenya and Niger. **Table 5** presents central tendency, data variabilities as well as spread of the data.

The following section presents VAR results of the analysis time series data of MR, MU, Rain and Temp of DRC, KEN and NER to assess how climate change variables Rain and Temp time series may impact rural-urban migration phenomenon of these countries in the future. The first step of the VAR analysis was the lag selection process. The goodness of fit statistics of

Variable	Min	Max	Mean	Range	P50	SD	Variance
DRC_MR	-115,821	79,940	6138.33	195,761	7663.5	37464.27	1.40E^9
DRC_MU	-47,403	59,624	12386.24	107,027	9040	20682.77	4.28E^8
DRC_Rain	1208.6	1728.9	1488.00	426.5	1494.6	67.3	4534.5
DRC_Temp	23.60	25.00	24.06	1.299999	24.00	0.28	0.080
KEN_MR	-115,821	79,940	6138.33	195,761	7663.5	37464.27	1.40E^9
KEN_MU	-47,403	59,624	12386.24	107,027	9040	20682.77	4.28E^8
KEN_Rain	429.9	1005.7	645.60	527.4	640.8	100.7	10136.1
KEN_Temp	23.60	25.60	24.59	2	24.50	0.34	0.114
NER_MR	-4708	18,450	5396.98	23,158	5649	5420.30	2.94E^7
NER_MU	-13,695	7510	1782.02	21,205	1656.5	3708.77	1.38E^7
NER_Rain	106.8	269.1	185.60	162.3	183.2	32.3	1041.5
NER_Temp	26.20	28.80	27.34	2.199999	27.20	0.49	0.240

Table 5. Descriptive statistics summary of MR, MU, rain and temp time series data (1962–2015).

the VAR model gave the R^2 values shown in **Table 6**. The test of the model fit gave favourable results. As shown in **Table 6**, most of R^2 values are above 0.70.

4.1. Democratic Republic of Congo (DRC)

The lag selection process suggested lag 3 for DRC time series. VAR (3) was used to assess the interaction between climatic variables and people movement. In other words how rainfall variability and rising temperatures may have impacted people movement in Democratic Republic of Congo. VAR results have shown that temperature has a significant impact on rural and urban migrations in DRC (**Table 7**). The temperature (lag 2) is a significant variable—less than 10 and 5%—to explain DRC rural migration and urban migration, respectively. Further, the results indicate a strong relationship between rural migration and urban migration in DRC; where urban migration is statistically significant to explain changes in rural migration and vice versa.

Granger causality tests were conducted to test the VAR model and to determine whether each variable plays a significant role in each of the equations. The granger causality tests have shown that there is significant granger causality effect from Temp to both DRC MR and MU. Further, Temp may able to compensate for the other variables including rainfall and lead to a combined granger effect on DRC MR and MU. The combined effect of the rising temperature and rainfall variabilities seem to be significant at 5% level. Further, the results also suggest that there is a significant granger causes exist between rural migration and urban migration where each migration variable granger causes the other at less than 1% significance level. **Table 8** presents the granger causality Wald tests for MR and MU of DRC. The results suggest that future amounts of MR and MU in DRC can be predicted by using Eqs. (4) and (5).

$$\begin{aligned} DRC_MR_t = & 355348 + 1.476MR_{t-1} - 1.237MR_{t-2} + 0.23MR_{t-3} + 1.274MU_{t-1} \\ & - 1.064MU_{t-2} + 0.531MU_{t-3} - 4.35Rain_{t-1} + 22.61Rain_{t-2} \\ & - 7.751Rain_{t-3} + 1987.52Temp_{t-1} - 11957.5Temp_{t-2} - 5619.88Temp_{t-3} + u_t \end{aligned} \quad (4)$$

$$\begin{aligned} DRC_MU_t = & -384210 + 0.586MR_{t-1} - 0.36MR_{t-2} - 0.067MR_{t-3} + 0.52MU_{t-1} \\ & - 0.227MU_{t-2} + 0.142MU_{t-3} + 0.857Rain_{t-1} - 24.366Rain_{t-2} \\ & + 3.364Rain_{t-3} + 5775.5Temp_{t-1} + 11500Temp_{t-2} - 1731.45Temp_{t-3} + u_t \end{aligned} \quad (5)$$

4.2. Kenya (KEN)

The lag selection process suggested lag 3 for KEN time series. VAR (3) was conducted to assess the impact that rainfall fluctuations and rising temperatures have on rural and urban migrations in Kenya. This is to identify how rainfall variability and rising temperatures may impact rural and urban migrations. VAR results have shown that temperature has a significant impact on rural and urban migration in Kenya (**Table 9**). Both rainfall and temperature are statistically significant at less than 5% to explain rural migration in Kenya. Similarly,

Equation	Parms	RMSE	R-sq	chi2	P-value
DRC_MR	13	10478.4	0.9439	857.9503	0.000
DRC_MU	13	7176.59	0.9128	533.7465	0.000
DRC_Rain	13	62.5479	0.3807	31.35537	0.002
DRC_Temp	13	0.203218	0.7205	131.4498	0.000
KEN_MR	13	9601.34	0.9529	1031.6	0.000
KEN_MU	13	7453.29	0.9059	491.136	0.000
KEN_Rain	13	107.421	0.1966	12.48087	0.408
KEN_Temp	13	0.31654	0.5711	67.90203	0.000
NER_MR	13	2916.02	0.7778	178.5192	0.000
NER_MU	13	2882.49	0.5537	63.27865	0.000
NER_Rain	13	29.2051	0.2938	21.21593	0.047
NER_Temp	13	0.33013	0.6683	102.7623	0.000

Table 6. Model fitting for VAR models for MR, MU, rain and temp of Congo DR, Kenya and Niger.

temperature impacts urban migration in Kenya. Further, results also suggest that there is a significant relationship between rural migration and urban migration where each variable is statistically significant to explain changes in to the other.

Granger causality tests were conducted to determine whether each variable plays a significant role in each of the equations. As shown in **Table 10**, both rain and temperature granger cause (<5%) rural migration in Kenya; rainfall and temperature together granger cause rural migration in Kenya at 1% significance level. Further, rising temperatures granger cause MU at less than 5%. The results also suggest that granger causality effects exist between rural and urban migrations, where each migration variable granger causes the other at less than 1% significance level. The VAR results suggest that future amounts of MR and MU in Kenya can be predicted by using Eqs. (6) and (7).

$$\begin{aligned}
 KEN_M R_t = & 143048.2 + 1.527M R_{t-1} - 1.121M R_{t-2} + 0.192M R_{t-3} + 1.105M U_{t-1} \\
 & - 1.096M U_{t-2} + 0.475M U_{t-3} + 15.2Rai n_{t-1} + 0.786Rai n_{t-2} \\
 & - 27.1Rai n_{t-3} + 6401.1Tem p_{t-1} - 14576.6Tem p_{t-2} + 2526.64Tem p_{t-3} + u_t
 \end{aligned} \tag{6}$$

$$\begin{aligned}
 KEN_M U_t = & -207028 + 0.619M R_{t-1} - 0.47M R_{t-2} - 0.023M R_{t-3} + 0.56M U_{t-1} \\
 & - 0.273M U_{t-2} + 0.268M U_{t-3} - 5.785Rai n_{t-1} + 4.024Rai n_{t-2} \\
 & + 12.26Rai n_{t-3} - 2708.18Tem p_{t-1} + 8202.4Tem p_{t-2} + 2833Tem p_{t-3} + u_t
 \end{aligned} \tag{7}$$

4.3. Niger (NER)

VAR lag 3 was used to examine the interaction between climatic variables (namely rainfall and temperature) and migration variables (rural and urban). The VAR results have shown that rainfall

	Lags	Coef.	Std. Err.	z	P-value	[95% conf. interval]	
DRC_MR							
DRC_MR	L1.	1.476003	0.133345	11.07	0.000	1.214651	1.737355
	L2.	-1.23725	0.229631	-5.39	0.000	-1.68732	-0.78718
	L3.	0.230204	0.144511	1.59	0.111	-0.05303	0.513439
DRC_MU	L1.	1.273907	0.19951	6.39	0.000	0.882875	1.66494
	L2.	-1.06411	0.216905	-4.91	0.000	-1.48924	-0.63899
	L3.	0.531081	0.185797	2.86	0.004	0.166926	0.895237
DRC_Rain	L1.	-4.34987	23.08613	-0.19	0.851	-49.5979	40.89811
	L2.	22.61041	23.87814	0.95	0.344	-24.1899	69.4107
	L3.	-7.75103	23.25511	-0.33	0.739	-53.3302	37.82815
DRC_Temp	L1.	1987.52	6380.53	0.31	0.755	-10518.1	14493.13
	L2.	-11957.5	6233.197	-1.92	0.055	-24174.3	259.3549
	L3.	-5619.88	5994.979	-0.94	0.349	-17369.8	6130.059
	Cons	355348.5	185244.5	1.92	0.055	-7723.95	718,421
DRC_MU							
DRC_MR	L1.	0.585985	0.091327	6.42	0.000	0.406987	0.764983
	L2.	-0.36227	0.157273	-2.3	0.021	-0.67052	-0.05402
	L3.	-0.06749	0.098974	-0.68	0.495	-0.26148	0.126494
DRC_MU	L1.	0.519761	0.136643	3.8	0.000	0.251946	0.787576
	L2.	-0.22655	0.148557	-1.53	0.127	-0.51772	0.064613
	L3.	0.141994	0.127251	1.12	0.264	-0.10741	0.391401
DRC_Rain	L1.	0.857312	15.81151	0.05	0.957	-30.1327	31.84731
	L2.	-24.3663	16.35395	-1.49	0.136	-56.4194	7.686882
	L3.	33.36421	15.92725	2.09	0.036	2.147376	64.58104
DRC_Temp	L1.	5775.531	4369.976	1.32	0.186	-2789.47	14340.53
	L2.	11500.03	4269.069	2.69	0.007	3132.805	19867.25
	L3.	-1731.45	4105.915	-0.42	0.673	-9778.89	6315.998
	Cons	-384,210	126872.5	-3.03	0.002	-632,875	-135,544

Table 7. Democratic Republic of Congo MR and MU VAR results.

(lags 1 and 3) impacts rural migration in Niger and statistically significant. Moreover, temperature (lag 2) impacts rural migration at less than 10% significance level. On the other hand, the VAR results have shown that rainfall impacts urban migration and statistically significant (less than 5%); while temperature (lag 2) impacts urban migration at less than 5% significance level (**Table 11**).

Equation	Excluded	chi ²	df	P-value
DRC_MR	DRC_MU	43.642	3	0.000
DRC_MR	DRC_Rain	0.90801	3	0.823
DRC_MR	DRC_Temp	7.7732	3	0.051
DRC_MR	ALL	47.282	9	0.000
DRC_MU	DRC_MR	82.511	3	0.000
DRC_MU	DRC_Rain	5.2714	3	0.153
DRC_MU	DRC_Temp	14.913	3	0.002
DRC_MU	ALL	126.24	9	0.000

Table 8. Granger causality Wald tests for MR and MU of DRC.

	Lags	Coef.	Std. Err.	z	P-value	[95% Conf. Interval]	
KEN_MR							
KEN_MR	L1.	1.527326	0.124974	12.22	0.000	1.282381 1.772271	
	L2.	-1.12056	0.200759	-5.58	0.000	-1.51404 -0.72708	
	L3.	0.191674	0.130621	1.47	0.142	-0.06434 0.447688	
KEN_MU	L1.	1.105072	0.173335	6.38	0.000	0.765342 1.444802	
	L2.	-1.09597	0.199596	-5.49	0.000	-1.48717 -0.70477	
	L3.	0.475334	0.153952	3.09	0.002	0.173592 0.777075	
KEN_Rain	L1.	15.18659	12.65142	1.2	0.230	-9.60974 39.98292	
	L2.	0.785979	12.16677	0.06	0.948	-23.0605 24.6324	
	L3.	-27.1015	11.93806	-2.27	0.023	-50.4996 -3.70329	
KEN_Temp	L1.	6401.065	3979.371	1.61	0.108	-1398.36 14200.49	
	L2.	-14576.6	4502.144	-3.24	0.001	-23400.6 -5752.53	
	L3.	2526.642	4568.531	0.55	0.580	-6427.51 11480.8	
	Cons	143048.2	114,720	1.25	0.212	-81798.8 367895.3	
KEN_MU							
KEN_MR	L1.	0.618856	0.097015	6.38	0.000	0.428711 0.809001	
	L2.	-0.4728	0.155844	-3.03	0.002	-0.77825 -0.16736	
	L3.	-0.02283	0.101398	-0.23	0.822	-0.22156 0.175912	
KEN_MU	L1.	0.563427	0.134556	4.19	0.000	0.299703 0.827151	
	L2.	-0.27283	0.154942	-1.76	0.078	-0.57651 0.030848	
	L3.	0.267967	0.11951	2.24	0.025	0.033733 0.502201	
KEN_Rain	L1.	-5.7853	9.820989	-0.59	0.556	-25.0341 13.46348	
	L2.	4.023753	9.444765	0.43	0.670	-14.4877 22.53515	
	L3.	12.26245	9.267225	1.32	0.186	-5.90098 30.42588	

	Lags	Coef.	Std. Err.	z	P-value	[95% Conf. Interval]	
KEN_Temp	L1.	-2708.18	3089.089	-0.88	0.381	-8762.68	3346.322
	L2.	8202.401	3494.905	2.35	0.019	1352.513	15052.29
	L3.	2832.964	3546.439	0.8	0.424	-4117.93	9783.857
	Cons	-207,028	89054.35	-2.32	0.020	-381,572	-32485.1

Table 9. Kenya MR and MU VAR results.

Further, there is a significant relationship between urban migration and rural migration in Niger, where rural migration is statistically significant at less than 5% to explain changes that occur to urban migration in Niger.

Granger causality tests were conducted to examine whether each variable plays a significant role in each of the equations. The granger causality tests have indicated that there are granger causality effects from Rain to both MR and MU at less than 5% significance level (**Table 12**). Further, the results also suggest that there is a granger causality running from urban migration to rural migration at less than 1% significance level. The granger causality Wald tests have suggested that temperature does not granger cause people movement in Niger. The results suggest that future amounts of MR and MU in NER can be predicted by using Eqs. (8) and (9).

$$\begin{aligned}
 NER_M R_t = & 46384.24 + 1.64M R_{t-1} - 1.26M R_{t-2} + 0.467M R_{t-3} + 1.228M U_{t-1} \\
 & - 1.144M U_{t-2} + 0.378M U_{t-3} + 26.3Rai n_{t-1} + 9.86Rai n_{t-2} \\
 & - 40.56Rai n_{t-3} + 622Tem p_{t-1} - 1918Tem p_{t-2} - 356Tem p_{t-3} + u_t
 \end{aligned} \quad (8)$$

$$\begin{aligned}
 NER_M U_t = & -56334 + 0.616M R_{t-1} - 0.644M R_{t-2} + 0.15M R_{t-3} + 1.014M U_{t-1} \\
 & - 0.7M U_{t-2} + 0.21M U_{t-3} - 32.82Rai n_{t-1} - 8.85Rai n_{t-2} \\
 & + 42.987Rai n_{t-3} - 498.24Tem p_{t-1} + 2293.47Tem p_{t-2} + 247.89Tem p_{t-3} + u_t
 \end{aligned} \quad (9)$$

Equation	Excluded	chi ²	df	P-value
KEN_MR	KEN_MU	47.081	3	0.000
KEN_MR	KEN_Rain	7.961	3	0.047
KEN_MR	KEN_Temp	11.625	3	0.009
KEN_MR	ALL	66.058	9	0.000
KEN_MU	KEN_MR	76.582	3	0.000
KEN_MU	KEN_Rain	2.7587	3	0.430
KEN_MU	KEN_Temp	10.582	3	0.014
KEN_MU	ALL	113.33	9	0.000

Table 10. Granger causality Wald tests for MR and MU of Kenya.

	Lags	Coef.	Std. Err.	z	P-value	[95% Conf. Interval]	
NER_MR							
NER_MR	L1.	1.648669	0.548767	3	0.003	0.573106	2.724232
	L2.	-1.26126	1.001884	-1.26	0.208	-3.22492	0.702394
	L3.	0.46737	0.568036	0.82	0.411	-0.64596	1.5807
NER_MU	L1.	1.22845	0.547162	2.25	0.025	0.156032	2.300868
	L2.	-1.1438	0.997921	-1.15	0.252	-3.09969	0.812092
	L3.	0.378649	0.570321	0.66	0.507	-0.73916	1.496458
NER_Rain	L1.	26.30783	14.01253	1.88	0.060	-1.15623	53.77188
	L2.	9.863682	13.98378	0.71	0.481	-17.544	37.27138
	L3.	-40.5639	15.41653	-2.63	0.009	-70.7798	-10.3481
NER_Temp	L1.	622.3344	1061.896	0.59	0.558	-1458.94	2703.613
	L2.	-1918.36	1100.37	-1.74	0.081	-4075.05	238.3239
	L3.	-356.347	1057.053	-0.34	0.736	-2428.13	1715.438
	Cons	46384.24	39517.46	1.17	0.240	-31068.6	123,837
NER_MU							
NER_MR	L1.	0.615852	0.542456	1.14	0.256	-0.44734	1.679046
	L2.	-0.64425	0.990362	-0.65	0.515	-2.58532	1.296827
	L3.	0.149531	0.561503	0.27	0.790	-0.951	1.250057
NER_MU	L1.	1.013816	0.54087	1.87	0.061	-0.04627	2.073901
	L2.	-0.7102	0.986445	-0.72	0.472	-2.6436	1.223198
	L3.	0.207188	0.563762	0.37	0.713	-0.89777	1.312142
NER_Rain	L1.	-32.8194	13.85138	-2.37	0.018	-59.9676	-5.67121
	L2.	-8.85125	13.82296	-0.64	0.522	-35.9438	18.24125
	L3.	42.98771	15.23924	2.82	0.005	13.11935	72.85607
NER_Temp	L1.	-498.241	1049.684	-0.47	0.635	-2555.58	1559.103
	L2.	2293.472	1087.715	2.11	0.035	161.5892	4425.355
	L3.	247.8878	1044.897	0.24	0.812	-1800.07	2295.847
	Cons	-56333.9	39,063	-1.44	0.149	-132,896	20228.15

Table 11. Niger MR and MU VAR results.

Equation	Excluded	chi ²	df	P-value
NER_MR	NER_MU	14.534	3	0.002
NER_MR	NER_Rain	8.5631	3	0.036
NER_MR	NER_Temp	3.4747	3	0.324
NER_MR	ALL	33.264	9	0.000
NER_MU	NER_MR	2.9754	3	0.395
NER_MU	NER_Rain	10.792	3	0.013
NER_MU	NER_Temp	4.9537	3	0.175
NER_MU	ALL	23.811	9	0.005

Table 12. Granger causality Wald tests for MR and MU of Niger.

5. Summary

As presented in the sections above, Democratic Republic of Congo, Kenya and Niger have been experiencing considerable rainfall fluctuations; that is often below average levels. In addition to that all countries have also experienced rising temperatures. As shown in Figure 6, it is

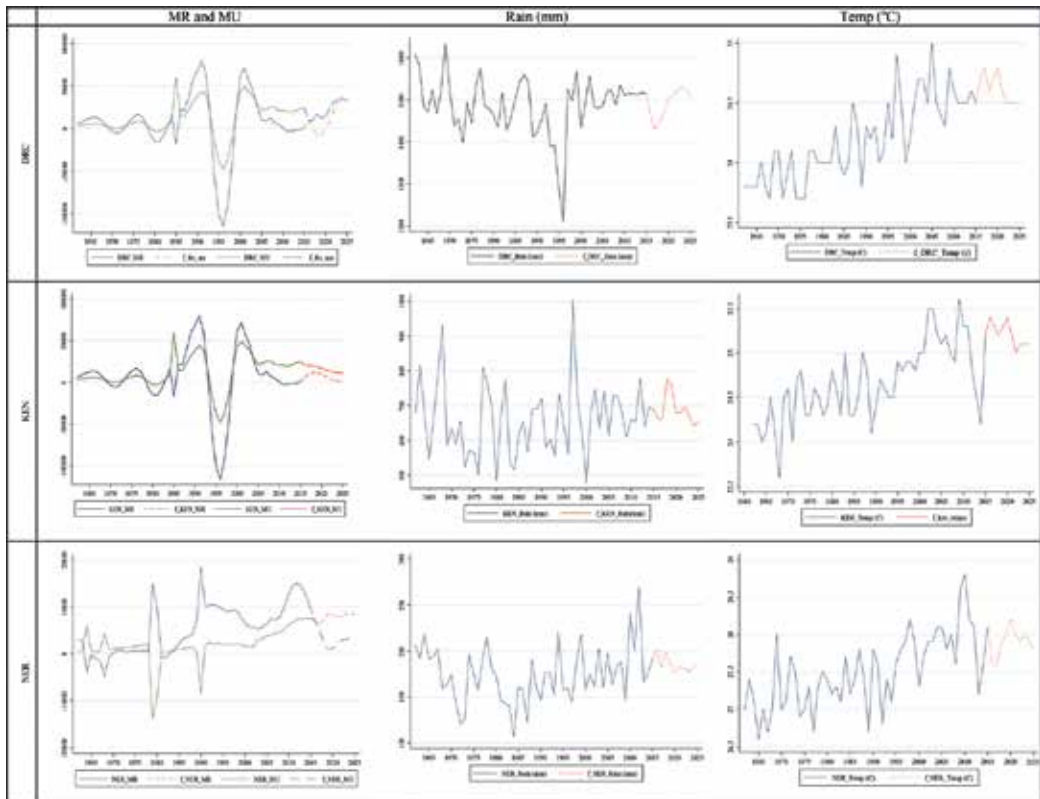


Figure 6. DRC, KEN and NER time series and forecasted line plots 1960–2025.

predicted that these climatic conditions will continue to exist. Populations in these countries have been growing rapidly. These unfavourable climatic conditions and increasing population have together compounded the water scarcity and rural-urban migration conditions in Kenya and Niger. In contrast to that, Democratic Republic of Congo receives high annual rainfalls and medium low average annual temperature. Democratic Republic of Congo has abundant water resources and the renewable internal freshwater resources per capita (m^3) is significantly high. During the vector auto-regression analyses, the lag selection process suggested lag 3 in all cases. VAR was used to investigate the interaction between climatic variables—rainfall and temperature—and people movement variables—rural and urban migrations. By using VAR (3), it was tested how rainfall variabilities and rising temperatures impact rural-urban migrations in Democratic Republic of Congo, Kenya and Niger. The VAR results have suggested that both rainfall and temperature impact rural migration and statistically significant. Further, the results also indicated that there is a significant relationship between rural and urban migrations.

Moreover, granger causality Wald tests were conducted to test the VAR model and to determine whether each variable plays a significant role in each of the equations. The granger causality tests have shown that there is significant granger causality effect from Rain and/or Temp to both rural and urban migrations in Democratic Republic of Congo and Kenya. Moreover, Rain and Temp together have a combined granger effect on MR and MU; this is statistically significant. In contrast, the granger causality test has shown that there is significant granger causality effect from Rain to both rural and urban migrations in Niger. However, rising temperatures does not appear to granger cause people movement in Niger. The results also suggest that there is a significant granger causes exist between rural migration and urban migration where each migration variable granger causes the other at less than 1% significance level. VAR auto forecasting in Stata and Eqs. (4), (5), (6), (7), (8) and (9) (inclusive) were used to predict changes of rural migration, urban migration, rainfall and temperature of Democratic Republic of Congo, Kenya and Niger in the next 10 years. The study predicts increasing rural-urban migrations in the next decade due to high rainfall variabilities and increasing temperatures. This study suggests that there will be a large number of rural communities leaving from their villages to urban areas due to water availability conditions and poor agricultural production levels.

6. Conclusion

This study investigated Sub-Saharan Africa water availability and water security conditions in relation to rural-urban migration numbers. The SSA countries considered in this study are Democratic Republic of Congo (DRC), Kenya (KEN) and Niger (NER). The countries were selected based on specific factors such as water resources availability, population growth, migration processes and urbanization situation in recent times. The study finds that all three countries have fast growing populations with Niger having the highest fertility rate in the world. The countries are experiencing rapid urbanization where rural communities have been moving to urban areas at increased rates. The study finds that the renewable internal freshwater resources per capita (cubic meters) in Niger and Kenya have reached well below the water scarcity level of $1000 \text{ m}^3/\text{capita}/\text{annum}$. In 2014, these countries had renewable internal freshwater resources per capita (cubic meters) of $183 \text{ m}^3/\text{capita}/\text{annum}$ and $450 \text{ m}^3/\text{capita}/\text{annum}$, respectively. On the other hand, Democratic Republic of Congo is known to be the SSA's water rich

state and in 2014 DRC had renewable internal freshwater resources per capita (cubic meters) of 12,208 m³/capita/annum. Despite the water abundance situation only 52.4% of the total population in DRC has access to improved water source. Further it is noted that 81% of urban population and 31% of rural populations had access to clean water sources in DRC in 2015. In general, many rural communities in these countries have limited access to clean water. Water availability and accessibility remains to be major challenge in rural communities of these countries.

This study reveals large rainfall variation and raising temperatures in DRC, KEN and NER. The adverse nature of climate change in these countries appears to have impacted agricultural production and livelihoods in the rural communities. These conditions led great deal of rural-urban migrations that occurred in these countries in recent times. Further, limited access to clean water in rural communities appears to have compounded the rural migration and rapid urbanization in these countries. In addition to that, the agricultural production in SSA has not been improving in recent times and this has exacerbated the move away from rural areas towards the urban. The study conducted VAR analyses and granger causality tests and concluded that rainfall and temperature have granger impact on rural and urban migrations in DRC, KEN and NER. The study predicts increasing rural and urban migrations in Democratic Republic of Congo, Kenya and Niger due to large rainfall fluctuations and rising temperatures.

Author details

Omar Moalin Hassan¹ and Gurudeo Anand Tularam^{2*}

*Address all correspondence to: a.tularam20@gmail.com

1 Environment Futures Research Institute, Griffith University, Brisbane, Australia

2 Mathematics and Statistics, Griffith Sciences (ENV), Environment Futures Research Institute, Griffith University, Brisbane, Australia

References

- [1] Tularam GA, Murali KK. Water security issues of Asia and their implications for Australia. In: Proceedings of the IWGC-Fifth International Groundwater Conference, The Assessment and Management of Groundwater Resources in Hard Rock Systems with Special Reference to Basaltic Terrain; 2012. p. 288
- [2] Tularam GA, Illahee M. Time series analysis of rainfall and temperature interactions in coastal catchments. *Journal of Mathematics and Statistics*. 2010;6(3):372-380
- [3] Tularam GA, Krishna M. Long term consequences of groundwater pumping in Australia: A review of impacts around the globe. *Journal of Applied Sciences in Environmental Sanitation*. 2009;4(2):151-166
- [4] Davidson-Harden A, Naidoo A, Harden A. The geopolitics of the water justice movement. *Peace, Conflict and Development*. 2007;11(11):1-34

- [5] Meeks R. Water works: The economic impact of water infrastructure. Harvard Environmental Economics Program, Harvard Kennedy School; 2012 Discussion Paper 12-35. p. 2. https://heep.hks.harvard.edu/files/heep/files/dp35_meeks.pdf
- [6] Roca E, Tularam GA, Reza R. Fundamental signals of investment profitability in the global water industry. *International Journal of Water*. 2015;9(4):395-424
- [7] Tularam GA, Marchisella P. Water scarcity in Asia and its long-term water and border security implications for Australia. In: *Securing Water and Wastewater Systems*. Cham: Springer International Publishing; 2014. pp. 189-211
- [8] Tularam GA, Murali KK. Water security problems in Asia and longer term implications for Australia. In: *Sustainable Water Use and Management*. Cham: Springer International Publishing; 2015. pp. 119-149
- [9] Msangi JP. Managing water scarcity in Southern Africa: Policy and strategies. In: *Combating Water Scarcity in Southern Africa*. Dordrecht: Springer; 2014. pp. 21-41
- [10] Steele M, Schulz N, Musana F. Water hungry coal: Burning South Africa's water to produce electricity. *Greenpeace Africa*; 2012;4:1-40
- [11] Jenna D, Roz N, Eran B, Amy P. Water, nutrition, health and poverty in Sub-Saharan Africa. *Water Nexus 2012 Connecting the Dots: The Water, Food, Energy and Climate Nexus*. Stanford University; 2012
- [12] Warner K, Hamza M, Oliver-Smith A, Renaud F, Julca A. Climate change, environmental degradation and migration. *Natural Hazards*. 2010;55(3):689-715
- [13] Steduto P, Faurès JM, Hoogeveen J, Winpenny J, Burke J. *Coping with Water Scarcity: An Action Framework for Agriculture and Food Security*. Rome: Food and Agriculture Organization of the United Nations; 2012
- [14] Tularam GA, Hassan OM. Water availability and food security: Implication of people's movement and migration in sub-Saharan Africa (SSA). In: Thangarajan M, Singh VP, editors. *Groundwater Assessment, Modeling, and Management*. New York: CRC Press; 2016. pp. 405-426
- [15] Tularam GA, Hassan OM. The vulnerable nature of water security in Sub-Saharan Africa (SSA)—A country by country analysis. In: Whitney S, editor. *Handbook on Africa: Challenges and Issues of the 21st century*. Hauppauge/New York: Nova Science Publishers; 2016. pp. 47-83
- [16] Florida S. Sustainability of surface and subsurface water resources: Case studies from Florida and Michigan, USA. *Water Resources*. 2004;127:100-107
- [17] Lam V. Review of water scarcity in Northern China: Why is the water scarce, and what can be done about it?; 2012
- [18] DoE US. *Energy Demands on Water Resources: Report to Congress on the Interdependency of Energy and Water*. Washington, DC: US Department of Energy; 2006. p. 1

- [19] UN. Global Environment Outlook 2000 (GEO). London: Economic Commission for Africa (UNECA), United Nations Environmental Programme UNEP, Earthscan; 1999
- [20] UNDP. How food insecurity persists amid abundant resources. In: Africa Human Development Report 2012: Towards a Food Secure Future. New York: Regional Bureau for Africa/United Nations Development Programme; 2012. pp. 27-44
- [21] Mekdaschi R, Liniger H. Water Harvesting: Guidelines to Good Practice. Centre for Development and Environment; Bern, Switzerland: University of Bern; 2013
- [22] Boko M, Niang I, Nyong A, Vogel C, Githeko A, Medany M, Osman-Elasha B, Tabo R, Yanda P. Africa. In: Parry ML, Canziani OF, Palutikof JP, van der Linden PJ, Hanson CE, editors. Climate Change 2007: Impacts, Adaptation and Vulnerability. Contribution of Working Group II to the Fourth Assessment Report of the Intergovernmental Panel on Climate Change. Cambridge/New York, NY, USA: Cambridge University Press; 2007. pp. 433-467
- [23] Climate and Development Knowledge Network. Managing climate extremes and disasters in Africa: Lessons from the SREX report. CDKN; 2012
- [24] AGRA. Africa Agriculture Status Report: Climate Change and Smallholder Agriculture in Sub-Saharan Africa. Nairobi, Kenya: Alliance for a Green Revolution in Africa; 2014
- [25] UNEP. Regionally based assessment of persistent toxic substances. Mediterranean Regional Report. United Nations Environment Programme (UNEP); 2002
- [26] Livingston G, Schonberger S, Delaney S. Sub-Saharan Africa: The state of smallholders in agriculture. In: Paper Presented at the International Fund for Agricultural Development IFAD Conference on New Directions for Smallholder Agriculture, Rome, Italy; 2011. p. 9
- [27] ADF VII. Climate Change And Ecosystem Sustainability: Acting on Climate Change For Sustainable Development in Africa, Seventh African Development Forum, United Nations Conference Centre, Addis Ababa. ADF VII, Issues Paper #9, Ethiopia; 2010. pp. 10-15
- [28] Cherry GA. Review of Australia's Relationship with the Countries of Africa. Joint Standing Committee on Foreign Affairs, Defence and Trade; 2009. Submission No.41. p. 2
- [29] Mejia A, Nucete Hubner M, Ron Sánchez E, Doria M. The United Nations World Water Development Report–No.4–Water and Sustainability. A Review of Targets, Tools and Regional Cases. UNESCO; 2012
- [30] UN. Trends in Sustainable Development: Africa Report. United Nations: Division for Sustainable Development, Department of Economic and Social Affairs; 2008. p. 38
- [31] Ashton PJ. Avoiding conflicts over Africa's water resources. *AMBIO: A Journal of the Human Environment*. 2002;31(3):236-242
- [32] Ashton P, Turton A. Water and security in Sub-Saharan Africa: Emerging concepts and their implications for effective water resource management in the Southern African region. In: Facing Global Environmental Change. Berlin/Heidelberg: Springer; 2009. pp. 661-674

- [33] Eberhard A, Foster V, Briceño-Garmendia C, Ouedraogo F, Camos D, Shkaratan M. Underpowered: The State of the Power Sector in Sub-Saharan Africa. Background Paper; Washington, USA: The World Bank; 2008
- [34] Faurès JM, Santini G. Water and the Rural Poor: Interventions for Improving Livelihoods in Sub-Saharan Africa. Rome: FAO; 2008
- [35] Tularam GA, Ilahee M. Environmental concerns of desalinating seawater using reverse osmosis. *Journal of Environmental Monitoring*. 2007;9(8):805-813
- [36] Tularam GA, Reza R. Water exchange traded funds: A study on idiosyncratic risk using Markov switching analysis. *Cogent Economics & Finance*. 2016;4(1):1139437. DOI: 10.1080/23322039.2016.1139437
- [37] Hell K, Mutegi C, Fandohan P. Aflatoxin control and prevention strategies in maize for sub-Saharan Africa. *Julius-Kühn-Archiv*. 2010;2(425):534
- [38] Temesgen BB. Rainwater harvesting for dryland agriculture in the Rift Valley of Ethiopia. PhD Thesis. Wageningen, NL: 2012. ISBN: 978-94-6173-215-6
- [39] DFID. Agriculture, Growth and Poverty Reduction. London, United Kingdom: Department for International Development; 2004
- [40] Maletta H. Hunger Amidst Plenty: World Trends in Undernourishment and Malnutrition; 2014
- [41] Indraratna B, Tularam GA, Blunden B. Reducing the impact of acid sulphate soils at a site in Shoalhaven floodplain of new South Wales, Australia. *Quarterly Journal of Engineering Geology and Hydrogeology*. 2001;34(4):333-346
- [42] Winterbottom R, Reij C, Garrity D, Glover J, Hellums D, McGahuey M, Scherr S. Improving Land and Water Management. World Resources Institute Working Paper; 2013
- [43] Rosegrant MW. Water Resources in the Twenty-First Century: Challenges and Implications for Action No. 20. Washington, DC: International Food Policy Research Institute, IFPRI; 1997
- [44] UN. World Population Prospects: The 2006 Revision Volume III: Analytical Report. New York: United Nations Department of Economic and Social Affairs/Population Division; 2006. p. 17
- [45] Bello OB, Ganiyu OT, Wahab MKA, Afolabi MS, Oluleye F, Mahmud J, Azeez MA, Abdulmalik SY. Evidence of climate change impacts on agriculture and food security in Nigeria. *International Journal of Agriculture and Forestry*. 2012;2(2):49-55
- [46] Enete AA, Amusa TA. Challenges of agricultural adaptation to climate change in Nigeria: A synthesis from the literature. *Field Actions Science Reports*. The Journal of Field Actions. 2010;4:1-11
- [47] Fabusoro E, Sodiya CI, Fasona M, Oyedepo J. Vulnerability of Settled Fulani Agro-Pastoralists' Livelihoods to Climate Change and Emerging Innovations for Adaptation and Land Accessibility in Southwest Nigeria, 2013-02. Washington, DC: International START Secretariat; 2014

- [48] Chijioke OB, Haile M, Waschkeit C. Implication of climate change on crop yield and food accessibility in Sub-Saharan Africa. Interdisciplinary Term Paper. Center for Development Research ZEF. Bonn, Germany: University of Bonn; 2011
- [49] DESA. Seven Billion and Growing: The Role of Population Policy in Achieving Sustainability. United Nations Department of Economic and Social Affairs, Population Division. Technical Paper, No. 2011/3; 2013
- [50] DESA. World Population Prospects: The 2012 Revision, Volume II, Demographic Profiles (ST/ESA/SER.A/345), Department of Economic and Social Affairs, Population Division, United Nations; 2013
- [51] DESA. World Population Prospects: The 2012 Revision. United Nations Department of Economic and Social Affairs; 2014
- [52] The World Bank. South Asia: Shared views on development and climate change, Chapter 10. In: The Social Dimensions of Climate Change. South Asia Region Sustainable Development Department. Washington, USA: The World Bank; 2009. pp. 131-137
- [53] Norman M. Environmental refugees: A growing phenomenon of the 21st century. The Royal Society; 2001
- [54] Peters KL. Environmental refugees [thesis]. Social Sciences Department, College of Liberal Arts, California Polytechnic State University; 2011
- [55] UNEP. The State of the Environment in Somalia: A Desk Study. Nairobi: United Nations Environment Programme; 2005
- [56] Khan MR. Toward a Binding Climate Change Adaptation Regime, A Proposed Framework, Routledge Advanced in Climate Change Research. London/New York: Routledge; 2014
- [57] Ďurková P, Gromilova A, Kiss B, Plaku M. Climate Refugees in the 21st Century. Vienna: Regional Academy on the United Nations; 2012
- [58] Myers N. Environmental refugees: A growing phenomenon of the 21st century. Philosophical Transactions of the Royal Society of London B: Biological Sciences. 2002;357(1420):609-613
- [59] Diao X, Hazell PB, Resnick D, Thurlow J. The Role of Agriculture in Development: Implications for Sub-Saharan Africa. Washington, DC: International Food Policy Research Institute, IFPRI; 2007
- [60] UNEP. Water Issues in the Democratic Republic of the Congo: Challenges and Opportunities. Nairobi, Kenya: United Nations Environment Programme; 2011
- [61] FAO. FAOSTAT Database. Rome, Italy: Food and Agriculture Organization of the United Nations; 2013
- [62] UNDP. Human Development Report 2013: The Rise of the South: Human Progress in a Diverse World. New York, USA: United Nations Development Programme; 2013. pp. 139-197

- [63] Kisangani EF. Historical Dictionary of the Democratic Republic of the Congo. London: Rowman & Littlefield; 18 November 2016
- [64] Kazongo J. DRC Richest and Poorest Country. Bloomington, USA: Xlibris Corporation LLC; 2016. pp. 1-78. ISBN-978152450059-7
- [65] Mula MG, Saxena KB. Lifting the Level of Awareness on *Pigeon pea*—A Global Perspective. Andhra Pradesh, Patancheru: International Crops Research Institute for the Semi-Arid Tropics; 2010. pp. 540. ISBN: 978-92-9066-535-9
- [66] Alinovi L, Hemrich G, Russo L. Addressing food insecurity in fragile states: Case studies from the Democratic Republic of the Congo, Somalia and Sudan. ESA Working Paper; 2007 July
- [67] Vlassenroot K, Ntububa S, Raeymaekers T. Food Security Responses to the Protracted Crisis Context of the Democratic Republic of the Congo. University of Ghent; 2007
- [68] Lukamba MT. Natural disasters in African countries: What can we learn about them? TD: The Journal for Transdisciplinary Research in Southern Africa. 2010;6(2):478-495
- [69] Nyanchaga EN. Importance of Water in Kenya: Challenges and Reforms. Kenya: Tampere University of Technology and Department of Civil and Construction Engineering University of Nairobi; 19 August 2011
- [70] Ogendi GM, Ong'oa IM. Water policy, accessibility and water ethics in Kenya. Santa Clara Journal of International Law. 2009;7:177
- [71] Marshall S. The water crisis in Kenya: Causes, effects and solutions. Global Majority E-Journal. 2011;2(1):31-45
- [72] World Bank. World Development Indicators 1960-2013. The World Bank; 09 April 2014
- [73] EPRI. Country profiles: Chapter 36. In: Country Profile: Niger. Cape Town: Economic Policy Research Institute; 2011
- [74] Hashizume M, Armstrong B, Wagatsuma Y, Faruque ASG, Hayashi T, Sack DA. Rotavirus infections and climate variability in Dhaka, Bangladesh: A time-series analysis. Epidemiology & Infection. 2008;136(9):1281-1289
- [75] Ebrahim S, Kinra S, Bowen L, Andersen E, Ben-Shlomo Y, Lyngdoh T, Ramakrishnan L, Ahuja RC, Joshi P, Das SM, Mohan M. Correction: The effect of rural-to-urban migration on obesity and diabetes in India: A cross-sectional study. PLoS Medicine. 2010;7(4):1-12
- [76] Granger CW. Investigating causal relations by econometric models and cross-spectral methods. Econometrica: Journal of the Econometric Society. 1969;424-438

Identifying Water Network Anomalies Using Multi Parameters Random Walk: Theory and Practice

Eyal Brill and Barak Brill

Additional information is available at the end of the chapter

<http://dx.doi.org/10.5772/intechopen.71566>

Abstract

A noise pattern analysis is used to demonstrate how water quality events can be classified. The algorithm presented mimics a random walk process in order to measure the level and type of noise in the water quality data. The resulting curve is analyzed and four different cases are identified. i.e. sensor problem, water source change, operational change and contamination. For each problem, the algorithm identifies a different pattern. This pattern can be used later to reduce the level of false alarms in the monitoring system.

Keywords: water network, abnormality detection, multi parameters, clustering, unsupervised learning

1. Introduction

Anomaly detection in multivariate time series, such as water quality data, derived from water quality monitoring stations, is considered a non-trivial task. This is mainly due to the implication involved with both false positive and false negative situations.

In the case of false positive, i.e., the water is declared non-drinkable, and an alternative for customers must be found by the relevant water utility. This type of one-time event may be costly, while repetitive mistakes of this kind will eventually cause the monitoring system to be perceived as unreliable.

In the case of false negative, i.e., the monitoring system failed to detect a problem, some health hazard situations may develop and, in the long run, once again, the monitoring system may be considered unreliable.

Several methods have been suggested as a methodology for detecting abnormal events in similar cases. The basic approach for solving such problems may be based on unsupervised machine learning (USL), As described in detail by Celebi and Aydin [1]. One of the first and most fundamental methods of USL is based on clustering. *Clustering* is a methodology which groups vectors into several similar groups, where the members of each group are as similar as possible and the differences between groups are as great as possible. Clustering may be distance-based or density-based. Examples of distance-based clustering, such as the kMean algorithm, were presented by Knorr and Ng [2, 3] who compute abnormality score by counting neighbors to each point. More updated work in this field was introduced by Angiulli and Pizzuti [4] who compute the anomaly score of a data instance as the sum of its distances from its k-nearest neighbors. Ramaswamy et al. [5] extend this technique to spatial data. Their methods are also based on the kNN algorithm. Bay and Schwabacher [6] introduced the same algorithm with regard to pruning.

Another clustering philosophy is based on density of points. Examples of such cases are Breunig et al. [7, 8], in relation to relative density. Jin et al. [9] showed how some of the calculations can be skipped. Tang et al. [10] further improved clustering by adding the idea of a connectivity-based outlier factor, which refers to the number of connections between points. Jin et al. [9] also introduced improvements by adding the idea of symmetric neighborhood relationship. The main density-based algorithm is known as the EM algorithm.

In both methods - distance or density - the result is a multi-dimensional data structure which contains centroids. A *centroid* is a center of a group. It is, in the broadest sense, the group's center of gravity, i.e., the coordinates of the center of the group in each dimension. Once such a data structure exists, each new incoming record is evaluated based on its distance from the most nearest centroid. If the new incoming record is too far from any known centroid, it is declared a suspicious record, one that should be examined. After examination, the new point is classified, either as a True or False event. This classification is added to the model's learning set.

A second method, which has been used for abnormality detection, is based on a prediction methodology. According to this methodology, one of the variables in a multi-dimensional space is considered to be a dependent variable, whose value or class (in the case of discrete values) is related to the other variables. Given that, a mathematical model is then constructed, which describes the relation between the dependent variable and all other variables. This model can be based, for example, on linear regression, decision trees or neural networks. In this case, each new incoming record is used to generate a prediction. If the predicted value is too far or has a different class value than the actual value of the dependent variable, the new incoming record, is again considered abnormal and must be investigated. An example of such a methodology is given by Stefano et al. [11], Odin and Addison [12], Hawkins et al. [13] and Williams et al. [14].

A third method, which will be the focus of this chapter, is based on examining noise pattern changes, generated by the multi-dimensional data. Several methods have been suggested along this line. A fundamental method has been demonstrated by Cheng et al. [15], which used an RBF¹ function to identify abnormal patterns in a moving window.

¹Radial basis function (see https://en.wikipedia.org/wiki/Radial_basis_function).

The methodology suggested in this chapter is based on Brill [16]. This methodology is based on detection and classification changes in noise patterns. Noise is measured based on the distance traveled by an artificial particle located at the normalized coordinates of the multi-dimensional vector. The difference between Cheng et al. [15] and Brill [16] is in the classification type of the abnormal events. While the first uses a True and False classification, the second adds the hazard and non-hazard classification. As will be demonstrated later in this chapter, patterns in this noise can be explained by different events related to the water network.

The aim of this chapter is to describe a different methodology for abnormality detection in water network. The chapter describes the basic model and presents a numerical illustration of the calculation framework. Then it illustrates four different cases which enable the identification of changes in the noise pattern and their related events. The last section concludes the chapter.

2. The model

The following section presents an overview of the mathematical model used in this chapter. It starts by examining Brownian Motion (BM), which is named after Robert Brown [17], who discovered the typical movement of flowers seeds on the water's surface. Einstein [18] used the idea of BM in order to provide precise details about the movement of atoms. This explanation was later further validated by Perrin who awarded the physics noble price for 1926.

BM was also used by Louis Bachelier [19] (1900) in his Ph.D. thesis "The Theory of Speculation", in which he presented a stochastic analysis of the stock and option markets. His work went on to inspire the novel work of Black and Scholes [20], which awarded them the Nobel Prize in economics.

Modern literature gives many examples of the usage of BM in various areas; most are related to biology, chemistry, physics and other fields of life sciences. However, it is rare that such a technique or a similar one is used for the analysis of abnormal water events - the main topic of the current chapter.

One of the central results of BM theory is an estimation of the traveling distance of a particle, which travels using random movement in a given time interval across a multi-dimensional space. According to this theory, if $\rho(x,m)$ is the density function of particles at location x (were x is a single dimension, e.g., one axis) at time m , then ρ satisfies the diffusion equation:

$$\frac{\partial \rho}{\partial m} = D \frac{\partial^2 \rho}{\partial x^2} \tag{1}$$

where D is the *mass diffusivity*, a term which measures how fast particles of a given type may move in a specific material, in our case, water. The solution of Eq. (1) gives a density function with a first moment, which is seen to vanish, and a second moment given by:

$$\overline{x^2} = 2D * m \tag{2}$$

The left side of Eq. (2) expresses the distance at which a particle can be found from its origin, given the elapsed time m and the diffusivity parameter D . Assuming x is distributed normally, the maximum value a particle can travel for a given time can be calculated using (2) with a given confidence interval.

Using Eq. (2), and assuming that the left hand side of (2) is distributed normally, and its standard deviation (S) can be estimated empirically, the probability of a particle to travel a given distance from its origin within m units of time can be calculated by:

$$L = \sqrt{2D * m} + S * t(\alpha) \quad (3)$$

where $t(\alpha)$ is the confidence interval factor, based on the level of confidence required (drawn from the student distribution). Thus, if a particle is found within m steps at a distance which is greater than L units from its origin, it is considered an abnormal event.

In the physical or chemical diffusion process, the value of D is determined based on material properties, and the value of m is measured in continuous time. In the current model, these values should be determined using another methodology as explained in the following paragraphs.

Let us denote with vector X_m the set of quality measurements of water at each moment m and, assuming X_m has K dimensions. The value of X_m can be normalized with the following process equation:

$$\hat{v}_m^k = \frac{X_m^k - X_{\min}^k}{X_{\max}^k - X_{\min}^k} \quad (4)$$

where v_m^k is the normalized k dimension of vector V_m and m is the discrete time index. The subscripts max and min refer to the maximum and minimum value of this dimension over the whole data set.

Let's also define the distance between two vectors to be denoted by DN_m^n (where DN stands for Dynamic Noise). This measurement is calculated as the normalized Euclidian distance between two values of V_m and is given by the equation

$$DN_m^n = \hat{V}_m - \hat{V}_{m-n}. \quad (5)$$

Note please that unlike in the case of BM where the distance of a particle from its origin increases with time, in the case of the DN, the particle may turn back to its origin.

An illustration of this distance in a normalized two-dimensional space is shown in **Figure 1**. In this case, V_m is a two-dimensional vector.

In terms of **Figure 1**, assuming a dataset with M records and two variables in each record (x_1 and x_2), one may look at this dataset as a description of location for a particle in each time stamp. After normalizing the dataset according to Eq. (4), the Euclidian distance between each two points is the distance this particle travels. If the distance is measured in a five-step gap, the result may be a chart as shown in **Figure 1**.

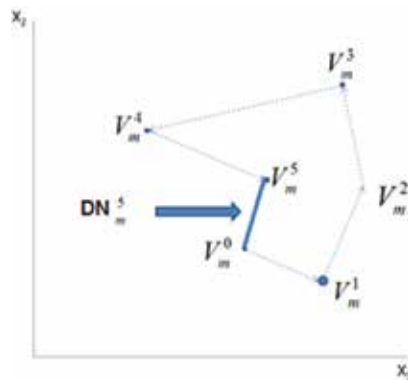


Figure 1. BM distance traveling in two dimensions.

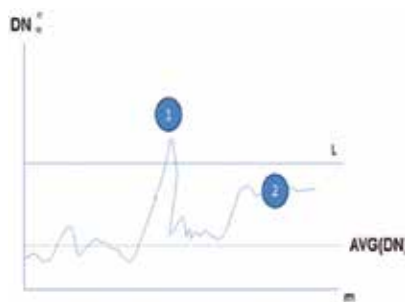


Figure 2. DN over time.

Figure 2 shows a schematic chart of DN_m^n over time without exceeding the L limit. As explained previously, under normal conditions the value of DN_m^n is not expected to go above the value of L , with a confidence level equal to $1 - \alpha$. The value of L can also be obtained. In **Figure 2**, point 1 refers to values of DN above the level of L for a constant period, while point 2 underline a significant change in the value of DN .

The first is calculated by comparing the value of DN_m^n with the result of Eq. (3), as calculated by data accumulated until the m point in time. The second is calculated by comparing the average normalized value of DN_m^n at a fixed-width moving window of DN_m^n with the average DN_m^n known prior to this window.

3. Numerical example

This section numerically describes the calculation procedure as described in the previous section. **Table 1** contains an example data set with 20 records. The measured variables are Free Chlorine (CL), Turbidity (TU), pH and Conductivity (CO). These are a common water quality indicators.

Max	1	1	9.5	600	Normalized data				
Min	0	0	6	300	CL	TU	pH	CO	DN
No	CL	TU	pH	CO	CL	TU	pH	CO	DN
1	0.60	0.09	7.69	536.00	0.60	0.09	0.48	0.79	0.0000
2	0.59	0.09	7.70	541.50	0.59	0.09	0.49	0.81	0.0000
3	0.60	0.08	7.70	538.00	0.60	0.08	0.49	0.79	0.0000
4	0.60	0.09	7.70	538.00	0.60	0.09	0.49	0.79	0.0000
5	0.60	0.09	7.71	538.00	0.60	0.09	0.49	0.79	0.0000
6	0.60	0.08	7.70	537.00	0.60	0.08	0.49	0.79	0.0003
7	0.60	0.09	7.70	536.00	0.60	0.09	0.49	0.79	0.0001
8	0.60	0.12	7.70	535.50	0.60	0.12	0.49	0.79	0.0008
9	0.60	0.12	7.70	536.00	0.60	0.12	0.49	0.79	0.0010
10	0.60	0.09	7.70	533.00	0.60	0.09	0.49	0.78	0.0002
11	0.60	0.09	7.70	533.00	0.60	0.09	0.49	0.78	0.0002
12	0.59	0.08	7.70	529.00	0.59	0.08	0.49	0.76	0.0016
13	0.60	0.08	7.71	529.00	0.60	0.08	0.49	0.76	0.0024
14	0.59	0.09	7.71	545.00	0.59	0.09	0.49	0.82	0.0017
15	0.59	0.09	7.71	545.00	0.59	0.09	0.49	0.82	0.0017
16	0.60	0.09	7.71	545.00	0.60	0.09	0.49	0.82	0.0029
17	0.59	0.08	7.71	544.00	0.59	0.08	0.49	0.81	0.0025
18	0.59	0.09	7.71	545.33	0.59	0.09	0.49	0.82	0.0000
19	0.59	0.08	7.71	540.00	0.59	0.08	0.49	0.80	0.0004
20	0.59	0.08	7.71	538.00	0.59	0.08	0.49	0.79	0.0006

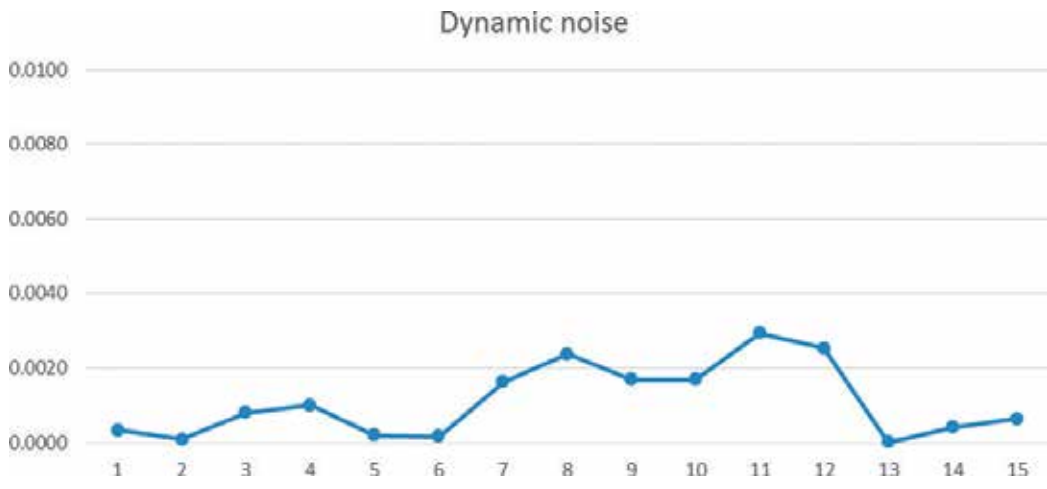


Table 1. Data for numerical example.

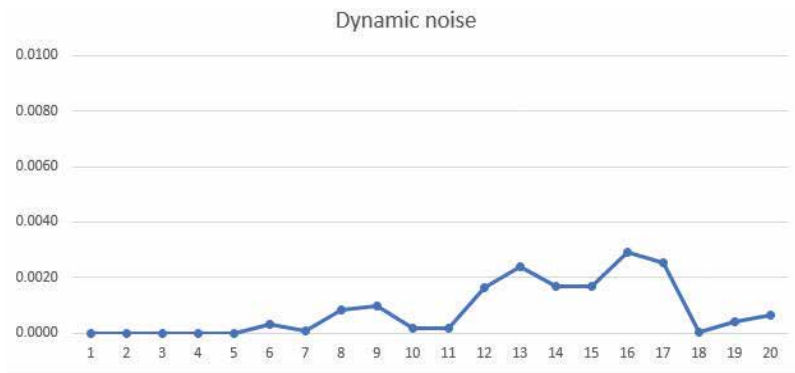


Figure 3. Dynamic noise chart.

The first two rows display the minimum and maximum values of each variable. These values were used to normalize the records in the left side of the table to the right side of the table. After normalization, a vector of the Euclidian Distance between each pair of records with a difference of 5 steps was calculated. This vector is the most right column in the table. The first value in this vector (located in row 6) contains the distance between record 6 to record 1. The second contains the distance between record 7 to record 2. The chart in **Figure 3** displays relevant DN chart.

In the following section, examples from a read data set are used to illustrate the analysis framework of abnormality detection and classification using this methodology.

4. Real data example

The following examples refer to a real data set recorded at a field station with measurements, as presented in **Table 2**. The table’s quality measurements include Free Chlorine (Cl measured in ppm), Turbidity (TU measured in NTU), pH, Conductivity (CO measured in mS), and pressure (PRI measured in bars). For each measurement, the algorithm dynamically calculates the minimum and maximum values of the last 48 hours. (see first two rows of **Table 1**).

Symbol	Measurement	Units	Minimum	Maximum
Cl	Free Chlorine	mA	0	2
TU	Turbidity	NTU	0	2
pH	pH	pH	6	9.5
CO	Conductivity	mS	0	800
PRI	Pressure	Bar	0	15

Table 2. Measurements.

Typical minimum and maximum values are shown in **Table 2**. Given these minimum and maximum values, the raw measurements are transformed into normalized measurements, as shown by Eq. (4) of Section 2. The normalized measurements are used to calculate the “Dynamic Noise”, as shown in Eq. (5), with a lag difference between the records of 10 time-stamps. **Figure 4** shows the distribution of the dynamic noise values.

As can be seen from the histogram, a value which is more than 0.25 is rare (see red arrow). Hence, the threshold for the dynamic noise was set to 0.3. In terms of Section 2 of this chapter, $L = 0.3$.

The first data analysis step with regard to the dynamic noise algorithm is to estimate the normal conditions, i.e., to observe how a dynamic noise curve behave in case of a normal data flow. **Figure 5** shows a normal period of time for the four water quality measurements. Note that pH ranges between 7.70 and 7.79; Free Chlorine ranges between 0.37 and 0.48; Conductivity usually has an average of around 520–530 with short drops to 450; and Turbidity ranges between 0.09 and 0.12.

Figure 6 shows the equivalent dynamic noise for the relevant measurements. As can be seen, the values range between 0.03 and 0.25 at the most.

We will now discuss four different cases, in which the dynamic noise violation threshold is analyzed. Note please that violation of the threshold L triggers an alarm only after a delay time in which the value of the DN is above the level of L . This in order to avoid false alarms caused by short spikes.

Case 4.1: Malfunctioning of sensors

The first case shows a situation in which two of the sensors stopped functioning for a short period of time. As can be seen from **Figure 7**, the Cl and the pH dropped suddenly to zero for a short period. This may result from communication problems, which are very common with distributed I/O.

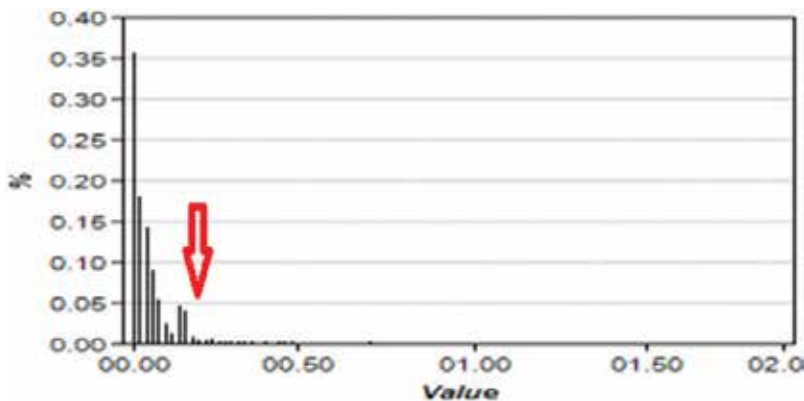


Figure 4. DN histogram.

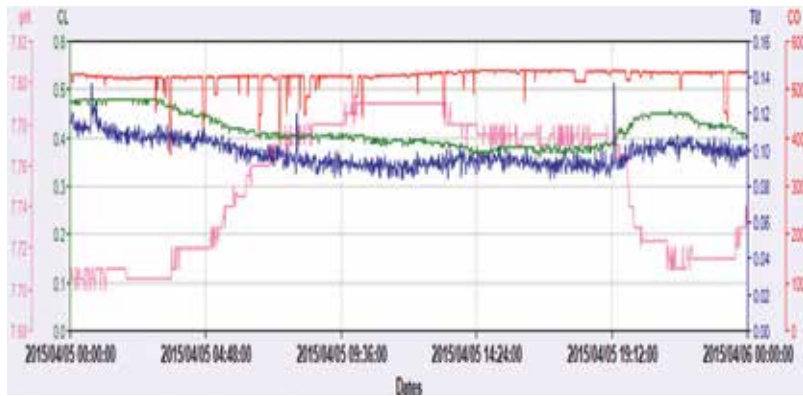


Figure 5. Normal measurements.

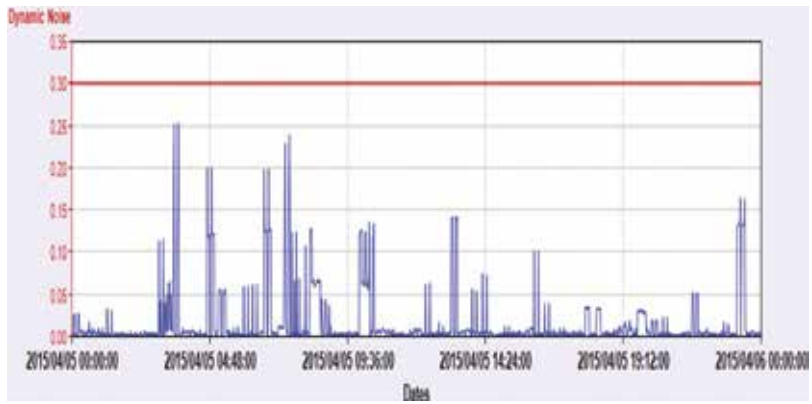


Figure 6. DN for normal measurements.



Figure 7. Malfunctioning of sensors.

Figure 8 shows the resulting dynamic noise curve of the sensor's malfunctioning. As can be seen, the drop in the values of Cl and pH causes a sharp increase in the value of the dynamic noise. After a short period, when the sensors resume functioning, the value of the dynamic noise drops back to a level below the red threshold line (0.3).

Note also that if the sensors remain non-functional for a long period of time, and the algorithm stops using the values of these sensors as part of Eq. (5), the level of the dynamic noise curve will be lower during steady state, since less sensors are transmitting data.

The gray box around the area of the event depicts the shape of the dynamic noise curve as a rectangle. This is due to the sharp change in the values of certain sensors. This sharp change can only occur during sensor failure. A chemical change in water quality cannot occur within 1 minute.

Case 4.2: Operational change

The second typical change is an *operational change*. This is defined as a situation in which one of the variables controlled by operators has been changed. Some examples of such variables may be pressure or flow. An operational change may influence the variables' quality. One such example of this type of situation is shown in **Figure 9**. The black line shows a change in the pressure (PRI) value. Shortly after this change, a peak in the Turbidity value is recorded (see red line in **Figure 9**).

Figure 10 shows the corresponding changes in the dynamic noise curve. The chart indicates that the operational change also results in the violation of the dynamic noise's "red line". However, this can be explained by the change in the operational variable.

Since operational changes are also sudden changes, the peak in the dynamic noise curve is immediate. However, the return to normal happens gradually. This is the reason why the gray area has a triangular shape in **Figure 10**.

Case 4.3: Water source change

The third case illustrates what happens when a change is made to the water source. In this case, if the attributes of the water from the new source are different, the footsteps of the water source change can also be seen in the dynamic change curve.

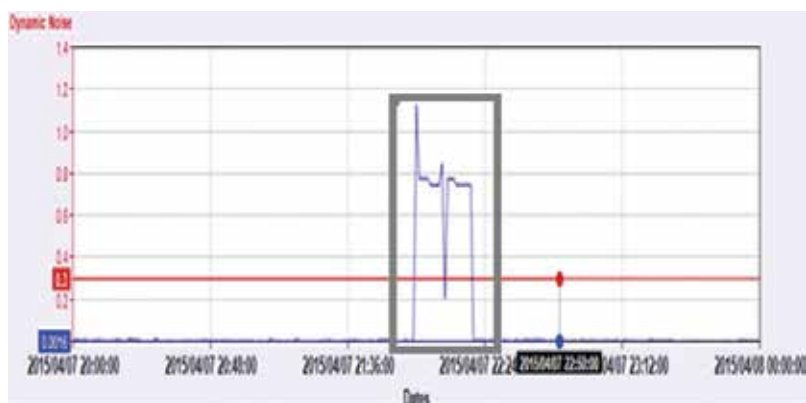


Figure 8. Noise curve for sensor malfunctioning.

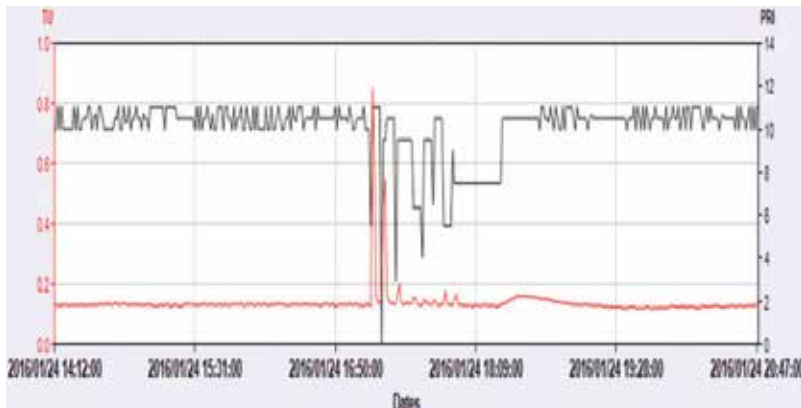


Figure 9. Operational change - raw data.

Figure 11 shows a change in the water source. Conductivity rose from a level of 345 mS to a level of 385 mS (within 6 hours, from 10:00 am to 4:30 pm). Together with this, the pH level dropped from 8.20 to 8.07.

The effect on the dynamic noise curve can be seen in Figure 12. The average value of the dynamic noise curve has changed. This is due to the change in the noise level of the water measurements from the new source.

A change in water source, which can take between 30 and 60 minutes and up to several hours, will result in a change in the noise of the dynamic noise curve. Sometimes, it will also cause a change to occur in the average value of the dynamic noise.

Case 4.4: Contamination event

Finally, we have the case of contamination. Figure 13 shows raw data from a typical contamination event. The event starts with a drop in the Free Chlorine (see green line in Figure 13). This is due to chlorine consumption by the contaminator. Shortly after, the Turbidity level starts to rise (see blue line in Figure 13).

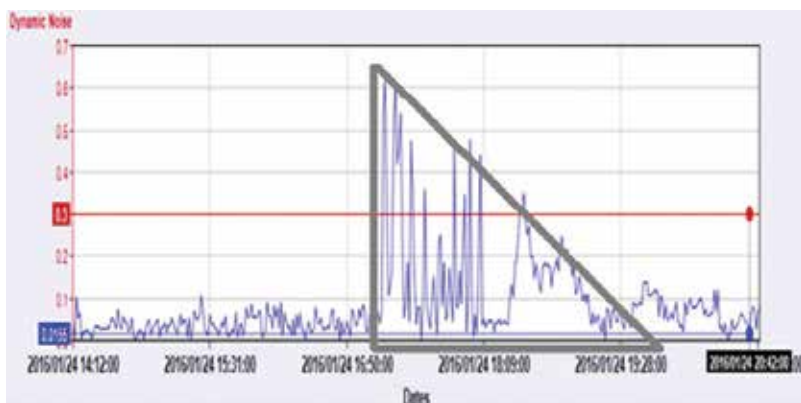


Figure 10. Operational change - dynamic noise curve.

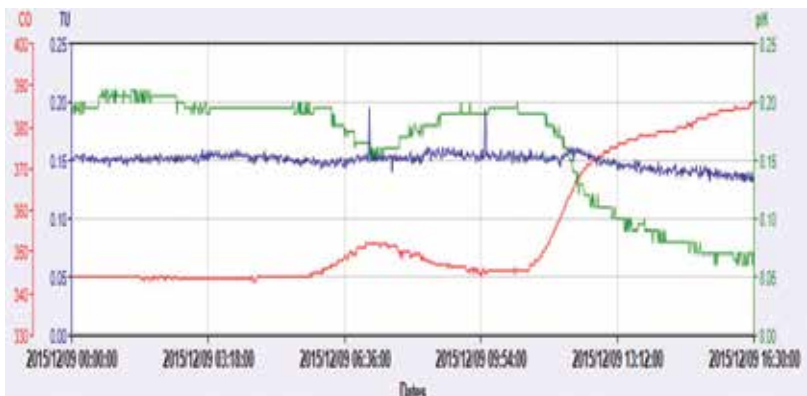


Figure 11. Water source change - raw data.

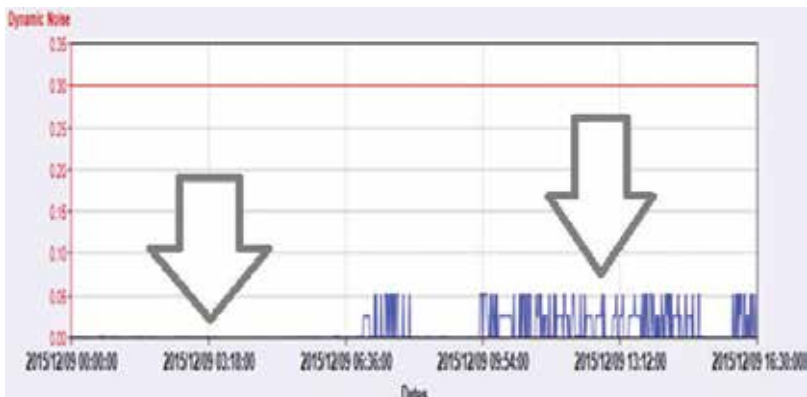


Figure 12. Water source change - dynamic noise.

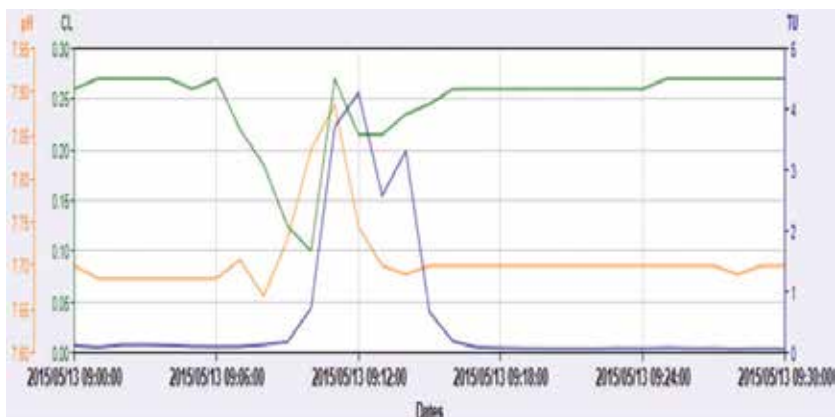


Figure 13. Contamination event - raw data.



Figure 14. Contamination event - dynamic noise.

At the same time, the chlorination dosing system reacts to the situation and the level of Free Chlorine once again rises to a normal level; and due to the diffusion factor, the Turbidity level gradually drops. The result of this event can be seen in the dynamic noise line shown in **Figure 14**.

As seen in **Figure 14**, when the event starts, the dynamic noise curve rapidly rises above the red line of the threshold. It is fast, but not steep, as in the case of sensor malfunctioning or water source change. Once the maximum level of contamination has been obtained, the level starts to gradually drop, due to the diffusion effect, which causes the contamination to be diluted with the incoming water. This is why the right side of the curve in **Figure 14** is not symmetric to the left side of the blue curve. The overall situation creates the shape of non-symmetric triangle, as is illustrated by the gray area in **Figure 14**. Note that the farther the contamination's penetration to the system is from the measuring point, the less non-symmetric and the shorter the triangle will be. This is due to the dilution effect.

5. Concluding remarks

The current chapter demonstrates how the simple pattern recognition of a curve created by a noise capture process, similar to a random walk, can be used to classify different types of abnormal events. The presented algorithm uses the imaginary center of gravity of the water quality measurements in order to measure the noise of the process captured as traveling distance. It has been shown that the created curve has a maximum value, due to the nature of the process. This threshold is violated when abnormal events occur.

Four different types of abnormal events were examined: malfunctioning of sensors, operational change, water source change and contamination events. Numerical examples based on real data show that each of the events has a different "signature", which enables the identification of the event's nature.

The current chapter shows how water analytics can be used as part of the information system which helps operators protect the water system. The above framework can also assist control systems in regard to the automatic classification process of observed events, in order to reduce the level of false alarms in water monitoring systems. For example, this may be achieved by eliminating alarms like the first three types analyzed in this study and notifying operators only in the case of contamination event alarms.

Author details

Eyal Brill^{1*} and Barak Brill²

*Address all correspondence to: eyalb@hit.ac.il

1 Faculty of Technology Management, Holon Institute of Technology, Israel

2 Department of Statistics and Operations Research Tel Aviv University, Israel

References

- [1] Emre Celebi M, Aydin K. *Unsupervised Learning Algorithms*. Springer International Publishing, Switserland; 2016. ISBN: 978-3-319-24211-8
- [2] Knorr EM, Ng RT. A unified approach for mining outliers. In: Proc. Conf. of the Centre for Advanced Studies on Collaborative Research (CASCON), Toronto, Canada; 1997
- [3] Knorr EM, Ng RT. Algorithms for mining distance-based outliers in large datasets. In: Proc. Int. Conf. on Very Large Data Bases (VLDB), New York, NY; 1998
- [4] Angiulli F, Pizzuti C. Fast outlier detection in high dimensional spaces. In: Proc. European Conf. on Principles of Knowledge Discovery and Data Mining, Helsinki, Finland; 2002
- [5] Ramaswamy S, Rastogi R, Shim K. Efficient algorithms for mining outliers from large data sets. In: Proc. ACM SIGMOD Int. Conf. on Management of Data (SIGMOD), Dallas, TX; 2000
- [6] Bay SD, Schwabacher M. Mining distance-based outliers in near linear time with randomization and a simple pruning rule. In: Proc. Int. Conf. on Knowledge Discovery and Data Mining (KDD), Washington, DC; 2003
- [7] Breunig MM, Kriegel H-P, Ng RT, Sander J. OPTICS-OF: Identifying local outliers. In: Proc. European Conf. on Principles of Data Mining and Knowledge Discovery (PKDD), Prague, Czech Republic; 1999
- [8] Breunig MM, Kriegel H-P, Ng RT, Sander J. LOF: Identifying density-based local outliers. In: Proc. ACM SIGMOD Int. Conf. on Management of Data (SIGMOD), Dallas, TX; 2000

- [9] Jin W, Tung A, Han J. Mining top-n local outliers in large databases. In: Proc. ACM SIGKDD Int. Conf. on Knowledge Discovery and Data Mining (SIGKDD), San Francisco, CA. 2001
- [10] Tang J, Li H, Cao Y, Tang Z. Email data cleaning. In: KDD'05, August 21-24, 2005, Chicago, Illinois, USA. Copyright 2005 ACM 1-59593-135-X/05/0008; 2005
- [11] Stefano C, Sansone C, Vento M. To reject or not to reject: That is the question: An answer in the case of neural classifiers. *IEEE Transactions on Systems, Man, and Cybernetics, Part C (Applications and Reviews)*. 2000;**30**(1):84-94
- [12] Odin T, Addison D. Novelty detection using neural network technology. In: Proceedings of the COMADEN Conference; 2000
- [13] Hawkins S, He H, Williams GJ, Baxter RA. Outlier detection using replicator neural networks. In: Proceedings of the 4th International Conference on Data Warehousing and Knowledge Discovery. Aix-en-Provence, France, September 4-6, 2002. pp. 170-180
- [14] Williams G, Baxter R, He H, Hawkins S, Gu L. A comparative study of RNN for outlier detection in data mining. In: Proceedings of the IEEE International Conference on Data Mining. IEEE Computer Society, Maebashi City, Japan, December 2002; p. 709
- [15] Cheng H, Tan P-N, Potter C, Klooster S. Detection and characterization of anomalies in multivariate time series Haibin Cheng, Pang Ning Tan, Christopher Potter, Steven Klooster. In: Proceedings of the 2009 SIAM International Conference on Data Mining; 2009
- [16] Brill E. Dynamic Brownian motion with Density superposition for abnormality detection. PCT. Application number: 14601862; 2015
- [17] Brown R. A brief account of microscopical observations made in the months of June, July and August 1827, on the particles contained in the pollen of plants; and on the general existence of active molecules in organic and inorganic bodies. *The Philosophical Magazine*. 2009;**4**:161-173. DOI: 10.1080/14786442808674769
- [18] Einstein A. Investigations on the theory of Brownian movement. *Annalen der Physik*. 1905;**322**(8):549-560
- [19] Davis M, Etheridge A. Louis Bachelier's Theory of Speculation: The Origins of Modern Finance. Princeton; Oxford: Princeton University Press, JSTOR; 2006
- [20] Black F, Scholes M. The pricing of options and corporate liabilities. *Journal of Political Economy*. 1973;**81**(3):637-654

Segmentation of Water Body and Lakeshore Changes behind an Island Owing to Wind Waves

Takaaki Uda, Masumi Serizawa and Shiho Miyahara

Additional information is available at the end of the chapter

<http://dx.doi.org/10.5772/intechopen.72550>

Abstract

In a slender water body with a large aspect ratio, the angle of wind waves relative to the direction normal to the shoreline may exceed 45° , resulting in the emergence of cusped forelands and the segmentation of the water body. The BG model was used to predict the segmentation of a rectangular water body by wind waves when the probability of occurrence of the wind direction is given by a circular or elliptic distribution, and the segmentation of a rectangular water body into a circular or elliptic lake was predicted in each case. The segmentation of a shallow water body with a triangular or crescent shape was also predicted together with the prediction of lakeshore changes when a rocky or sandy island exists in a circular lake.

Keywords: closed water body, wind waves, segmentation, lakeshore changes, BG model, cusped foreland, island

1. Introduction

In a shallow water body, beach changes may take place owing to wind waves. In a narrow water body with a large aspect ratio, the angle of wind waves relative to the direction normal to the shoreline may exceed 45° , and the shoreline may become unstable because the fetch distance in the direction of the principal axis of the water body is sufficiently large for waves with significant energy to be generated [1, 2]. Therefore, cusped forelands that develop from both shores of a narrow water body connect with each other, resulting in the segmentation of the water body into smaller rounded lakes [3, 4]. For example, **Figure 1** shows the segmentation of a lagoon facing the Chukchi Sea in Russia [3, 4]. In this example, five elliptic lakes can be observed as a result of segmentation, and their axes are parallel to each other. **Figure 2** shows an enlarged satellite image of the rectangular area in **Figure 1**, and in this image, lake segmentation at a primitive



Figure 1. Example of segmentation of slender water body: Lagoons facing Chukchi Sea [3, 4].

stage can be seen with the alternate development of cusped forelands. Regarding these phenomena, the division and reduction of the fetch distance owing to the formation of a large shoreline protrusion associated with shoreline instability under high-wave-angle conditions and the resulting change in the wave field are key factors. Ashton et al. [4] predicted that the forelands formed along the shoreline connect with each other, resulting in the segmentation of the water body into smaller rounded lakes. Uda et al. [5] predicted the three-dimensional (3-D) segmentation of a shallow rectangular water body using the BG model (a model for predicting 3-D beach changes based on Bagnold's concept) [6]. Uda et al. studied the emergence and mergence of small lakes and their segmentation using the same model [7], assuming that the wind blew from all directions between 0 and 360° with the same probability of occurrence and intensity, that is, a circular distribution of the probability. The segmentation into elliptic shapes, as shown in **Figure 1**, was not predicted in their study. It may be accomplished, assuming that the probability of occurrence of the wind direction is given by an elliptic distribution, similarly to the case of oriented lakes [8]. In this study, the segmentation of a rectangular water body was predicted, given a circular or elliptic distribution of the probability of occurrence of the wind direction.

In the coastal area, the segmentation of a shallow water body with a triangular or crescent shape can also be observed. To study the mechanism of segmentation of such a water body, several examples of segmentation together with the development of sand spits along the lake-shore were examined in Lagoa de Mangueira in Brazil, Lake Saroma and Lake Kitaura in



Figure 2. Enlarged satellite image of rectangular area in **Figure 1**.

Japan. Then, the BG model was used to investigate the segmentation of a shallow water body with a triangular or crescent shape, and 3-D beach changes during the segmentation of a shallow water body into small lakes were predicted.

When wind waves are incident to the lakeshore in a closed water body with a rocky or sandy island, topographic changes may occur on the lee of the island because of the wave-sheltering effect. Since a rocky island is fixed at a location in a closed water body, the wave-sheltering effect of the island is constant with time, and the lakeshore converges to a certain stable form after the wave action for a sufficiently long time. When a sandy island is located in a closed water body, however, the island itself can deform owing to the action of wind waves, resulting in the successive change in wave field. Thus, more complicated lakeshore changes will occur. Here, Lake Balkhash located in Kazakhstan [9] was selected as an example, and the BG model was used for predicting lakeshore changes when a rocky or sandy island exists in a circular lake.

2. Examples of cusped forelands in lake

2.1. Lakeshore in Lagoa de Mangueira

Figure 3 shows an example of segmentation and the development of sand spits along the lakeshore of Lagoa de Mangueira (location: 33°09'59"S, 52°49'32"W) in Brazil [7]. The crescent lake is 100 km long and 10 km wide at the center of the lake. Many cusped forelands have developed along the lakeshore and, in particular, the intervals of the cusped forelands formed on the west shore become short near the south end of the lake. On the other hand, sand spits with similar shapes and cusped forelands have developed along the east and west shores, respectively, in the north part of the lake. This is a typical example of segmentation and the development of sand spits in a crescent lake.

2.2. Lakeshore in Lake Saroma

Figure 4 shows a satellite image of an abandoned inlet located at the east end of Lake Saroma in Hokkaido, Japan (Location: 44°08'03"N, 143°59'04"E) [10]. This water body has a triangular shape, and segmentation of a water body can be seen near the east end. When enlarging the rectangular area in the satellite image of **Figures 4** and **5** is obtained. For the wind rose in Lake Saroma, the predominant wind direction is WNW, resulting in the eastward development of sand spits. On the south shore is Tofutsu fishing port, as shown in **Figure 5**. East of



Figure 3. Segmentation and development of sand spits along lakeshore of Lagoa de Mangueira in Brazil [7].



Figure 4. Study area in eastern Lake Saroma [10].

this fishing port, the width of the water body gradually decreases, and sand spits A-E develop together with pairs of sand spits A' and E'. Of these sand spits, sand spits A and A' are the largest and divide the water body into two. In the vicinity of sand spit A', wind waves cannot be generated in the presence of the westerly wind, resulting in no development of sand spits. However, east of sand spit A', wind waves can develop, and the size of the sand spits increases eastward in the order of sand spits B, C, and D.

2.3. Lakeshore in Lake Kitaura

Lake Kitaura located in Ibaraki Prefecture is a shallow lake with an area of 35.2 km² and 25 km length in the north-south direction, as shown in **Figure 6**. The formation of cusped forelands in this lake was discussed in [5], and here we refer this results. This lake is located in the lowland surrounded by Kashima and Namegata tablelands with elevations of 40 and 30 m on the east and west sides, respectively. Thus, wind waves can be generated without a significant sheltering effect by hills or mountains. Because the direction of the principal axis of Lake



Figure 5. Enlarged satellite image of rectangular area in **Figure 4**, and sand spits A-E and E' [10].



Figure 6. Cusped forelands developed along lakeshore of Lake Kitaura in Japan [5].

Kitaura is N18°W, the predominant wind of NNE blows at an angle of 40.5° clockwise relative to the direction of the principal axis. Because of this oblique wind direction, wind waves are incident at a large incidence angle to the shoreline, resulting in the formation of the protruding shoreline on the west shore. In particular, an enlarged satellite image of two subareas, **a** and **b**, in Figure 6 is shown in Figure 7. In subarea **a**, cusped forelands and the ridges develop out of phase, and this condition is very similar to that in the lagoon facing the Chukchi Sea, as shown in Figure 2. Similarly, the cusped forelands on both shores extend out of phase in subarea **b**. This shows a typical example of segmentation and the development of sand spits in a triangular lake.

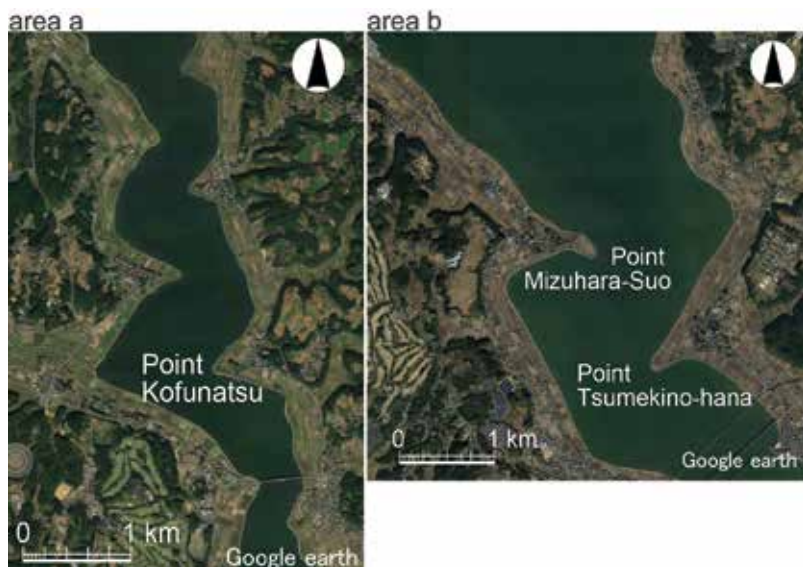


Figure 7. Enlarged satellite images of areas a and b in Lake Kitaura [5].



Figure 8. Satellite image of Lake Balkhash in Kazakhstan.

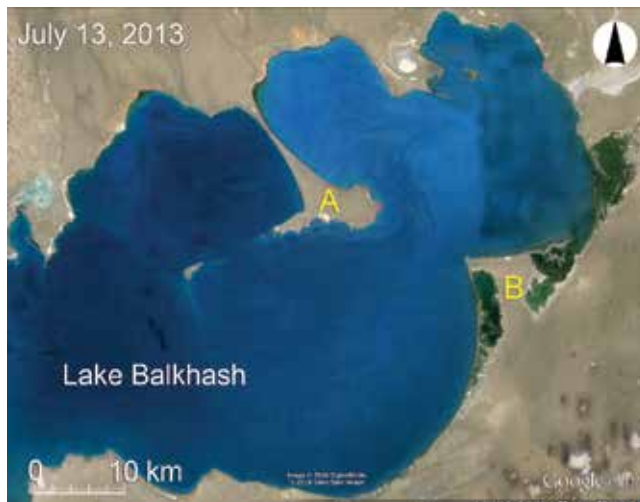


Figure 9. Enlarged satellite image of Lake Balkhash.

2.4. Lake Balkhash

Lake Balkhash has 450 and 200 km lengths in the E-W and S-N directions, respectively (**Figure 8**). **Figure 9** shows an enlarged satellite image of the rectangular area in **Figure 8**. Island A is located at a location of $46^{\circ}34'53.99''\text{N}$ and $78^{\circ}50'17.47''\text{E}$ at the central part of the lake near the east end, and a cuspate foreland of 14 km length extends between island A and the lakeshore. On the shore opposite to island A, a triangular cuspate foreland B is formed with a barrier island. The sand bar extending northwestward from Island A is symmetric with respect to the centerline of the cuspate foreland, and the length of the sand bar is longer than the width of the island. From this, it is inferred that the cuspate foreland extended from the land to Island A by the sand supply from Island A and the land, and connected to Island A.

3. Model for predicting lakeshore changes

For the calculation of the segmentation of a rectangular water body, the BG model employed for the calculation of oriented lakes [8] was used. Given a local fetch distance F at a given point (g is the acceleration due to gravity and U is the wind velocity), the significant wave height $H_{1/3}$ was calculated using Wilson's formula [11, 12].

$$H_{1/3} = f(F, U) = 0.30 \left\{ 1 - \left[1 + 0.004 (gF/U^2)^{1/2} \right]^{-2} \right\} (U^2/g) \quad (1)$$

In this calculation, a coordinate system (x_w, y_w) was set corresponding to the wave direction instead of a fixed coordinate system (x, y) for the calculation of beach changes with the rectangular calculation domain, ABCD, as shown in **Figure 10**, and the wave height was calculated in the rectangular domain A'B'C'D' including the domain ABCD. Neglecting the wave refraction effect, waves were assumed to propagate in the same direction as the wind. The fetch distance F was added from upwind to downwind along the x_w -axis using Eq. (2) when the x_w -axis was divided by mesh intervals Δx_w [13]. Here, the index i in Eq. (2a) is the mesh number along the x_w -axis.

$$F^{(i+1)} = F^{(i)} + r\Delta x_w \quad (2a)$$

$$r = \begin{cases} 1 & (Z \leq 0) \\ 0 & (Z > 0) \end{cases} \quad (2b)$$

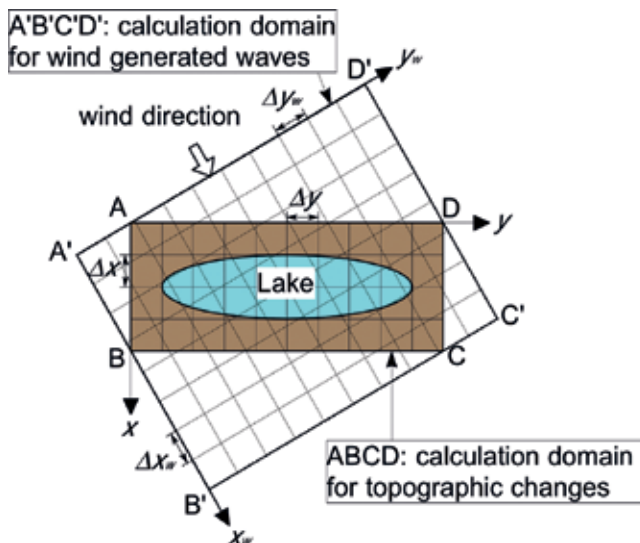


Figure 10. Selection of coordinate system (x, y) adopted for calculation of beach changes with rectangular calculation domain ABCD and another coordinate system (x_w, y_w) [13].

When a grid point was located on land and the downslope condition of $dZ/dx_w \leq 0$ was satisfied, the local fetch was reset as $F = 0$ (Eq. (3)).

$$F^{(i)} = 0 \quad (\text{if } Z \geq 0 \text{ and } dZ/dx_w \leq 0) \quad (3)$$

When the grid point was located in the lake, F was recalculated. By this procedure, the wave height becomes 0 on the lee of the cusped forelands, and the wave-sheltering effect alone can be evaluated.

For the sand transport equation, Eq. (4), which is expressed using the wave energy at the breaking point, was used [6].

$$\vec{q} = C_0 \frac{K_s P}{\tan\beta_c} \left\{ \tan\beta_w \vec{e}_w - |\cos\alpha| \vec{\nabla}Z \right\} \quad (-h_c \leq Z \leq h_R) \quad (4)$$

$$P = \varepsilon(Z) (EC_g)_b \tan\beta_w \quad (5)$$

$$\tan\beta_w = dZ/dx_w \quad (\tan\beta_w \geq 0) \quad (6)$$

Here, $\vec{q} = (q_x, q_y)$ is the net sand transport flux, $Z(x, y, t)$ is the seabed elevation with reference to the still water level ($Z=0$), $\vec{\nabla}Z = (\partial Z/\partial x, \partial Z/\partial y)$ is the seabed slope vector, \vec{e}_w the unit vector of the wave direction, α is the angle between the wave direction and the direction normal to the contour line, and $|\cos\alpha| = |\vec{e}_w \cdot \vec{\nabla}Z|/|\vec{\nabla}Z|$. $\tan\beta_c$ is the equilibrium slope of sand, and K_s is the longshore and cross-shore sand transport coefficient. The P value in Eq. (5) is the wave dissipation ratio per unit area of the seabed and time between $Z = -h_c$ and h_R where sand movement occurs [6], and $(EC_g)_b$ is the wave energy flux at the breaking point. x_w is the coordinate in the direction of wave propagation, and $\tan\beta_w$ is set to 0 when $\tan\beta_w < 0$ is satisfied. $\tan\beta_w$ is the seabed slope measured in the direction of wave propagation. In the calculation, the local beach slope measured along the wave ray was used for the beach slope in Eq. (5), as shown in Eq. (6). h_c is the depth of closure, and h_R is the berm height. C_0 is the coefficient for transforming the immersed weight expression to the volumetric expression ($C_0 = 1/[(\rho_s - \rho)g(1-p)]$; ρ is the seawater density, ρ_s is the specific gravity of sand, p is the sand porosity, g is the acceleration due to gravity), $\varepsilon(Z)$ in Eq. (5) is the depth distribution of sand transport and is defined so as to satisfy Eq. (7); in this study, a uniform distribution was employed (Eq. (8)).

$$\int_{-h_c}^{h_R} \varepsilon(Z) dZ = 1 \quad (7)$$

$$\varepsilon(Z) = 1/(h_c + h_R) \quad (-h_c \leq Z \leq h_R) \quad (8)$$

If $H_{1/3}$ is approximately equal to the breaker height H_b and γ is the ratio of the breaker height to water depth, the wave energy flux at the breaking point $(EC_g)_b$ in Eq. (5) can be written as Eq. (9a).

$$(EC_g)_b = C_1 (H_b)^{\frac{5}{2}} \approx C_1 (H_{1/3})^{\frac{5}{2}} \quad (9a)$$

$$C_1 = \frac{\rho g}{k_1} \sqrt{g/\gamma} \quad (k_1 = (4.004)^2, \gamma = 0.8) \quad (9b)$$

When F and $H_{1/3}$ are calculated using the coordinate system (x_w, y_w) according to the wave direction, the wave power P (Eq. (5)) can be calculated and assigned to each grid point on the coordinate system (x_w, y_w) . The wave power P at each grid point in the calculation of beach changes was interpolated from this distribution of P . The mesh intervals $(\Delta x_w, \Delta y_w)$ in the coordinate system (x_w, y_w) were taken to be the same as $(\Delta x, \Delta y)$. Finally, the sand transport and continuity equations were solved on the x - y plane by the explicit finite-difference method using a staggered mesh scheme. In this study, the wind direction at each step in the calculation of beach changes was selected to be a value determined by random numbers so as to satisfy the probability distribution function of the occurrence of a certain wind direction, although the wind velocity was assumed to be constant.

In estimating the intensity of sand transport near the berm top and at the depth of closure, the intensity of sand transport was linearly reduced to 0 near the berm height or the depth of closure to prevent sand from being deposited in the zone higher than the berm height and the beach from being eroded in the zone deeper than the depth of closure [14].

4. Calculation conditions

Lakeshore changes in a rectangular water body with an aspect ratio of 5 owing to wind waves were first predicted when wind blew from all directions between 0 and 360° with the same probability of occurrence and intensity (Case 1) or blew at an angle of 45° relative to the principal axis of the rectangular water body with an elliptic probability of occurrence and intensity (Case 2), as shown in **Figure 11** [13]. Then, lakeshore changes in triangle- and crescent-shaped shallow water bodies with a flatbed were predicted in Cases 3 and 4, respectively. In all cases, the water depth of the flatbed, the berm height, and the initial beach slope were set to 3 m, 1 m, and 1/20, respectively. **Figure 12** shows the initial topography in each case. Random perturbations with

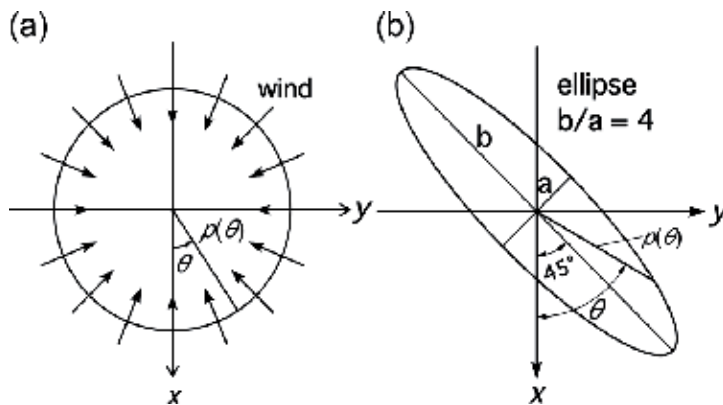


Figure 11. Probability distribution of occurrence of wind direction: (a) circular and (b) elliptic [13].

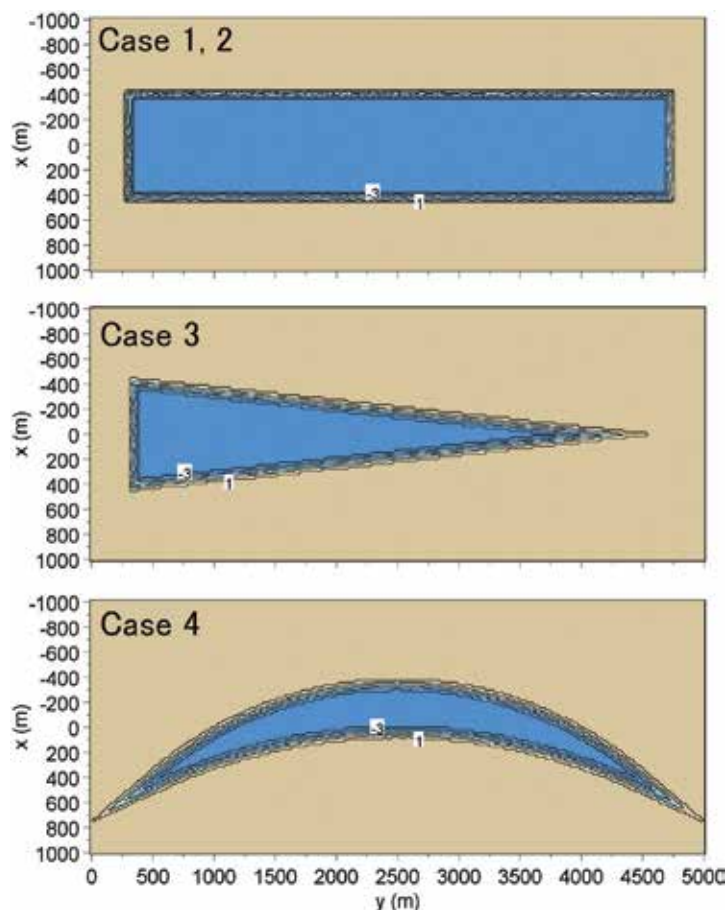


Figure 12. Initial topographies in Cases 1–4.

the amplitude $\Delta Z = 0.1$ m were added to the slope between $Z = 1$ and -3 m in the initial bathymetry. The wind velocity was 20 m/s. The calculation domain was discretized by $\Delta x = \Delta y = 20$ m with $\Delta t = 10$ h. The depth distribution of sand transport was assumed to be a uniform distribution throughout the depth, and the equilibrium slope was $1/20$. **Table 1** shows the calculation conditions for Cases 1–4. The wind velocity of 20 m/s is the value at which a significant wave height of approximately 1 m, the same as the berm height, could be generated, given the fetch distance of 4.6 km, being the distance along the diagonal of the initial rectangular water body in Cases 1 and 2. In Cases 3 and 4, the wind velocity was also assumed to be 20 m/s, and wind was assumed to blow from all directions with the same probability and intensity.

In predicting lakeshore changes when a rocky or sandy island is located in a closed water body, four calculations were carried out, as shown in **Figure 13**. In each case, a circular lake with a radius of 1000 m and a solid bottom of a constant depth of 3 m was set for the calculation domain. In this circular lake, a rocky or sandy island with a radius of 200 m was set at locations deviating from the center of the lake. The foreshore slope of the lakeshore was assumed to be $1/20$. In the present study, the incident angle of waves to the mean shoreline exceeds 45° at

Wind velocity	20 m/s
Berm height, h_R	1 m
Depth of closure, h_c	3 m
Equilibrium slope, $\tan\beta_c$	1/20
Coefficient of sand transport	$K_s = 0.2$
Calculation cases	Case 1: rectangular water body, circular probability distribution Case 2: rectangular water body, elliptic probability distribution Case 3: segmentation of a triangular water body Case 4: segmentation of a crescent-shaped water body Cases 5–8: topographic changes around an island located in a circular lake
Mesh size	$\Delta x = \Delta y = 20$ m
Time intervals	$\Delta t = 10$ h
Duration of calculation	10^6 h (10^5 steps) in Cases 1–4, 5×10^5 h (5×10^4 steps) in Cases 5–8
Boundary conditions	Shoreward and landward ends, $q_x = 0$ Right and left boundaries, $q_y = 0$

Table 1. Calculation conditions.

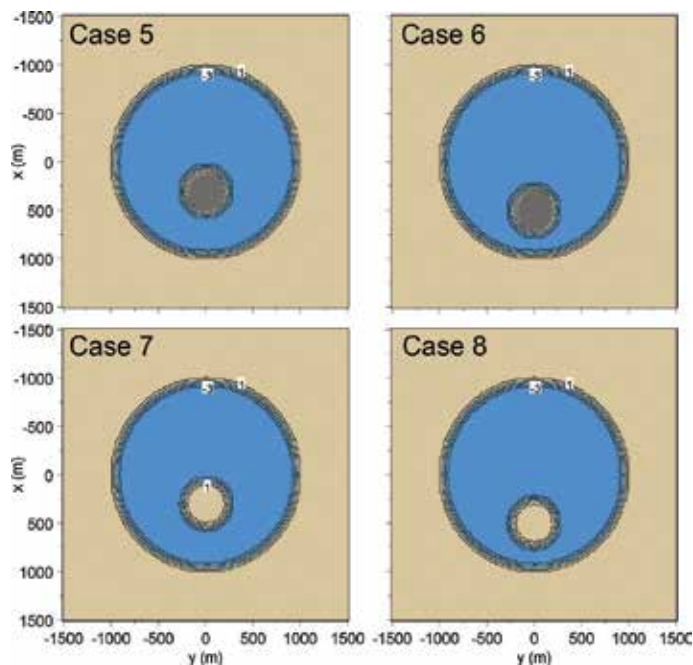


Figure 13. Arrangement of island in Cases 5–8.

certain locations of the lakeshore, resulting in shoreline instability. Therefore, a small perturbation with the amplitude $\Delta Z = 0.1$ m was added in the depth zone between $Z = -3$ and 1 m. In Cases 5 and 6, a rocky island was placed with its center deviating from the center of lake, and the wave-sheltering effect by the island was enhanced in Case 6, in which the island was set at a location closer to the lakeshore. In Cases 7 and 8, the arrangement of the island is the same as those in Cases 5 and 6, respectively, but the island is composed of sand. The other conditions are the same as those in Cases 1–4. **Table 1** shows the calculation conditions for Cases 5–8.

5. Results

5.1. Segmentation of water body given circular distribution of probability (Case 1)

Figure 14 shows the calculation results for the segmentation of a slender, rectangular water body with a longshore length of 4.5 km, and a width of 0.9 km (aspect ratio = 5), assuming that the probability of occurrence of wind direction was given by a circular distribution [13]. When wind waves were incident to the lakeshore, several cusped forelands with irregular shapes developed along the shoreline in the beginning. After 2×10^4 steps, the cusped forelands merged with each other, resulting in a reduction in their number, and sand bars with a hound's-tooth shape were formed. This development of cusped forelands well explains the formation of the lakeshore, as shown in **Figure 2**. After 4×10^4 steps, sand bars extended to the opposite shores, and the water body was about to separate into two lakes, and then the water body had separated into two completely independent lakes. Finally, two completely rounded lakes were formed.

The distributions of the wave height and longshore sand transport alter in response to the wind direction at each time. The formation of cusped forelands and rounded lakes over time, however, strongly depends on the mean $(H_{1/3})^{5/2}$ flux averaged over a significantly long time [13]. **Figure 15** shows the mean $(H_{1/3})^{5/2}$ flux averaged over 10^3 steps at six stages between 1×10^3 and 1×10^5 steps. The arrows in the figure show the direction of the flux, and the color corresponds to the intensity of the flux. After 10^3 steps, outward flux was generated radially from the central part of the lake with a symmetric distribution, and the time-averaged flux at the central part was 0 because of the cancelation of the sum of the vectors. After 2×10^4 steps, the mean $(H_{1/3})^{5/2}$ flux was equivalent on both sides of the central cusped foreland, facilitating the development of the cusped foreland. After 4×10^4 steps, the cusped forelands had further developed, and the direction of the mean $(H_{1/3})^{5/2}$ flux approached the direction normal to the shoreline. Finally, after 10^5 steps, its direction became normal to the shoreline of the rounded lake.

The mean sand transport flux after 4×10^4 and 5×10^4 steps in Case 1 can be drawn, as shown in **Figure 16** [13]. Intensive sand transport flux occurred along the shoreline of a cusped foreland at the central part of the water body, enhancing further development of a cusped foreland. Also, intensive sand transport took place near the right corner of the slender water body because of a large aspect ratio of the water body, which induced the formation of a circular lake.

5.2. Segmentation of water body given elliptic distribution of probability (Case 2)

In Case 2, wind blew from the direction of 45° with respect to the principal axis of the slender lake, that is, the probability of occurrence of the wind direction is given by an elliptic distribution [13].

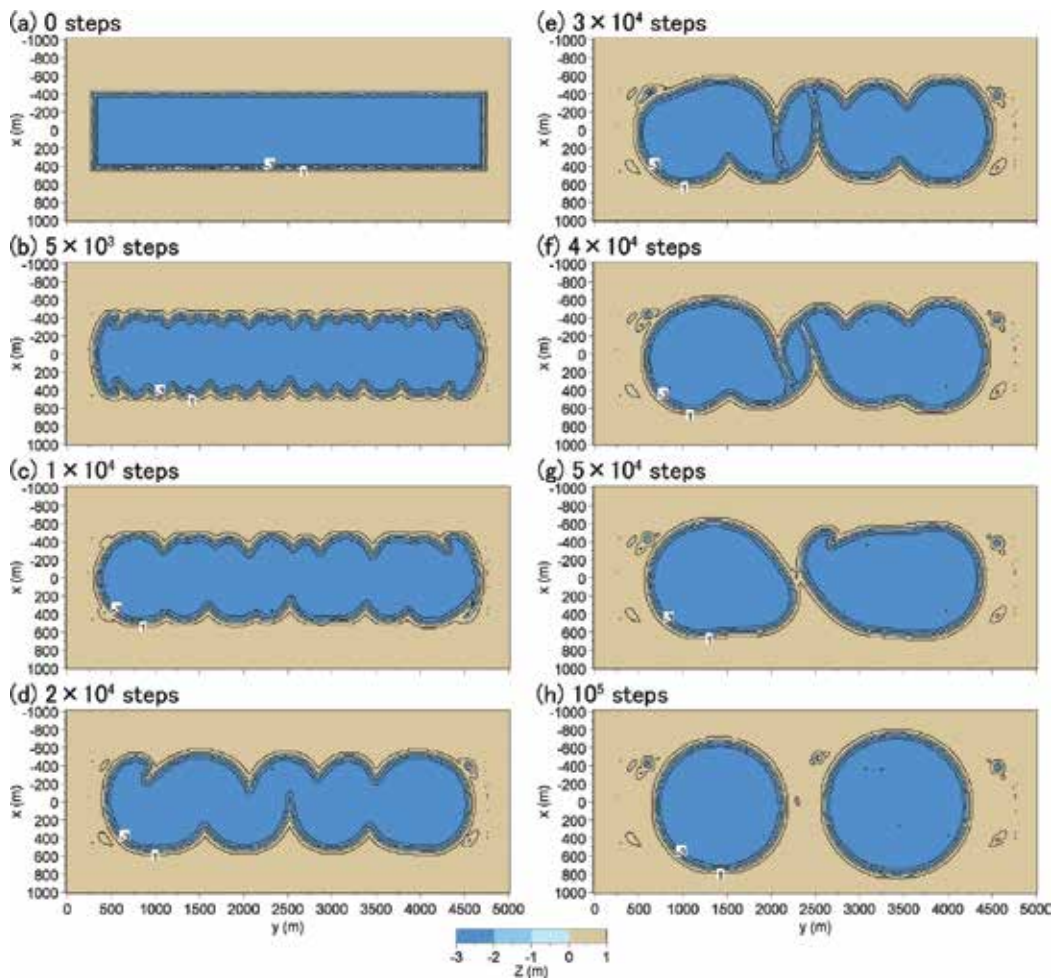


Figure 14. Topographic changes in Case 1 under uniform distribution of occurrence of wind direction and intensity [13].

Uda et al. [8] predicted the formation of oriented lakes [15] using the BG model and showed that oriented lakes can develop when the probability of occurrence of the wind direction is given by an elliptic distribution. Here, the segmentation of a rectangular water body was predicted, assuming that the probability of occurrence was given by an elliptic distribution.

Figure 17 shows the predicted results of the lake averaged over 10^3 steps in Case 2 [13]. Cusped forelands with an asymmetric form had developed on both shores and inclined rightward (leftward) on lower (upper) shorelines in the beginning. Then, the cusped forelands had merged to increase their size and moved rightward (leftward) on lower (upper) shorelines. These results are in good agreement with those obtained by Uda et al. [5] concerning the development of sand spits and cusped forelands owing to the shoreline instability. Because the principal axis of the wind direction is at an angle of 45° relative to the shoreline, and the effect of wind blowing from the land to the lake can be neglected along lower shoreline, the oblique component of waves incident from the left had a higher probability than that of waves incident from the right. As a result, rightward sand transport predominantly

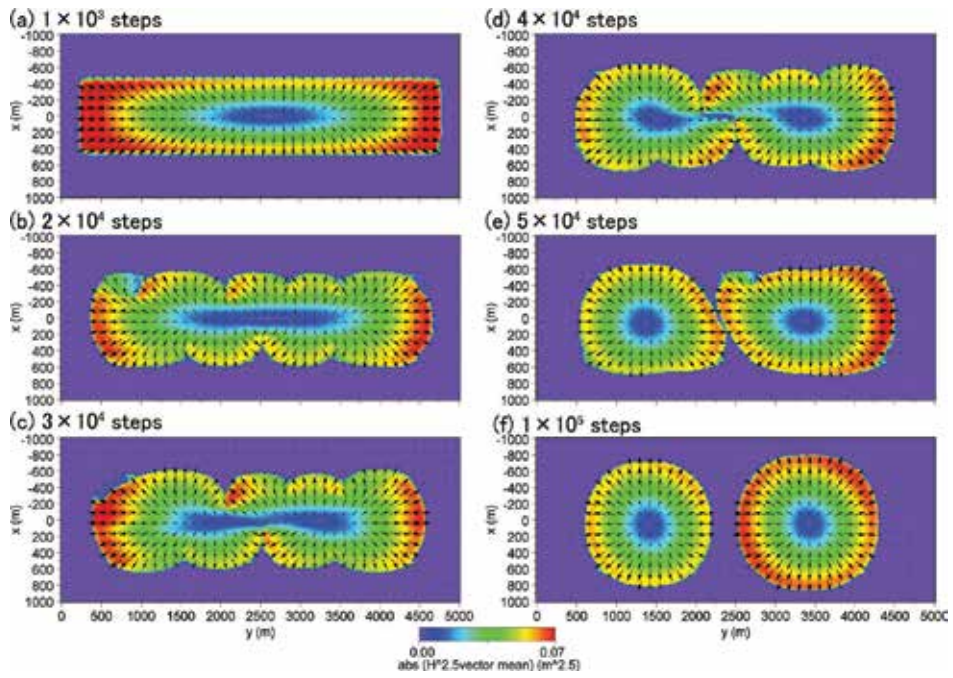


Figure 15. Distribution of mean $(H_{1/2})^{5/2}$ flux in Case 1 [13].

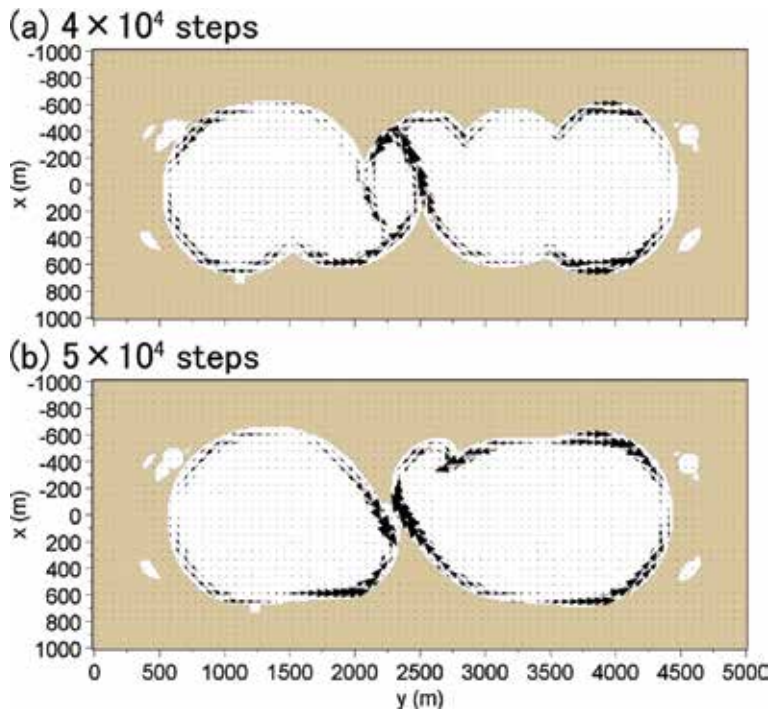


Figure 16. Mean sand transport flux in Case 1 [13].

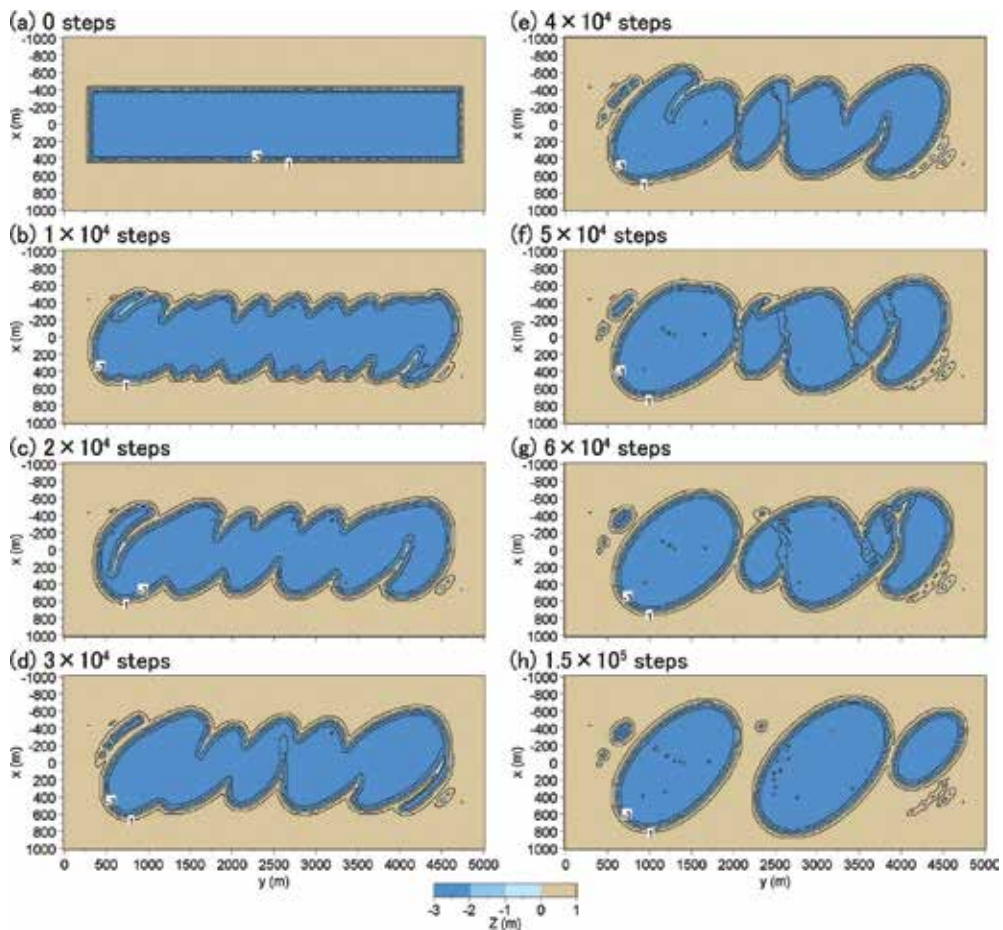


Figure 17. Topographic changes in Case 2 under elliptic distribution of occurrence of wind direction [13].

caused the formation of a cusplate foreland with an asymmetric shape along the y -axis, and rightward movement of the cusplate foreland took place. The formation of a cusplate foreland with an asymmetric shape corresponds to the formation of a lagoon, as shown in **Figure 2**. Furthermore, the cusplate foreland markedly developed at the right (left) end on the lower (upper) shoreline because of the long fetch distance and large wave intensity after 2×10^4 steps. With time, the cusplate forelands near the end of the lake were connected to the ends and formed a barrier island, whereas the cusplate foreland in the central part markedly extended to the opposite shore. After 5×10^4 steps, the water body on the left side was segmented to have an elliptic form. Finally, three segmented lakes with an elliptic shape were formed. The formation of the lakes with an elliptic shape with parallel principal axes explains the development process of the elliptic lakes observed in Chukchi Sea shown in **Figure 1**.

5.3. Segmentation of a triangular or crescent-shaped water body (Cases 3 and 4)

Figure 18 shows the results of the calculation of the segmentation of a triangular water body, assuming that the probability of occurrence of wind direction was given by a circular

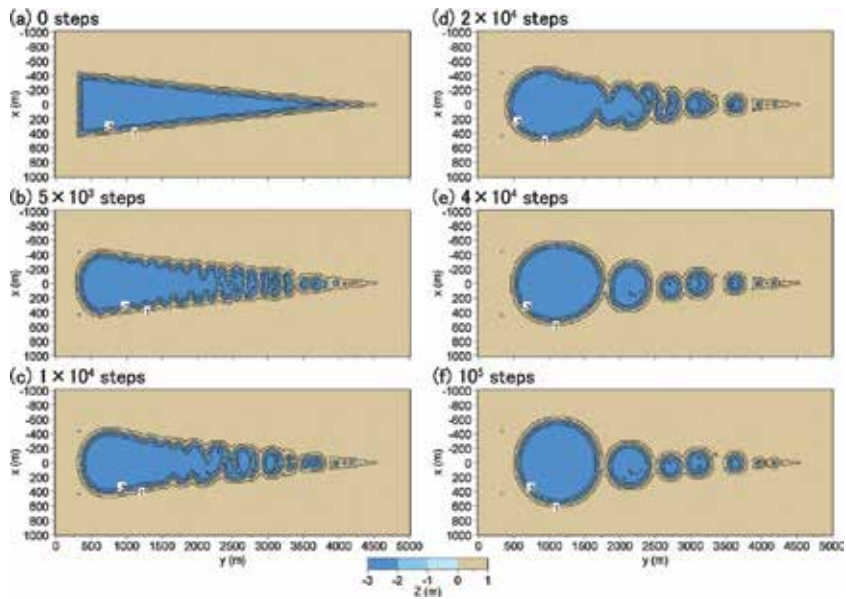


Figure 18. Segmentation of a triangular water body with time.

distribution [7]. Although the results are similar to those in [7], numerical simulation was carried out with changing the size of the lake because of the revision in Eq. (2b). Segmentation rapidly occurred in the vicinity of the right end of the triangular water body, and elliptic lakes were formed in the area between $y = 3.25$ and 3.75 km in the beginning. Near the left end, the segmentation stage was delayed, and cusped forelands extended from both shores. After 1×10^4 steps,

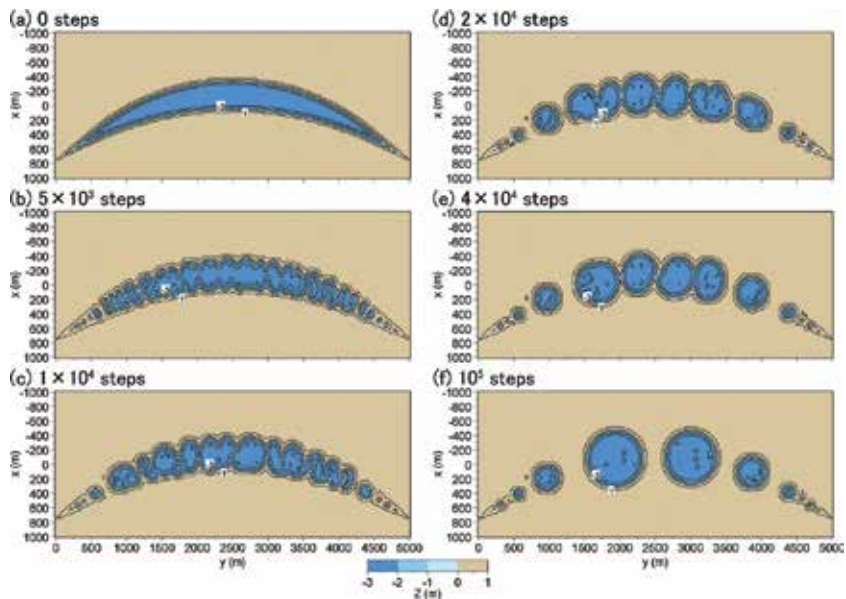


Figure 19. Segmentation of a crescent-shaped water body with time.

the elliptic lake that formed near $y = 3.0$ km became rounded and merged into a larger lake, resulting in a decrease in the aspect ratio. Until 4×10^4 steps, five circular lakes were formed. The shape of the water body after 1×10^4 steps well explains the development of the sand spits in Lake Saroma shown in **Figure 5**.

Similarly, **Figure 19** shows the results of the segmentation of a crescent-shaped water body with time. Rapid segmentation occurred in the vicinity of the both ends of the crescent water body in the beginning. In the area between $y = 3.25$ and 4.0 km, cusped forelands that developed from both shores were alternately distributed on both shores, in contrast to the symmetric cusped forelands in the central part. This explains the features observed in the water body facing the Chukchi Sea, as shown in **Figure 2**. After 1×10^4 steps, sand bars with a hound's-tooth shape were formed in the area between $y = 3.75$ and 4.25 km. The segmentation continued over time, and the lakes became rounded as a whole. After 10^5 steps, circular lakes with a radius corresponding to the initial lake width were formed and stabilized.

5.4. Lakeshore changes in circular lake with a rocky or sandy island

Figure 20 shows the lakeshore changes in Case 5 with a rocky island in a circular lake, assuming that the probability of occurrence of wind direction was given by a circular distribution. Under

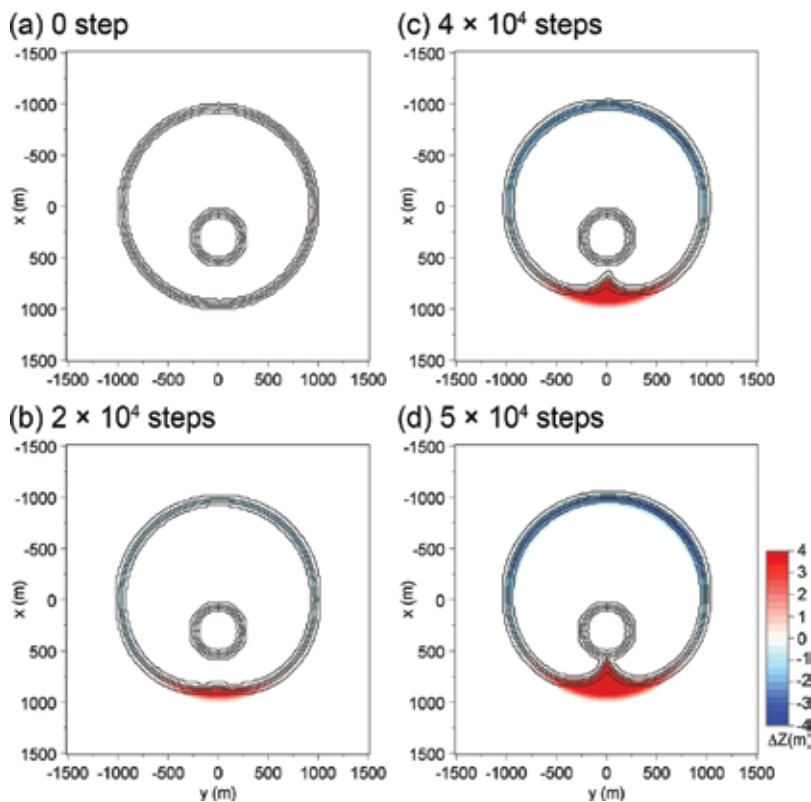


Figure 20. Lakeshore changes behind a rocky island in lake (Case 5).

the condition, a wave-shelter zone was primarily formed on the lee of the island against wind waves incident from x -axis. Sand was transported from the outside of the wave-shelter zone to the inside, and a symmetrical cusped foreland started to form on the lee of the island. After 5×10^4 steps, the cusped foreland connected to the island. Because sand was mainly transported from the opposite shore with a longer fetch distance to the lee of the island, the lakeshore on the opposite shore was eroded. Thus, when a rocky island is asymmetrically located at a location in a lake, the formation of a cusped foreland and erosion on the opposite shore take place at the same time.

Figure 21 shows the same results in Case 6. In this case, the wave-sheltering effect due to the island was strengthened than that in Case 5 because of the proximity of the island to the lakeshore, the cusped foreland rapidly developed together with the formation of a large cusped foreland. After 5×10^4 steps, a headland with a circular head was formed. Because the distance between the island and lakeshore decreased, the wave-sheltering effect increased, resulting in the greater cusped foreland behind the island and erosion on the opposite shore.

The lakeshore changes in Case 7 with a sandy island in a circular lake are shown in **Figure 22**. When waves were incident to the sandy island, the island deformed by the action of waves incident from x -axis, which has the longest fetch distance, and slender sand bars extended

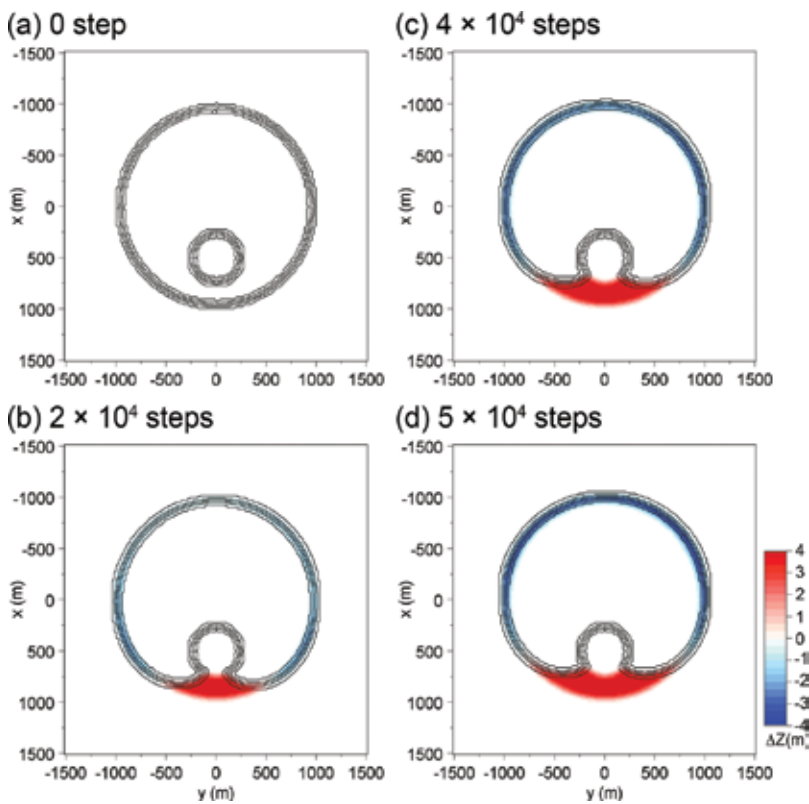


Figure 21. Lakeshore changes behind a rocky island in lake (Case 6).

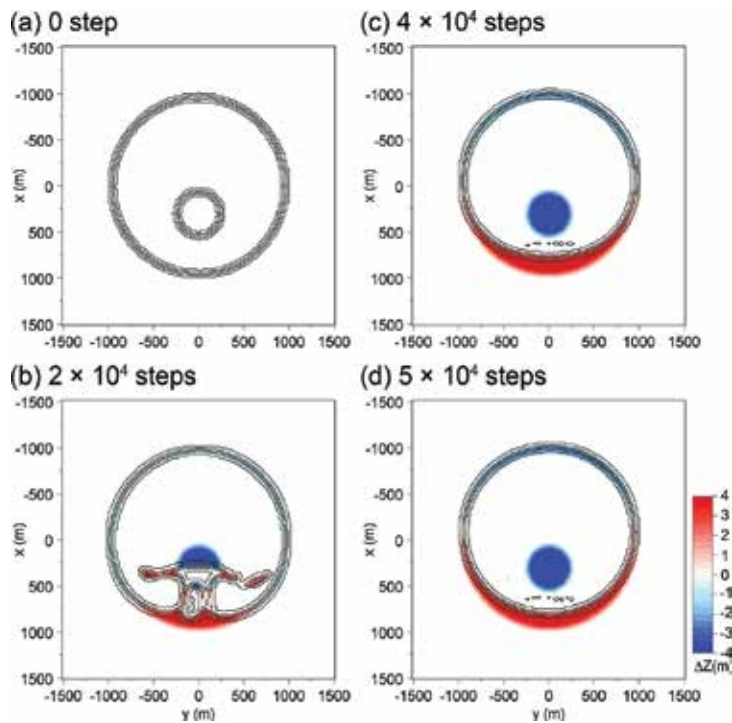


Figure 22. Lakeshore changes around a sandy island in lake (Case 7).

toward the y -axis. In the wave-shelter zone of this sand bars, double tombolo extended at first, which connected to the slender sand bars. With time, all sand comprised of the island were transported to the lakeshore and merged with the lakeshore. After 5×10^4 steps, a large amount of sand was deposited on the lee of the island, whereas the opposite shore was eroded.

Figure 23 shows the same results in Case 8. The initial circular island significantly deformed owing to the action of wind waves incident from the direction of x -axis, and sand bars extending to the direction of the y -axis were formed. Because of the short distance between the island and lakeshore, double tombolo quickly extended on the lee of the sandy island, while leaving a lagoon in the central part. With time, a barrier island was formed with a lagoon inside double tombolo, and the smaller lake behind the barrier island was rounded by wind waves in the closed water body. A large amount of sand was deposited behind the island.

The mean sand transport fluxes averaged over 1000 steps between $1.9 \times 10^4 + 1$ and 2×10^4 steps in Cases 5 and 7 with the same arrangement of an island are shown in **Figure 24**. In Case 5 with a rocky island, the intensive sand transport flux occurred on both sides of the island with decreasing the intensity behind the island, whereas in Case 7, strong sand transport flux toward the tips of the sand bar occurred along the shoreline of sand bars. When setting point O at the center of the circular lake, and points **a** and **b** at both ends of the straight line through point O, as shown in **Figure 24**, the direction of sand transport flux is downward at points **a** and **b**. Out of waves incident to point **a**, waves incident from the upper half of the

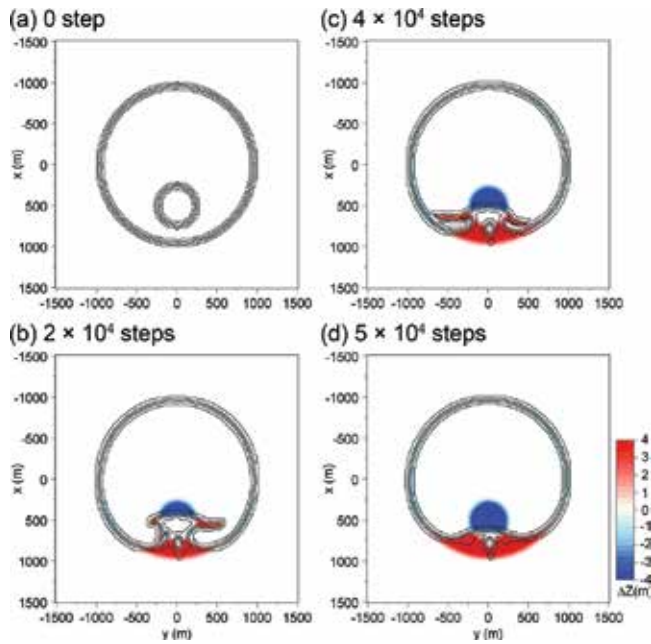


Figure 23. Lakeshore changes around a sandy island in lake (Case 8).

lake causes downward longshore sand transport, and vice versa, when waves are incident from the lower half. Without an island, net sand transport at point A is 0 because of the symmetry of the closed water body. With an island, however, the area of the water body in the lower half decreases than that in the upper half, resulting in weaker wave action. As a result, the direction of the net sand transport fluxes at points a and b became downward, enhancing sand transport from the upper half to the lower half, resulting in erosion in the upper half.

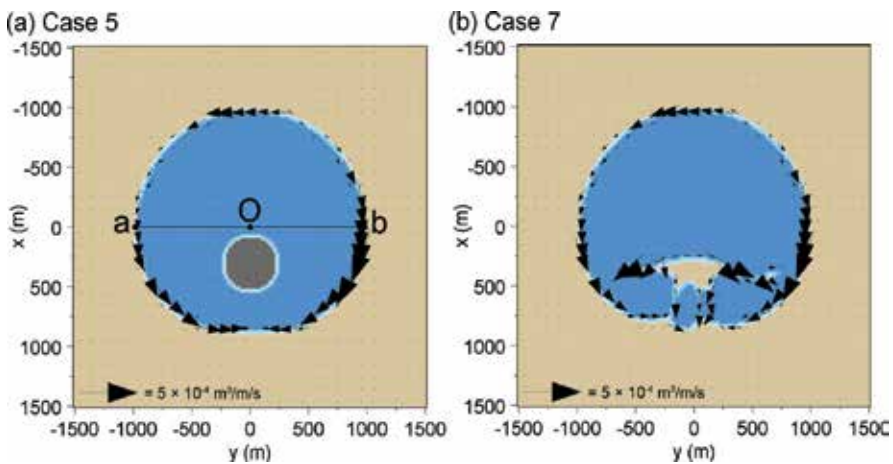


Figure 24. Mean sand transport flux averaged over 1000 steps in Cases 5 and 7.

In the case of Lake Balkhash, part of sand comprised of the island was considered to be transported northwestward, forming a long slender sand bar. Such topographic changes can be explained by the merge of a slender sand bar extended from the island and the sand bar extended in the opposite direction, as shown in the results after 5×10^4 steps in Case 5 and after 2×10^4 steps in Case 7.

6. Conclusions

Specific geomorphological features associated with shoreline instability under a high-wave-angle condition on the lakeshore, such as the development of sand spits, in several elongated water bodies were investigated, and the segmentation of a water body was numerically predicted using the BG model. It was concluded that a rectangular water body segmented into circular (elliptic) lakes when the probability of occurrence of the wind direction was given by a circular (elliptic) distribution. In each case, the wave-sheltering effect of the cusped forelands played a primary role. Also, the merge and segmentation of triangular and crescent-shaped slender water bodies were predicted using the BG model. It was further used for predicting the lakeshore changes when a rocky or sandy island exists in a circular lake. The deformation of a sandy island and merge of the sandy island to the lakeshore were predicted well.

Author details

Takaaki Uda¹, Masumi Serizawa^{2*} and Shiho Miyahara²

*Address all correspondence to: coastseri@nifty.com

1 Head, Shore Protection Research, Public Works Research Center, Taito, Tokyo, Japan

2 Coastal Engineering Laboratory Co., Ltd., Shinjuku, Tokyo, Japan

References

- [1] Ashton A, Murray AB, Arnault O. Formation of coastline features by large-scale instabilities induced by high-angle waves. *Nature*. 2001;**414**:296-300
- [2] Ashton A, Murray AB High-angle wave instability and emergent shoreline shapes: 1. Modeling of sand waves, flying spits, and capes. *Journal of Geophysical Research*. 2006;**111**:F04011. DOI: 10.1029/2005JF000422
- [3] Zenkovich VP. *Processes of Coastal Development*. New York: Interscience Publishers; 1967. p. 751
- [4] Ashton A, Murray AB, Littlewood R, Lewis DA, Hong P. Fetch limited self-organization of elongate water bodies. *Geology*. 2009;**37**:187-190

- [5] Uda T, Serizawa M, Miyahara S. Numerical simulation of three-dimensional segmentation of elongated water body using BG model. Proc. 33rd ICCE, sediment. 65, 2012. pp. 1-11
- [6] Serizawa M, Uda T, San-nami T, Furuike K. Three-dimensional model for predicting beach changes based on Bagnold's concept. Proc. 30th ICCE, 2006; pp. 3155-3167
- [7] Uda T, Serizawa M, Miyahara S, San-nami T. Prediction of segmentation and mergence of shallow water bodies by wind waves using BG model. Proc. Coastal Dynamics. 2013; Paper No. 166, pp. 1729-1740
- [8] Uda T, Serizawa M, San-nami T, Miyahara S. Prediction of formation of oriented lakes. Proc. 34th ICCE, ASCE. 2014. pp. 1-12
- [9] Scheffers AM, Kelletat DH. Lakes of the World with Google Earth: Understanding our Environment. Coastal Research Library, Vol. 16. Switzerland: Springer International Publishing; 2016. p. 293
- [10] Miyahara S, Uda T, Serizawa M, San-nami T. Prediction of effects of artificial alteration on segmentation of a slender water body. Coastal Sediments '15. 2015;**164**:1-14
- [11] Wilson BW. Numerical prediction of ocean waves in the North Atlantic for December, 1959. Deut. Hydrogr. Zeit, Jahrgang 18, Heft 3. 1965. pp. 114-130
- [12] Goda Y. Revisiting Wilson's formulas for simplified wind-wave prediction, Journal of Waterway. Port, Coastal and Ocean Engineering. 2003;**129**(2):93-95
- [13] Serizawa M, Uda T, Miyahara S. Segmentation of water body given probability of occurrence of wind direction by circular or elliptic distribution. Proc. 35th Conf. Coastal Eng., sediment. 6. 2016. pp. 1-15
- [14] San-nami T, Uda T, Gibo M, Ishikawa T, Miyahara S, Serizawa M. Change in carbonate beach triggered by construction of a bridge on Irabu Island and its simulation using BG model. Asian and Pacific Coasts 2013, Proc. 7th International Conf. 2013. pp. 24-31
- [15] Seppälä M. Wind as a Geomorphic Agent in Cold Climates. New York: Cambridge University Press; 2004. p. 358

Assessing the Hydrodynamic Pattern in Different Lakes of Malaysia

Zati Sharip, Shahirwan Aman Shah,
Aminuddin Jamin and Juhaimi Jusoh

Additional information is available at the end of the chapter

<http://dx.doi.org/10.5772/intechopen.73274>

Abstract

Hydrodynamic simulations using three-dimensional numerical model were carried out in three different shallow tropical lakes to understand the characteristics of water movement in the respective water bodies. The models were based on meteorological data from the nearest stations and calibrated with current measurement, temperature, or water-level data. The results show good agreement between measured and simulated velocities and/or temperature at certain depth. This study found that the major driving forces of the hydrodynamic pattern were different in the three lakes. Hydrodynamic simulations showed that Bukit Merah and Durian Tunggal reservoirs were more sensitive to wind-driven motion. Floodplain lakes, such as Bera Lake, are more sensitive to flood inflow by the main river during the monsoon season. Convective motion driven by water temperature gradient was important for Bukit Merah and Bera Lake.

Keywords: circulation, convective motion, hydrodynamic simulation, numerical modeling, wind-driven motion

1. Introduction

Hydrodynamic studies in water bodies are important areas of study for researchers and managers to understand patterns of surface water movement and pollutant transport. Variations in hydrodynamics among lakes have been associated with differences in morphological geometries and the surrounding topographies as well as hydrometeorological and geochemical influences [1]. Simulations of hydrodynamic pattern using high-dimensional numerical models have become useful for understanding the complex role of different forcing mechanisms. For example, wind-driven motion was an important forcing mechanism to induce

observed basin-scale cyclonic gyre in Lake Maracaibo [2]. Bailey and Hamilton showed that the effects of changing wind direction were found to have a greater influence on the sediment concentration distribution compared to advection and diffusion in lakes having directionally varying strong winds such as Thomsons Lake in Australia [3]. Numerous earlier works have established the spatial variability of winds and temperature on lake dynamics including horizontal and vertical mixing and stratification pattern [4].

Many recent studies have also used hydrodynamic simulation to assess the impacts of climate change on lakes [4, 5]. One-dimensional hydrodynamic model was used to identify potential drawbacks of climate change in Lake Ammersee, Germany. The study found that global warming of the atmosphere increased water temperatures, subsequently extending duration of stratification and increasing thermal stability on the lake ecosystem [6]. In [7], simulation results indicated global warming led to possible increase in water transparency in Lake Mangueira, Brazil due to nutrient limitation and submerged macrophyte growths, while increase in inflows and low water levels changed the lake hydrodynamic behavior leading to algal bloom [8].

Despite known significant advances in lake hydrodynamic information published in literature, understanding on the circulation patterns in different lakes, in particular in the trophic zone, remains inadequate due to the absence of long-term monitoring data and technical knowledge on numerical model simulation [4]. The aim of this study is to improve understanding of the hydrodynamic characteristics in different tropical lakes located in Malaysia. Understanding such hydrodynamic pattern is necessary to enable effective management purposes.

2. Research method

The study has focused on three shallow water bodies namely Bukit Merah reservoir, Durian Tunggal reservoir and Bera Lake (**Figure 1**). Bera Lake is a natural floodplain lake with a mean depth of about 2.8 m, while Durian Tunggal is a water supply reservoir with a mean depth about 6 m. Bera Lake (N3°7'00", E102°36'00") is a dendritic, alluvial peat and freshwater swamp system situated in Bera District, Pahang [9], while Durian Tunggal Lake is located in the Malacca State, Malaysia (N2°20'00", E102°18'00"). Bukit Merah reservoir is a multi-function shallow reservoir (mean depth of about 2.5 m) created for irrigation and flood mitigation. The reservoir is located in Northern Perak State at N5°2'00", E100°40'00". Durian Tunggal reservoir is small (surface area about 5.8 km²), while Bukit Merah reservoir is large (surface area of about 33 km²). Both Bera Lake and Durian Tunggal Lake are mesotrophic, while Bukit Merah Lake is mesotrophic-eutrophic [10].

Meteorological and hydrological data were obtained from automatic weather monitoring stations deployed at each lake or the nearest weather or rainfall stations over the study period. Meteorological data, such as wind, water discharge, and morphological properties, were important elements for three-dimensional hydrodynamic model application and calibration of the model. Bathymetry data for Bukit Merah Reservoir were attained from hydrographic survey results provided by Kerian Drainage and Irrigation Department. Hydrographic surveys were carried out for Bera Lake and Durian Tunggal reservoir. Survey area for Bera Lake

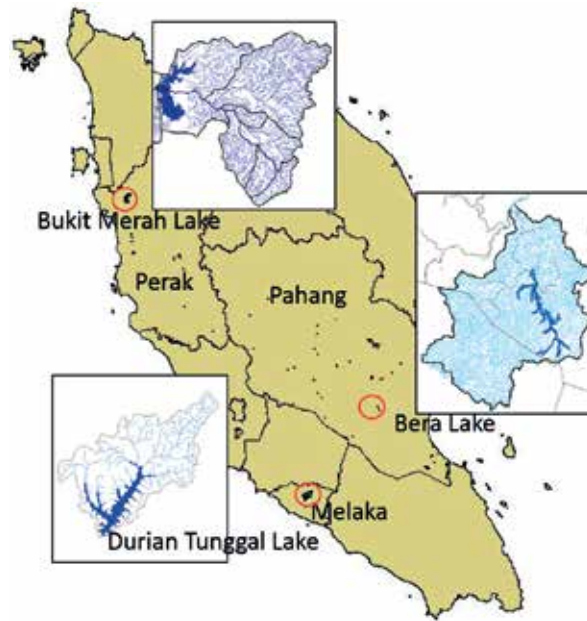


Figure 1. Map of study lakes in Peninsular Malaysia.

Lake	Bera	Durian Tunggal	Bukit Merah
Horizontal grid designs	100 m uniform mesh model	100 m uniform mesh model	200 m × 200 m; 5 m mesh for channel
Vertical grid (m)	1.0	1.0	0.5
Simulation period	March-June 2015	January-March 2014	February-August 2014
Computational area (m)	3180 × 3500	4300 × 5200	6500 × 9500
Maximum time step (s)	3	2	10
Surface drag coefficient	$0.0007 + 0.0004\sqrt{\text{Wind speed(m/s)}}$		
Vertical eddy viscosity and diffusivity	Predicted by the turbulence closure model		

Table 1. Hydrodynamic model set up and computational setting.

was limited to open lake areas due to extensive presence of macrophytes. The bathymetry and shoreline data were meshed into three-dimensional grids (**Table 1**). Smaller vertical grid (0.5 m) was selected for the Bukit Merah reservoir due to its shallowness (~4 m) while vertical grid of 1 m was chosen for Bera and Durian Tunggal lakes. Bukit Merah Lake has nonuniform mesh type with larger grid for open water and smaller grid in channel connecting the north and south of the lake. For Durian Tunggal Lake, focus was given to the larger part of the lake in the east with areas separated by road excluded in the analysis due to the lack of observation data. The bathymetry of the three lakes is shown in **Figure 2**. Flow data at nearest station within each lake catchment were obtained from the Drainage and Irrigation Department of

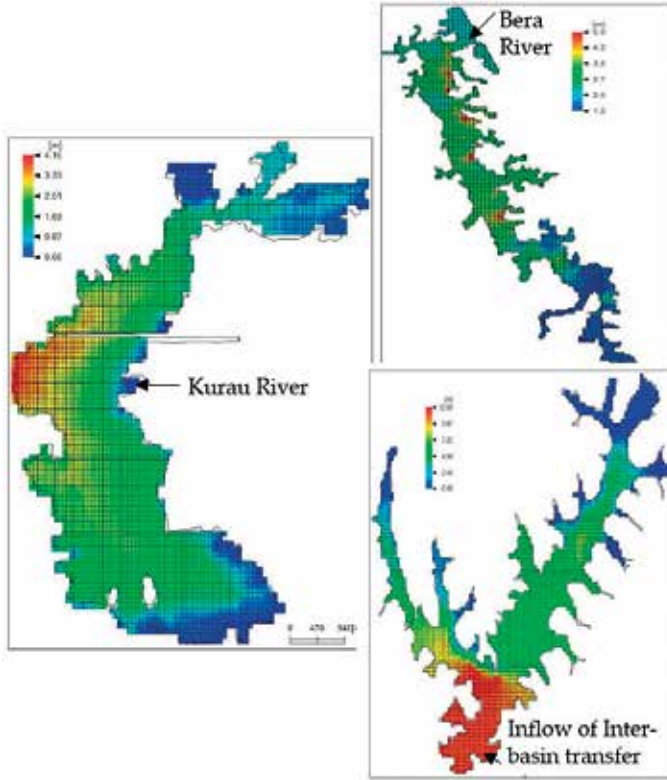


Figure 2. Bathymetry of study lakes and their major inflow.

Malaysia or published information in [11, 12]. Additional measurements of main river discharges were also carried out in Bukit Merah and Bera lakes. Current data were based on current measurements using Acoustic Doppler Current Profiler (ADCP).

This study used a three-dimensional rectilinear grid hydrodynamic model to simulate the hydrodynamic structures of the lakes. The numerical model comprises integrated momentum, continuity, and heat transfer equations together with the equation of state developed by National Institutes of Japan [9]. The physical processes are described by fluid motion (Eq. (1)), flow continuity (Eq. (2)), state equation (Eq. 3), and heat transfer conservation (Eq. (4)), and the numerical schemes are adapted in-line with the methodology described in [13, 14].

For each layer k , the depth integrated momentum equation is described as follows:

$$\begin{aligned}
 \frac{\partial \mathbf{M}_k}{\partial t} + (\mathbf{v} \cdot \nabla) \mathbf{M}_k + (\mathbf{v}w)|_{-H_{k-1}} - (\mathbf{v}w)|_{-H_k} - f_0 \mathbf{k} \times \mathbf{M}_k \\
 = \frac{h_k}{\rho_k} \left(\Psi_k - \frac{1}{2} g h_k \nabla \rho_k \right) + [\nabla \cdot (A_H \nabla)] \mathbf{M}_k \\
 + \left(A_z \frac{\partial \mathbf{v}}{\partial z} \right) \Big|_{-H_{k-1}} - \left(A_z \frac{\partial \mathbf{v}}{\partial z} \right) \Big|_{-H_k}
 \end{aligned} \tag{1}$$

$$\frac{\partial \zeta}{\partial t} = w - \nabla \cdot \mathbf{M}_1, w_{k-1} = w_k - \nabla \cdot \mathbf{M}_k \quad (2 \leq k \leq K-1), \quad (2)$$

$$\rho = \rho(S, T) \quad (3)$$

$$\begin{aligned} & \frac{\partial}{\partial t} (h_k \cdot \theta_k) + \nabla \cdot (\mathbf{M}_k \cdot \theta_k) + (w\theta)|_{-H_{k-1}} - (w\theta)|_{-H_k} \\ & = [\nabla \cdot (h_k K_H \nabla)] \cdot \theta_k + \left(K_z \frac{\partial \theta}{\partial z} \right) \Big|_{-H_{k-1}} - \left(K_z \frac{\partial \theta}{\partial z} \right) \Big|_{-H_k} \end{aligned} \quad (4)$$

In these equations, h_k ($k = 1, 2, \dots, K$) represents thickness (cm) of each k layer, H the still-water depth (cm), $v = (u, v)$ the horizontal velocity components ($\text{cm}\cdot\text{s}^{-1}$) in the x, y direction, w the vertical velocity ($\text{cm}\cdot\text{s}^{-1}$), ρ the seawater density ($\text{g}\cdot\text{cm}^{-3}$), ζ the sea-surface level (cm), f_0 the Coriolis parameter (s^{-1}) which is described as $f_0 = 2\omega \sin \varphi_0$ with the angular velocity ω (s^{-1}) of the earth rotation and the mean latitude φ_0 of the lake, g the gravitational acceleration ($= 980 \text{ cm}\cdot\text{s}^{-2}$), and P_a the atmospheric pressure ($\text{g}\cdot\text{cm}^{-2}\cdot\text{s}^{-1}$). $\mathbf{M}_k = h_k \cdot \mathbf{v}_k$ is volume transport integrated into vertically in each layer, ∇ the horizontal gradient operator, A_H and K_H the horizontal viscosity and diffusivity coefficients ($\text{cm}^{-2}\cdot\text{s}^{-1}$), A_Z and K_Z are vertical viscosity and diffusivity coefficients ($\text{cm}^{-2}\cdot\text{s}^{-1}$), and θ is the conservative physical value such as temperature. T and S represent water temperature ($^{\circ}\text{C}$) and salinity (ppt), respectively.

The model employs the turbulence closure scheme, the k - L model, that considers turbulence kinetic energy (k) and mixing length (L) for hydrodynamic simulation due to the importance of vertical turbulence transport processes. The buoyancy effect due to stratification was based on Munk-Anderson empirical relationship [13]. Knudsen's expression was adopted for calculating the water density from water temperature and salinity. The heat exchange calculation through the water surface is estimated based on the contribution from the sensible heat flux, and latent heat flux, short wave radiation and long wave radiation. Meteorological data, such as air temperature, wind speed, and solar radiation, provide the input for the surface heat balance.

The main inputs of the model were the river inflow; meteorological parameter, such as wind, rainfall, and air temperature; and bathymetry data. Comparison between different wind speeds and under calm wind conditions was made to evaluate the circulation pattern and transport phenomena. The model assumes no physical effect of the flow field and no contribution from the groundwater. Despite the fact that a large quantity of macrophytes, such as submerged species *Cabomba furcata* in Bukit Merah Lake and emergent plants *Pandanus helicopus* in Bera Lake, may shape the hydrodynamic features, this effect was not considered in the study. The bathymetry data for Bera Lake only cover open surface areas where accessibility is not limited, while the presence of submerged species in Bukit Merah was highly variable during the study period. The maximal allowable time step for the models follows the Courant-Friedrichs-Lewy (CFL) condition stability criterion with values completed at 3, 10, and 2 s for Bera, Bukit Merah, and Durian Tunggal, respectively. In this respect, we discuss the impact of drought and water management on the hydrodynamic pattern of the water bodies. The main characteristics of runs are explained in **Table 1**.

3. Results and discussion

3.1. Hydrological and meteorological characteristics

Wind speed and rainfall pattern vary between the three lakes (**Figure 3**). Rainfall amount and wind speed in 2016 was highest in Durian Tunggal Lake compared to Bera and Bukit Merah lakes. Highest daily rainfall amount recorded was 151, 50, and 33 mm in Durian Tunggal, Bukit Merah, and Bera lakes, respectively. Wind speed was also highest in Durian Tunggal Lake followed by Bukit Merah and Bera lakes. Mean daily wind speeds were relatively higher

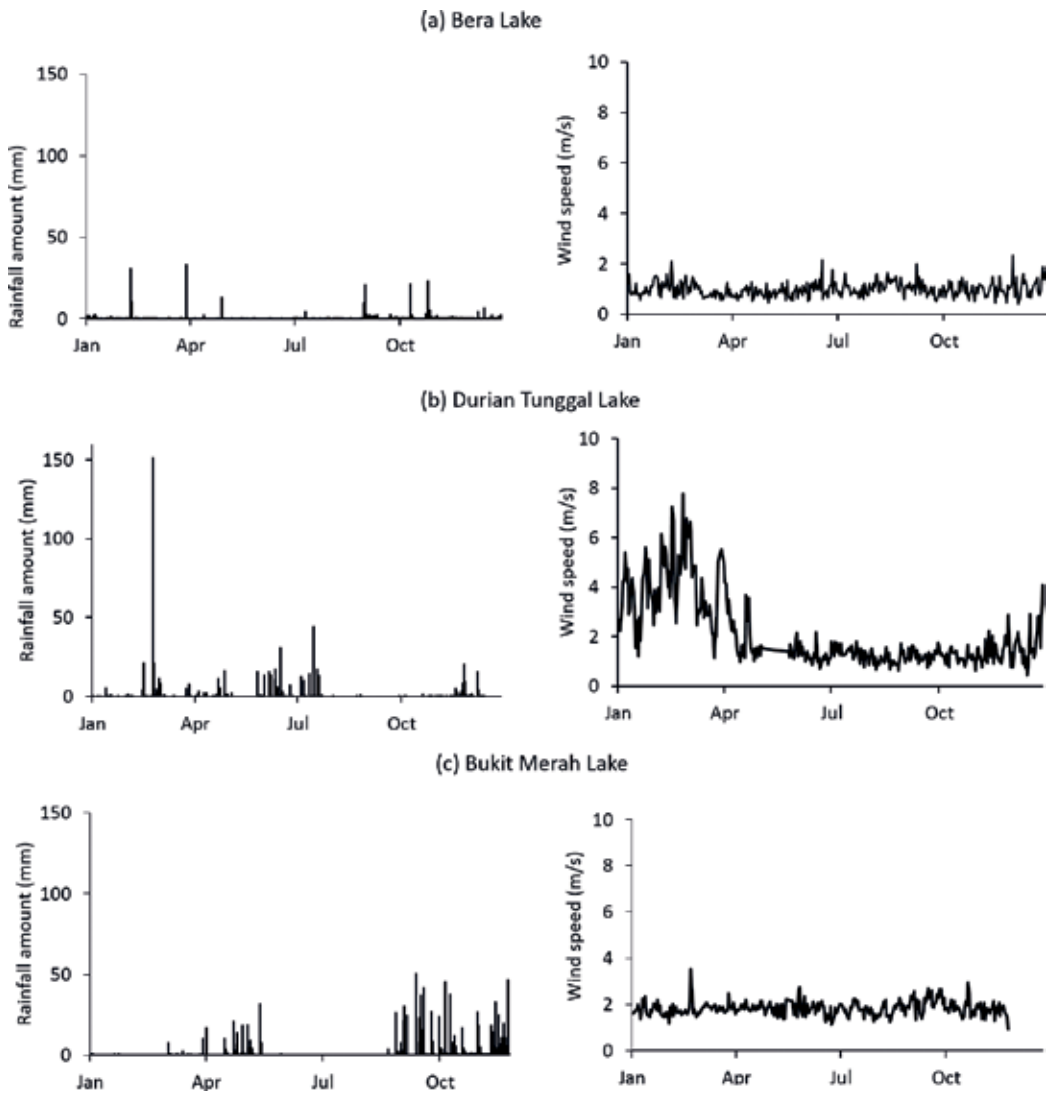


Figure 3. Rainfall amount and wind speed in three lakes in 2016.

in Durian Tunggal and Bukit Merah, namely 2.1 and 1.8 m/s compared to Bera Lake of 1.0 m/s. The highest daily mean wind speeds recorded in Durian Tunggal, Bukit Merah, and Bera Lake were 7.8, 7.7, and 2.6 m/s, respectively.

The main rivers that flow into the Bukit Merah Lake are Kurau River and Merah River. Kurau River covers a large catchment with total surface area of 337 km² and thus contributing bigger flow into the lake. Mean flow recorded at DID Pondok Tanjung monitoring station for the period 1960–2004 was 16.5 m³/s. Measurement recorded in 2012 showed flows of 26.7 and 1.3 m³/s for Kurau River and Merah River, respectively [15]. The discharge of Kurau River based on measurement was approximately 13 m³/s. The main river that flows into Bera Lake is the Tembagau River and Bera River, which channel backflow of water from Pahang River during monsoon season. Inflows from Bera River range between <1 and 12.2 m³/s, while inflows from tributaries are almost negligible for Durian Tunggal Lake. Durian Tunggal lake is more dependent on the inter-water transfer scheme from Muar River [16] consistent with qualitative observation. Generally, the small catchment and large conversion of forested land to agriculture in Durian Tunggal Basin are likely reducing the natural water resource supply within the catchment. In contrast, Bera Lake and Bukit Merah have large forest reserve and water catchment storage subsequently more inflows.

3.2. Model calibration

In this chapter, evaluation of the model performance was based on the visual inspection of observed and simulated trends and correlation coefficients of determination (r^2). Flow field of east, north, and vertical directions was measured at one location in Bukit Merah using ADCP and used to calibrate the hydrodynamic model. The results show good agreement between measured and simulated velocities at 1-m depth (**Figure 4a**). However, proper agreement of velocities at different depths and water level was difficult to achieve due to many uncertainties connected with hydrology and water demand management. Additionally, temperature sensor was also deployed to calibrate the hydrodynamic model. Simulated temperature yields very good agreement with measured temperature (**Figure 4b**). Based on the coefficients of determination (r^2) between model output and observed data, the simulated current has higher correlation with the observed values at 1 m level. The coefficient of determination for temperature was 0.742. In Durian Tunggal and Bera Lake, temperature-depth profiling was carried out at few sites for calibration purposes. The coefficient of determination for temperature was 0.762 and 0.6 for Durian Tunggal and Bera Lake, respectively.

3.3. Model analysis

Hydrodynamic simulation in Bukit Merah Lake indicated that the major driving force of the hydrodynamic pattern in the reservoir is wind-driven motion. The hydrodynamic patterns at surface level as shown in **Figure 5** were averaged from air-water interface to 0.5 m depth. The circulation pattern analyzed and modeled showed mixing and water movement in the lake, which is closely related to wind velocity and direction. For example, a northeast wind, with magnitude approximately greater than 3 m/s, can cause a substantial transport and circulation of water mass in Bukit Merah Lake. A much higher wind speed exceeding 7 m/s was recorded

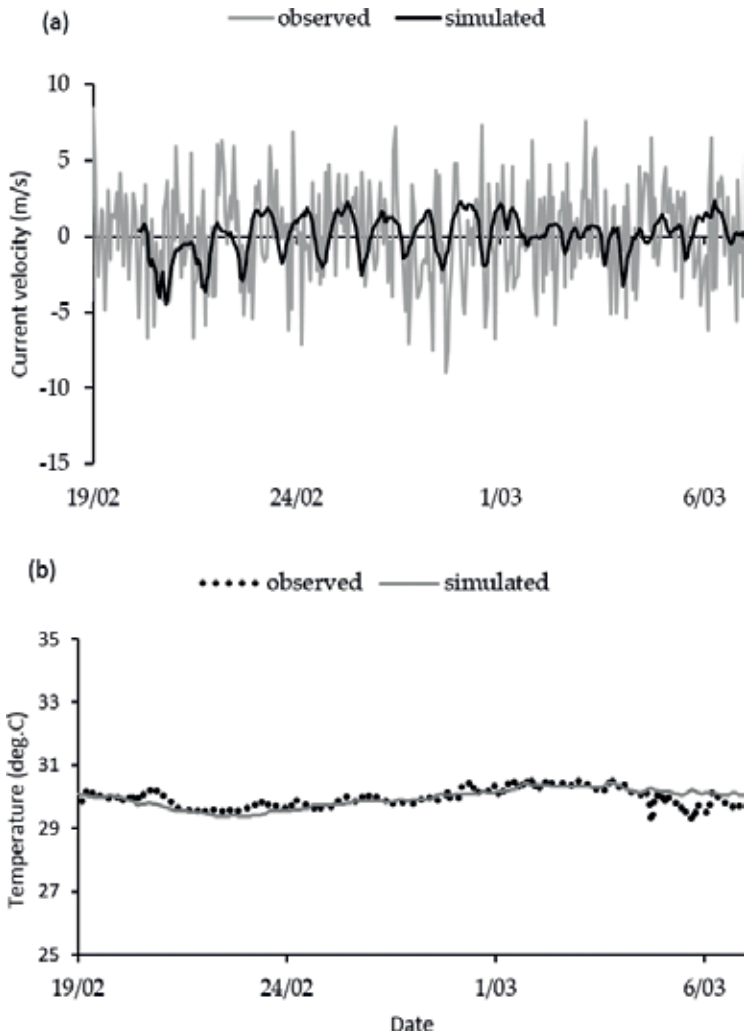


Figure 4. Calibrated results of (a) current velocity and (b) temperature in Bukit Merah Lake.

in an earlier observation in 2014, and most wind direction was observed to be from north-east [17]. Wind-induced storm has been observed to have transported floating vegetation island from north to south of the lake [17]. In our simulation, water movement responded along the wind direction. As shown in **Figure 5a**, north-east wind moved water toward southeast direction. High wind exceeding 7.5 m/s induced mean surface current about 7.2 cm/s. Higher current of 14.4 cm/s occurs near constricted channel. Warmer temperature was observed in the west, while lowest temperature was observed in the southeast. High wind effects homogenized the surface temperature and induced turbulence that could well mix the water column (**Figure 5a** and **b**).

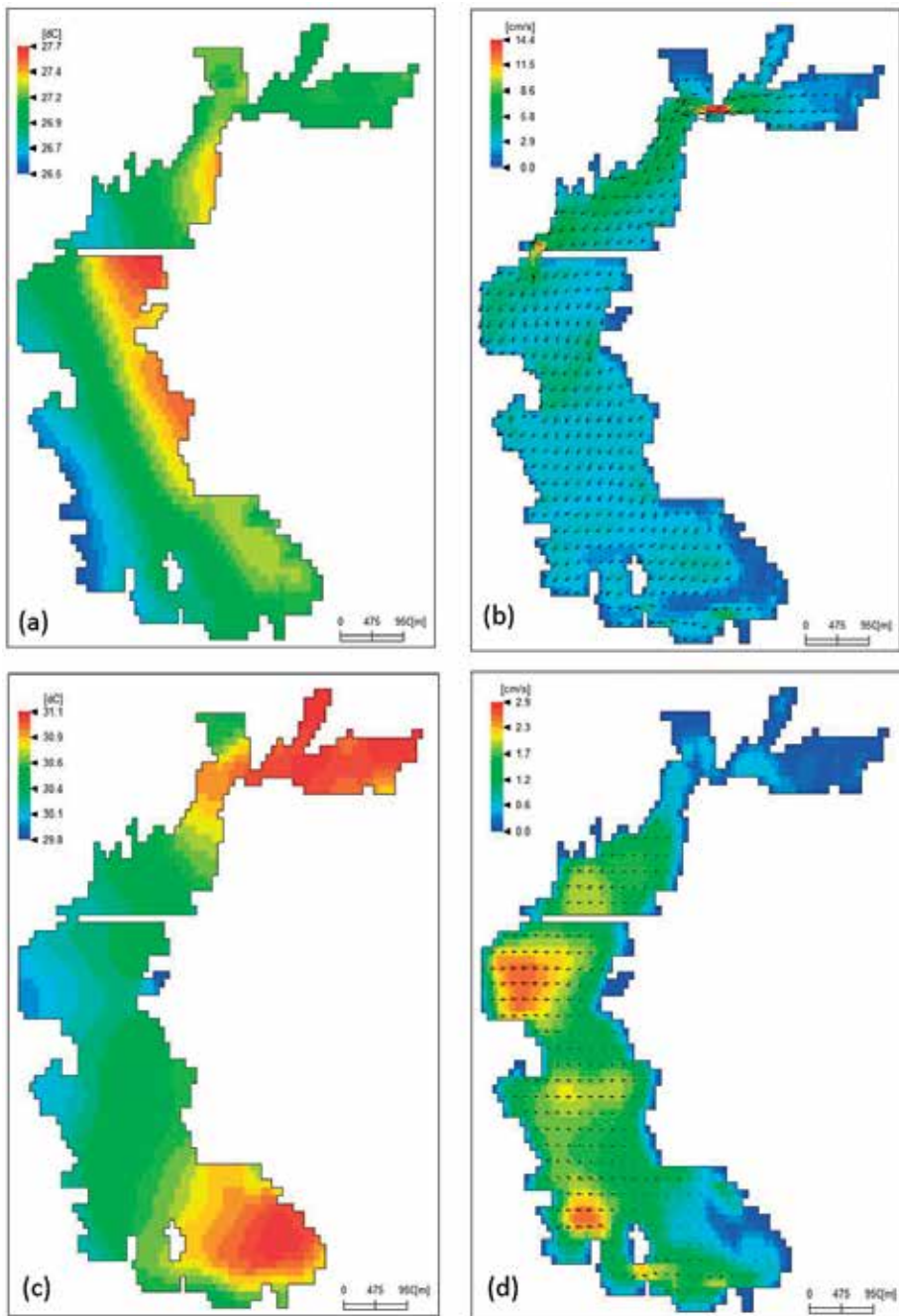


Figure 5. Pattern of (a) temperature and (b) current velocity pattern under high wind events and (c) temperature and (d) current velocity pattern under low wind events in Bukit Merah Lake.

In addition to winds, inflows from tributaries are also important for Bukit Merah Lake. Water movement from Kurau River from simulated result responded directly with the inflow of Kurau River. The water mass moved from the river mouth in the east to the deeper area in the west and south. Wind effects conveyed further the water mass and spread in to larger areas depending on the speed and direction. Under low wind events or calm conditions, temperature gradient between shallow and deep areas promoted convective motion. Convective motions can be driven by differential heating and cooling of water mass of differed depth and volume. Since the lake depth was less than 5 m deep, both wind-induced and nocturnal mixing in Bukit Merah Lake extended to the lake bottom consistent with mixing pattern in other shallow lakes [18]. Well-mixed lakes were like to be more supersaturated with oxygen and thus more productive due to better light environment and nutrient supply such as from sediment. This hydrodynamic feature may support the findings on phytoplankton characterization between the three lakes, which indicated higher productivity in Bukit Merah Lake compared to the two lakes [19].

Unequal heating of surface layer between shallow and deep regions resulted in higher rate of change in temperature in the shallow areas due to small volume of water contained. This differential heating can induce movement of warm waters over the cooler waters [20]. Similarly, differential cooling or unequal cooling between shallow and deep regions resulting from larger heat loss in the shallow regions or weaker winds due to wind shelters resulted in downslope movement of cold waters to deeper regions [20]. Most of the areas at the south and west of Bukit Merah are shallower compared to the east side of Bukit Merah which induced movement of water toward the deeper areas in the east or center due to differential heating in the shallow areas during calm conditions (**Figure 5c** and **d**). In contrast to current velocity during wind events, current velocity during calm weather were small, in the range of nil to 2.9 cm/s. Differential cooling was observed in other large lake, such as the Lake Tanganyika in Africa, which induced large-scale convective motion throughout the lake [21]. Drought associated with long dry season may have strong impact on the Bukit Merah Lake due to its large size. Continuous abstraction of water for irrigation and higher evaporation rates can lead to significant drop of water level in the lake. Low water level reduces the lake volume and affects the hydrodynamic patterns with stronger mixing and temperature gradient in agreement with atmospheric forcing including wind, temperature, and solar radiation pattern.

Hydrodynamic simulation in Bera Lake indicated that the major driving force of the hydrodynamic pattern in the reservoir is river inflow. Bera Lake is mostly surrounded by riparian forest and subsequently is sheltered from wind motions. Wind records showed low wind conditions with average winds of about 1 m/s. Wind-driven motion has low effects on this natural lake. However, higher wind speed (>3 m/s) occasionally alters water movement in the lake (**Figure 6a**). Similar to the nearby Chini Lake, this floodplain lake is very much influenced by inflows of the main river, namely the Pahang River that backflows into the lake through Bera River during monsoon and rainy seasons. Simulation showed the water movement responded directly with inflow from the Pahang River (**Figure 6b**). The inflow of cold and turbid water from the Pahang River is heavier and enters into the lake as underflows. Our qualitative observation revealed that inflows into the lake from all tributaries were negligible during dry period and drought, and together with no rain input led to severe drop of lake's water level.

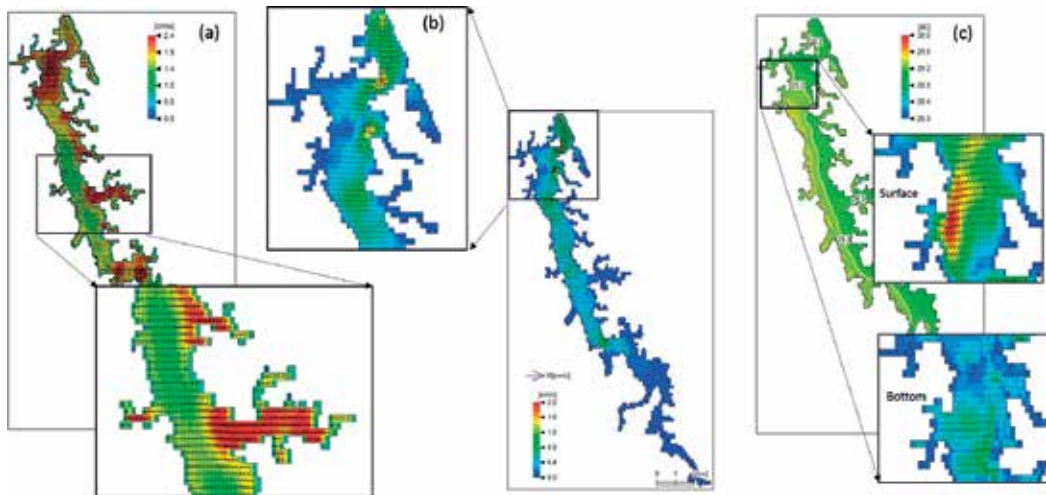


Figure 6. Temperature and current velocity pattern in Bera Lake during (a) high winds, (b) strong inflow from Bera River, and (c) calm wind and low flow.

The turbid water from the Pahang River may also induce vertical density gradient as surface temperature increases at the surface water due to reduction in penetration of solar radiation to a smaller depth as observed in the nearby floodplain Chini Lake [19]. Convective motion driven by water temperature gradient was also important in Bera Lake. In this lake, under still wind conditions and low flow, movement of current or convective motion was detected by the simulation which was likely driven by unequal temperature gradient between the macrophytes (shallow) and open water (deeper). During the night, warmer temperature at the deeper area in the east moved to shallower area in the west at the surface, while cooler water in the shallow areas move to the deeper areas of the open water at the lake bottom (**Figure 6c**). Density-driven flow was observed between reed beds and open water in a shallow lake in southern Sweden [22] and in laboratory experiments [23]. Current velocities induced by differential cooling and heating between floating-leaved bed and open water reported in the literature were between 1.6 and 1.9 cm/s [19]. Higher horizontal density flow was reported between open water and reed beds (1.5–2.8 cm/s) [22] and between the wetland and lake (3–5 cm/s) [24]. In this study, simulated current movements under no winds as illustrated in the simulation were in the range of 1.0–3.0 cm/s.

Hydrodynamic simulation in Durian Tunggal Lake showed the importance of wind effects in driving the hydrodynamic pattern in the reservoir. Wind records showed high wind conditions exceeding 6 m/s with wind direction mostly from the northeast. Durian Tunggal Lake was deeper compared to the other two lakes and may experience more apparent stratification. Lake isotherm under different wind conditions is shown in **Figure 7**. High wind speeds exceeding 6 m/s led to strong mixed layer throughout the water column within the upper (**Figure 7a**). In mid-afternoon and high solar radiation, increased surface heating and weak winds induce differential heating near surface layer (**Figure 7b**). The lake may also experience differential heating due to variation in heat absorption, given the high turbidity level in the

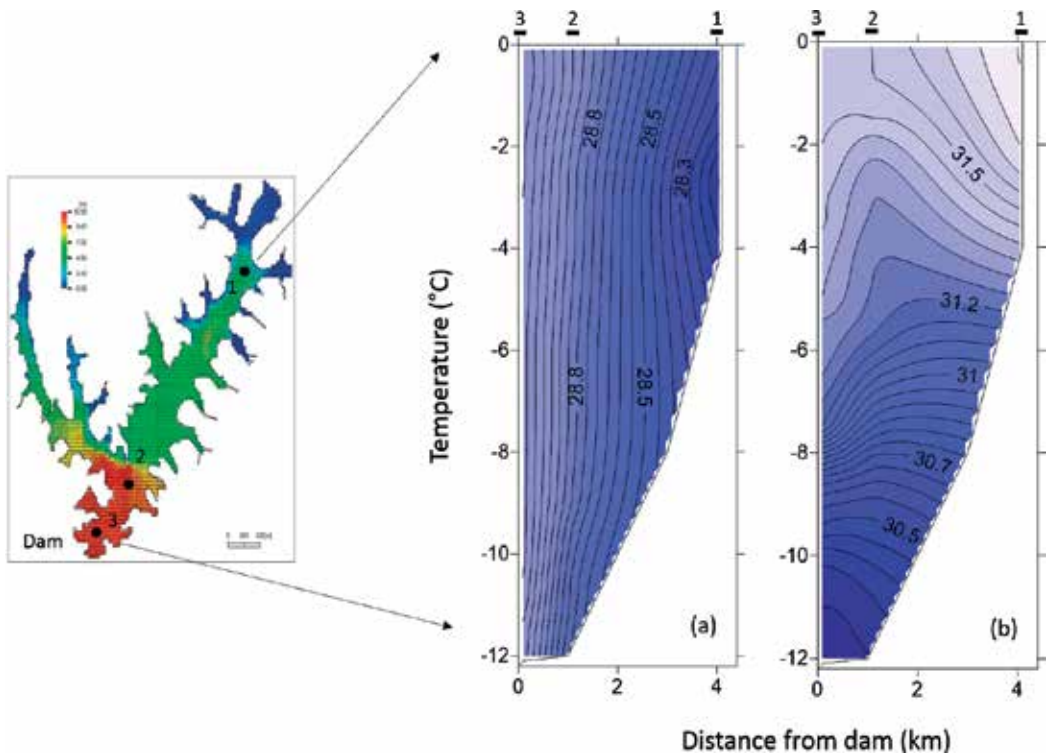


Figure 7. Isotherm in the Durian Tunggal Lake during (a) high wind, well-mixed condition and (b) low wind, differential heating condition. Numbers represent profiling locations.

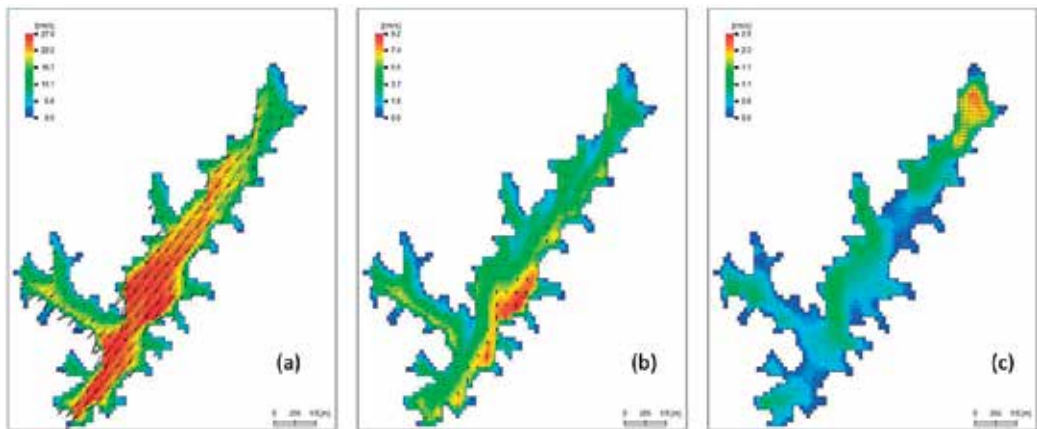


Figure 8. Temperature and current velocity pattern in Durian Tunggal Lake during (a) high wind, (b) mid-wind speed, heavy rain, and (c) low wind.

water from interbasin water transfer from Muar River into the lake. Similar to Bukit Merah, northeast winds are common for Durian Tunggal Lake and such wind direction moved water toward southeast direction (**Figure 8a**). Mid-wind speeds and heavy rain exceeding 50 mm induced mean surface current more than 9.0 cm/s in certain western part of the lake (**Figure 8b**), while low wind induced wind surface current less than 2.5 cm/s (**Figure 8c**). Additionally, higher salinity of the water from interbasin water transfer was reported occasionally which may affect the hydrodynamic features [10]. However, this dynamic is not studied here due to limited observation data. Water level in this man-made lake is very much influenced by the water abstraction.

4. Conclusion

The hydrodynamic studies of the three lakes in Malaysia here indicate distinct variation of the circulation. The mixing regime is shaped by the bathymetry of the lakes in relation to changes in winds, temperature-solar radiation, and inflows. This study found variation in the major driving force of the hydrodynamic pattern between lakes. Hydrodynamic simulations showed that the Bukit Merah and Durian Tunggal reservoirs are more sensitive to wind-driven motion. Bera Lake is more sensitive to flood inflow by the main river during the monsoon season. Convective motion driven by water temperature gradient was important for Bukit Merah and Bera Lake. The horizontal gradient in the former was driven by variation in depth between shallow and deeper regions, while in the latter it was influenced by variation between sheltered areas and open areas. The hydrodynamic models were capable of evaluating the changes in the stratification pattern and physical process created by the effect of the wind on the lake. This will aid in identifying upwelling and downwelling areas and spatial water quality variation and plankton community structure.

The model provides tool for understanding the hydrodynamic characteristics of lakes. The findings from the hydrodynamic analysis, such as water column and circulation pattern generated by the model, will become useful as the basis for the study of the water quality and environmental variations in water bodies.

Acknowledgements

This research was supported by Ministry of Science and Technology of Malaysia, e-Science Fund grant (No. 04-03-09-SF0003). The authors are thankful to Kerian District, Perhilitan RAMSAR Tasek Bera and Syarikat Air Melaka Berhad for allowing us to conduct the research in field. Special thanks to Dr. Saim Suratman and Ir. Ahmad Jamalluddin Shaaban for their helpful support in this project and Kamasuahadi Yasin, Nizam, and Shukor for their technical support in the field.

Author details

Zati Sharip^{1*}, Shahirwan Aman Shah², Aminuddin Jamin³ and Juhaimi Jusoh⁴

*Address all correspondence to: zati@nahrim.gov.my

1 Lake Research Unit, Water Quality and Environment Research Centre, National Hydraulic Research Institute of Malaysia, Ministry of Natural Resources and Environment, Selangor, Malaysia

2 Syarikat Air Melaka Berhad, Malaysia

3 Tasik Bera Ramsar, Perhilitan, Malaysia

4 Perak Drainage and Irrigation Department, Malaysia

References

- [1] Beletsky D, Schwab D. Modeling circulation and thermal structure in Lake Michigan: Annual cycle and interannual variability. *Journal of Geophysical Research*. 2001;**106**(C9): 19745-19771
- [2] Laval B, Imberger J, Findikakis A. Dynamics of a large tropical lake: Lake Maracaibo. *Aquatic Sciences*. 2005;**67**(3):337-349
- [3] Bailey MC, Hamilton DP. Wind induced sediment resuspension: a lake-wide model. *Ecological Modelling*. 1997;**99**:17-228
- [4] Imberger J. Thermal characteristics of standing waters: An illustration of dynamic processes. *Hydrobiologia*. 1985;**125**:7-29
- [5] Lam DCL, Schertzer WM. Potential climate change effects on Great Lakes hydrodynamics and water quality. Reston, VA: ASCE Publications; 1999
- [6] Weinberger S, Vetter M. Using the hydrodynamic model DYRESM based on results of a regional climate model to estimate water temperature changes at Lake Ammersee. *Ecological Modelling*. 2012;**244**(0):38-48
- [7] Fragoso Jr CR et al. Potential effects of climate change and eutrophication on a large subtropical shallow lake. *Environmental Modelling & Software*. 2011;**26**(11):1337-1348
- [8] Vilhena LC, Hillmer I, Imberger J. The role of climate change in the occurrence of algal blooms: Lake Burragarang, Australia. *Limnology and Oceanography*. 2010;**55**(3):1188-1200
- [9] Wetland International-Asia Pacific, UPEN. Tasek Bera RAMSAR site—Integrated Management Plan. Kuantan: Pahang State Economic Planning Unit (UPEN); 1999. p. 178
- [10] Sharip Z, Yusoff FM. Plankton community characterization in shallow tropical lakes. *Journal of Environmental Biology*. 2017;**38**(6):1365-1374

- [11] Hidzrami SA. Bukit Merah Perak, Lake Brief. *Managing Lakes and Their Basins for Sustainable Use in Malaysia (Lake Briefs Report Series 1)*. Kuala Lumpur: Akademi Sains Malaysia; 2010. pp. 29-72
- [12] Hasan ZA, Hamidon N, Yusof MS, Ghani AA. Flow and sediment yield simulations for Bukit Merah Reservoir catchment, Malaysia: A case study. *Water Science and Technology*. 2012;**66**:2170-2176
- [13] Taguchi K, Nakata K. Analysis of water quality in Lake Hamana using a coupled physical and biochemical model. *Journal of Marine Systems*. 1998;**16**:107-132
- [14] Sharip Z, Yanagawa R, Terasawa T. Eco-hydrodynamic modelling of Chini Lake: model description. *Environmental Modelling and Assessment*. 2016;**21**(2):193-210. DOI: 10.1007/s10666-015-9464-4
- [15] Perak DID. A preliminary status of Ecosystem Health of Bukit Merah Lake—Final Report. 2012. p. 57
- [16] Durian Tunggal AR. Dam—Current status and lesson learned. In: *Proceedings of the National Seminar on Research and Management of Lakes and Their Basins for Sustainable Use (Lake Brief Report Series 3)*. Seri Kembangan: National Hydraulic Research Institute of Malaysia; 2013. pp. 34-55
- [17] Sharip Z, Zaki AT. The effects of season and sand mining activities on thermal regime and water quality in a large shallow tropical lake. *Environmental Monitoring and Assessment*. 2014;**186**:4959-4969
- [18] Tundisi JG, Forsberg BR, Devol AH, Zaret TM, Tundisi TM, Santos AD, Ribeiro JS, Hardy ER. Mixing patterns in Amazon lakes. *Hydrobiologia*. 1984;**108**:3-15
- [19] Monismith SG, Imberger J, Morison ML. Convective motions in the sidearm of a small reservoir. *Limnology and Oceanography*. 1990;**35**(8):1676-1702
- [20] Verburg P, Antenucci JP, Hecky RE. Differential cooling drives large-scale convective circulation in Lake Tanganyika. *Limnology and Oceanography*. 2011;**56**(3):910-926
- [21] Sharip Z, Hipsey MR, Schooler SS, Hobbs RJ. Physical circulation and spatial exchange dynamics in a shallow floodplain wetland. *International Journal of Design & Nature and Ecodynamics*. 2012;**7**:274-291
- [22] Lovstedt CB, Bengtsson L. Density-driven current between reed belts and open water in a shallow lake. *Water Resources Research*. 2008;**44**(10):1-13
- [23] Zhang XY, Nepf HM. Density-driven exchange flow between open water and an aquatic canopy. *Water Resources Research*. 2008;**44**(8):1-12
- [24] Nepf HM, Oldham CE. Exchange dynamics of a shallow contaminated wetland. *Aquatic Sciences*. 1997;**59**:193-213

Application of a Hydrodynamic and Water Quality Model for Inland Surface Water Systems

Lubo Liu

Additional information is available at the end of the chapter

<http://dx.doi.org/10.5772/intechopen.74914>

Abstract

This chapter introduces basic concepts, properties, and principles of different processes in inland surface water and analytical methodologies. The fundamentals of surface water hydrodynamics, including water properties, hydrodynamic processes, Cartesian coordinate-based governing equations, and boundary and initial conditions were reviewed. The fate and transport of contaminants in surface water were introduced. Based on aforementioned theory and principles, two hydrodynamic-water quality models were developed for studying a lake and a river, respectively. A stratified 3D model was used to investigate the circulation and *E. coli* transport in the nearshore region of Lake Michigan. The modeling results show that stratified phenomenon exists in the near region, and a 3D model is necessary even though a previous 2D model works well for the shallow water environment. A 2D depth-averaged water quality model was developed to estimate the fate and transport of four contaminants in the San Joaquin River of California. The modeling results indicate that it took 20 days for these contaminants to transport from the upstream to the downstream in the research domain. These models can be effectively used for inland surface water restoration and management.

Keywords: inland, surface water, hydrodynamics, water quality, numerical model

1. Introduction to surface water systems

Inland surface water systems such as rivers, streams, creeks, lakes, reservoirs, and wetlands play a hugely important role in our drinking water supply, agricultural irrigation, industrial utilization, recreational activities, and other public uses. Our everyday lives depend on the availability and quality of surface water. Surface water is in motion in response to natural forces, climatic effects, and human activities, all of which have a significant impact on its

quality. Although surface water systems are governed by many different factors, this chapter focuses primarily on two of the most influential aspects: hydrodynamics and water quality. Water's hydrodynamic characteristics include its flow velocity, water depth, and water surface elevation, while water quality is assessed in terms of its physical (temperature, color, odor, sediments, etc.), chemical (dissolved oxygen, salinity, organic matter and heavy metal content, nutrients, etc.), and biological characteristics (bacteria, viruses, protozoans, etc.). The interactions between the processes related to these characteristics are inevitably fairly complex; water system administrators must therefore seek to develop a good understanding of the dominant factors and processes that affect the water quality of each of the local water resources they are responsible for if they are to make correct or optimized management decisions.

Water quality is represented by the levels of a series of water quality parameters such as water temperature, dissolved oxygen, level of pathogens, and the concentrations of different chemicals, all of which may vary both temporally and spatially. In addition to the inactivation of contaminants, the levels and distribution of contaminants are governed by several dynamic processes, including diffusion, dispersion, and advection. These processes are closely linked to the water's flow characteristics, the influents and effluents entering and leaving the body of water, wind stress, the Coriolis effect (which must be taken into account in large bodies of water such as the Great Lakes), and stratified temperature, among other factors. In turn, the fate and transport of contaminants may influence flow, for example, sediment transport may change flow density. In addition to these common mechanisms shared by all surface water bodies, each will have its own unique characteristics. Therefore, to better understand how a particular surface water system functions, essential knowledge of its hydrodynamic and water quality related processes must be supplemented by information regarding its specific characteristics.

The methods typically used to study the surface water systems include theoretical analyses, mathematical modeling, laboratory experiments, and field observations. Experiments and observations are the most reliable ways to acquire real information for a specific system that will provide a good basis for analysis and modeling. However, for a complex surface water body, the observed or measured data are usually far from sufficient to reflect or predict a complete picture of the real scenario. Furthermore, the available data are not necessarily totally reliable, and low quality data with high errors may lead researchers to build a false or misleading idea of what is actually happening. Therefore, mathematical modeling coupled with observations for verification and calibration is essential in such cases. Hydrodynamic and water quality models have been widely developed and used for the investigations of rivers [1–4], lakes or reservoirs [5–11], estuaries [12, 13], and coastal waters [14, 15] on various aspects. These models have been effective tools for explaining, simulating, and forecasting the complex processes in water environment.

This chapter focuses on the fundamental concepts and principles of surface water analysis, and the application of a model that combines hydrodynamics and water quality. The goals are to help develop a better understanding of the different hydrodynamic processes involved to facilitate decision making in real surface water systems. After a discussion on the fundamentals of surface water hydrodynamics (Section 2), contaminant fate and transport in surface water and a water quality model will be discussed. This chapter concludes with a discussion of two case studies of very different surface water systems, the southern part of Lake Michigan and the upper reaches

of the San Joaquin River in California, to illustrate how these theoretical predictions compare to the hydrodynamic and water quality properties observed in real bodies of water.

2. Fundamentals of surface water hydrodynamics

Hydrodynamics deals with the motion of water and the forces acting on water. Hydrodynamic studies focus on investigating the mechanisms driving flow by quantifying the key physical processes in water. The results obtained provide invaluable information on the movement and transport of contaminants, which serves as the basis for all research into water quality. The information needed to develop a hydrodynamic model includes a comprehensive set of governing equations that describe the physical processes involved and the associated initial and boundary conditions required to numerically solve the equations, and the various parameters that must be input to run the model.

2.1. Water properties and hydrodynamic processes

In hydrodynamics, the main property parameters of water are its density/specific weight and its viscosity, both of which have a significant impact on the solutions to the governing equations. The density of water can vary depending on the temperature, concentration of the suspended solids, and salinity. The influence of these factors on water density has been formulated as follows [16]:

$$\rho = \rho_T + \Delta\rho_S + \Delta\rho_C \quad (1)$$

where ρ_T is the density of pure water as a function of temperature T [17, 18], $\Delta\rho_S$ is the change in density due to salinity S , and $\Delta\rho_C$ is the change in density due to total suspended sediments [19].

Viscosity represents the internal friction of water and is very important for hydrodynamic processes. The kinematic viscosity (m^2/s) of a river can be approximated as a function of temperature T ($^{\circ}\text{C}$) [20].

$$\nu = (1.785 - 0.0584T + 0.00116T^2 - 0.0000102T^3) \times 10^{-6} \quad (2)$$

Here, hydrodynamic processes refer to water motion, circulation, mixing phenomena; the corresponding processes involving the materials suspended in the water include advection, dispersion and mixing. The results combine to form a hydrodynamic model that generally includes flow field, water depth and water surface elevation, salinity, temperature, and sediment concentration. Some of this information, for example, which related to temperature, salinity, and/or sediment, may also be utilized in water quality models.

2.2. Cartesian coordinate-based governing equations

The governing equations for both water flow and the transport of contaminants are based on the conservation laws of mass, momentum, and energy. Hydrodynamic models include two main types of governing equations: continuity equation for the mass balance of water in the

Model dimensions	Characteristics	Applications
Zero	Completely mixed, no flow, spatially uniform	Estimation of ponds, lakes, tanks with no or low flow
One	Shallow narrow flow, well mixed, spatial variation in transverse and vertical directions neglected	Long creeks, rivers, streams, narrow channels
Two (horizontal)	Shallow wide flow, well mixed, spatial variations in vertical direction neglected	Wide open lakes and estuaries (weakly stratified), ponds, wide shallow river reaches
Two (vertical)	Deep narrow flow, spatial variation in lateral direction neglected	Narrow and deep lakes, reservoirs, river reaches (strongly stratified)
Three	Deep, stratified flow, significant variation in vertical direction, all three directions considered	Deep large lakes, reservoirs, coastal regions, estuaries

Table 1. Examples of different dimensional models and their applications.

flow and momentum equation that indicates the relationship between the driving forces and water acceleration of motion, which is Newton's second law. The forces acting on a water body include gravity, viscous force, and pressure as well as other external forces such as wind and the Coriolis force. The momentum equation in most hydrodynamic models is a simplification and/or modification of the Navier-Stokes equation. Most natural surface water systems are characterized as "shallow water," where the horizontal scale is far greater than the water depth. The hydrostatic assumption, which assumes that the hydrostatic balance in the vertical plane and the vertical acceleration can be neglected, also applies to shallow water. Technically, all surface water systems are three-dimensional scenarios, and a fully 3D model would thus provide the most complete description of their flow features, but the resulting model would be far too complex for the governing equations to be solved. Under most circumstances, it is reasonable to use a 1D, 2D, or quasi-3D model as this provides sufficient accuracy to solve nearly all practical problems. Based on the representation and spatial scale of water body and application purposes, a number of different dimensional models have been developed by researchers. Examples of these models and their applications are listed in **Table 1**. Their governing equations for continuity and momentum are described as follows [20] (2.2.1), [16, 20] (2.2.3), [21] (2.2.2), [23] (2.2.4).

2.2.1. 1D equations

2.2.1.1. Continuity equation

$$\frac{\partial A}{\partial t} + \frac{\partial(Au)}{\partial x} = 0 \quad (3)$$

2.2.1.2. Momentum equation

$$\frac{\partial(Au)}{\partial t} + \frac{\partial(Au^2)}{\partial x} + gA \left[\frac{\partial(a+h)}{\partial x} \right] - \frac{1}{\rho} \frac{\partial}{\partial x} \left(\varepsilon_{xx} A \frac{\partial u}{\partial x} \right) - \frac{1}{\rho} (B\tau_{sx} - \lambda\tau_{bx}) = 0 \quad (4)$$

where A is the cross sectional area, u is the flow velocity averaged over the cross section, a is the elevation of channel bottom, h is the water depth, ε_{xx} is the horizontal eddy coefficient, B is the channel width at the water surface, λ is the wetted perimeter of the cross section, τ_{sx} is the wind stress acting on water surface, and τ_{bx} is the frictional stress on bottom and bank surface [20].

2.2.2. Depth-averaged 2D equations

2.2.2.1. Continuity equation

$$\frac{\partial h}{\partial t} + u \frac{\partial(h)}{\partial x} + v \frac{\partial(h)}{\partial y} + h \left(\frac{\partial u}{\partial x} + \frac{\partial v}{\partial y} \right) = 0 \quad (5)$$

2.2.2.2. Momentum equations

$$h \frac{\partial u}{\partial t} + hu \frac{\partial u}{\partial x} + hv \frac{\partial u}{\partial y} - fvh = \frac{1}{\rho} \left[\frac{\partial}{\partial x} \left(\bar{\varepsilon}_{xx} h \frac{\partial u}{\partial x} \right) + \frac{\partial}{\partial y} \left(\bar{\varepsilon}_{xy} h \frac{\partial u}{\partial y} \right) \right] - gh \left(\frac{\partial a}{\partial x} + \frac{\partial h}{\partial x} \right) - \frac{ugn^2 \sqrt{(u^2 + v^2)}}{h^{1/3}} + \zeta W^2 \cos \psi \quad (6)$$

$$h \frac{\partial v}{\partial t} + hu \frac{\partial v}{\partial x} + hv \frac{\partial v}{\partial y} - fuh = \frac{1}{\rho} \left[\frac{\partial}{\partial x} \left(\bar{\varepsilon}_{yx} h \frac{\partial v}{\partial x} \right) + \frac{\partial}{\partial y} \left(\bar{\varepsilon}_{yy} h \frac{\partial v}{\partial y} \right) \right] - gh \left(\frac{\partial a}{\partial y} + \frac{\partial h}{\partial y} \right) - \frac{vgn^2 \sqrt{(u^2 + v^2)}}{h^{1/3}} + \zeta W^2 \sin \psi \quad (7)$$

where u, v are the depth-averaged velocities in the x, y directions, respectively, W is the wind velocity, ψ is the wind direction, ζ is the empirical wind coefficient; f is the Coriolis parameter, g is the acceleration due to gravity, n is the Manning's roughness coefficient, and $\bar{\varepsilon}$ is the depth-averaged eddy viscosity. Horizontal mixing is described using the Smagorinsky eddy parameterization:

$$\bar{\varepsilon} = 2A_m = \alpha A \left[\left(\frac{\partial u}{\partial x} \right)^2 + \left(\frac{\partial v}{\partial y} \right)^2 + \frac{1}{2} \left(\frac{\partial u}{\partial y} + \frac{\partial v}{\partial x} \right)^2 \right]^{\frac{1}{2}} \quad (8)$$

where α is a constant in the range 0.01–0.5 [22] and A_m is the area of the current element based on the finite element scheme [21].

2.2.3. Lateral-averaged 2D equations

2.2.3.1. Continuity equation

$$\frac{\partial(Bu)}{\partial x} + \frac{\partial(Bw)}{\partial z} = 0 \quad (9)$$

where u is the lateral averaged velocity in the x direction, w is the lateral averaged velocity in the z direction, and B is the water width.

2.2.3.2. Momentum equation

$$\frac{\partial(Bu)}{\partial t} + \frac{\partial(Bu^2)}{\partial x} + \frac{\partial(uwB)}{\partial z} + gB \frac{\partial(z_s)}{\partial x} - \frac{\partial}{\partial x} \left(BA_H \frac{\partial u}{\partial x} \right) - \frac{\partial}{\partial x} \left(BA_v \frac{\partial u}{\partial z} \right) - \tau_x = 0 \quad (10)$$

where A_H is the horizontal eddy viscosity, A_v is the vertical turbulent mixing coefficient, and z_s is the water surface elevation. For gradually varying flows, the z-direction momentum equation can be neglected due to the insignificant effects of inertia, diffusion, and dispersion in the vertical direction [16, 20].

2.2.4. 3D stratified flow equations

2.2.4.1. Continuity equation

$$\frac{\partial u}{\partial x} + \frac{\partial y}{\partial y} + \frac{\partial w}{\partial z} = 0 \quad (11)$$

Based on the hydrostatic assumption Eq. (12), vertical momentum equations can be eliminated from 3D governing equations.

$$\frac{\partial p}{\partial z} + \rho g = 0 \quad (12)$$

For the purposes of this analysis, a water system is divided into a series of horizontal layers that interact with each other. The topography of a real 3D environment is generally nonuniform, and the bathymetry may spatially differ over a wide range. To avoid any problems due to the nonuniform water depth, it is necessary to transform the system to a constant geometric structure with uniform resolution. Based on the Sigma method [16, 23, 24], a transformation scheme was developed as follows:

$$\begin{aligned} x' &= x \\ y' &= y \\ z' &= a + \frac{(z-a)(b-a)}{h} \end{aligned} \quad (13)$$

where x', y', z' are the transformed coordinates, p is the water pressure, g is the acceleration due to gravity, ρ is the water density, z is the vertical coordinate, a is the bottom elevation, and b is the fixed vertical location to which the water surface will be transformed. Thus, the continuity equation and momentum equations along the horizontal direction are as follows [23]:

$$\begin{aligned} \frac{\partial h}{\partial t} + \int_a^b \left[\frac{\partial u}{\partial x} - \frac{(b-a)}{h} \frac{\partial u}{\partial z} T_x + \frac{\partial v}{\partial y} - \frac{(b-a)}{h} \frac{\partial v}{\partial z} T_y \right] dz + u_s \frac{\partial(a+h)}{\partial x} - u_b \frac{\partial a}{\partial x} \\ + v_s \frac{\partial(a+h)}{\partial y} - v_b \frac{\partial a}{\partial y} = 0 \end{aligned} \quad (14)$$

$$\begin{aligned} & \rho h \frac{\partial u}{\partial t} + \rho hu \frac{\partial u}{\partial x} + \rho hv \frac{\partial u}{\partial y} + \rho \frac{\partial u}{\partial z} \left[(b-a)(w - uT_x - vT_y) - (z-a) \frac{\partial h}{\partial t} \right] \\ & - (b-a) \frac{\partial}{\partial x} \left(\varepsilon_{xx} \frac{h}{(b-a)} \frac{\partial u}{\partial x} \right) - (b-a) \frac{\partial}{\partial y} \left(\varepsilon_{xy} \frac{h}{(b-a)} \frac{\partial u}{\partial y} \right) \\ & - (b-a) \frac{\partial}{\partial z} \left(\varepsilon_{xz} \frac{\partial u}{\partial z} \right) + \rho_s gh \frac{\partial a}{\partial x} + \rho_s gh \frac{\partial h}{\partial x} + g_x h - \Gamma_x = 0 \end{aligned} \quad (15)$$

$$\begin{aligned} & \rho h \frac{\partial v}{\partial t} + \rho hu \frac{\partial v}{\partial x} + \rho hv \frac{\partial v}{\partial y} + \rho \frac{\partial v}{\partial z} \left[(b-a)(w - uT_x - vT_y) - (z-a) \frac{\partial h}{\partial t} \right] \\ & - (b-a) \frac{\partial}{\partial x} \left(\varepsilon_{yx} \frac{h}{(b-a)} \frac{\partial v}{\partial x} \right) - (b-a) \frac{\partial}{\partial y} \left(\varepsilon_{yy} \frac{h}{(b-a)} \frac{\partial v}{\partial y} \right) \\ & - (b-a) \frac{\partial}{\partial z} \left(\varepsilon_{yz} \frac{\partial v}{\partial z} \right) + \rho_s gh \frac{\partial a}{\partial y} + \rho_s gh \frac{\partial h}{\partial y} + g_y h - \Gamma_y = 0 \end{aligned} \quad (16)$$

where u, v, w are the velocities in the x, y, z direction, respectively, ε_{ij} is the turbulent eddy coefficient ($i, j = x, y, z$), Γ_i is the external tractions on the water body, and ρ_s is the density at the water surface. Subscripts s and b denote surface and bottom, respectively.

Eddy viscosity can be determined using a number of different methods, but the Mellor Yamada formulation [25] and the Smagorinsky [22] method are the among most widely used methods for the horizontal and vertical eddy viscosity, respectively.

2.3. Boundary and initial conditions

To numerically solve these governing equations, boundary conditions (and initial conditions for transition problems) must be specified for all external surfaces of the water body. Boundaries of a surface water system consist of the top water surface and the bottom and side surfaces. Accordingly, the water surface elevation, the velocities at the bottom and side surfaces, and the flux (if sediment and salinity are to be considered) at all boundaries must be specified.

2.3.1. The free water surface

There is zero pressure on the water surface and no leakage across the water surface.

$$w_s = \frac{dh}{dt} \quad (17)$$

where w_s is the vertical velocity at the water surface. There may also be some external surface traction, such as wind stress, acting on the water surface.

2.3.2. The bottom surface

Two types of boundary conditions are applied to the bottom surface [23], which will be either a no leakage boundary or a no slip boundary ($u_b = v_b = w_b = 0$) condition.

2.3.3. *The side surface*

The side surface refers to the shoreline of the water body or a defined boundary of the model such as the entrance or exit of a river reach. The shoreline conditions are zero normal velocity, that is, no leakage across the boundary surface. Information on the water surface elevation, velocities, or flow rate need to be specified for the defined boundaries, but combinations of different conditions should be avoided on the same boundary.

2.3.4. *Other boundary conditions*

In addition to the required boundary conditions mentioned earlier, some frictional stresses Γ_i in the governing equations may act on the surfaces of water body so the corresponding conditions should be added to the model. Common stresses include wind stress (Γ_{WX} and Γ_{WY}) and frictional stress (Γ_{BX} and Γ_{BY}).

2.3.5. *Initial conditions*

A dynamic model requires a set of initial values to be input in order to begin to solve the governing equations. The model needs a “best guess” set of conditions for all the nodes in the mesh at the beginning of the iterative process; a bad initial guess that is far from the real conditions will adversely affect the convergence, slowing down the process immensely. A commonly used strategy is to have the whole water body at rest with a constant water surface elevation (WSE) when $t = 0$. The real initial scenario generally emerges after running the simulation for a period from this initial state.

2.4. Parameters and data for the hydrodynamic model

Many different types of data are needed as input or to determine the controlling parameters when running a hydrodynamic model. The data used as direct input include the geographic coordinates of the shoreline, bathymetry, flow rate, water surface elevation, meteorological data such as wind speed and direction, radiation intensity, air pressure, precipitation and the evaporation rate, among others. In addition to the input data, data on the flow rate, velocities, water depth, and water surface elevation at other locations than the boundaries are also needed to calibrate the model to determine hard to measure parameters such as the roughness of the bottom and the horizontal momentum diffusion coefficient [16], and to confirm that the model accurately reflects the real scenario. The modeling results are compared to the data measured either in the laboratory or in the field for the model calibration and verification.

3. Water quality model

Water quality, which includes its physical, chemical, biological, and other characteristics, is predominantly controlled by the hydrodynamic processes and the various mechanisms governing the fate and transport of contaminants. Once a contaminant enters a water system, its concentration is determined by its chemical and biological reactions and hydrodynamic transport processes, including advection, dispersion, and vertical mixing. Water quality models

are widely used to reflect these processes. Some examples of water quality model applications include the simulation and prediction of water temperature, dissolved oxygen (DO), biochemical oxygen demand (BOD), the nitrogen cycle (including levels of organic nitrogen, ammonia, nitrite and nitrate), the phosphorous cycle (including levels of organic phosphorous and phosphates), algae growth and decay, cohesive/noncohesive suspended sediment, salinity, heavy metals, and pathogens, among others [27]. Depending on the results for advection, dispersion, and turbulent mixing obtained from the hydrodynamic model, water quality models may also incorporate the sources/sinks, chemical and biological reactions of contaminants.

3.1. Governing equations for contaminant fate and transport

The governing equations for contaminant fate and transport are as follows [16, 21, 23]:

3.1.1. 1D equation

$$\frac{\partial(A_s C)}{\partial t} + \frac{\partial(Au C)}{\partial x} - \frac{\partial}{\partial x} \left(D_x A \frac{\partial C}{\partial x} \right) - k A_s C \pm G = 0 \quad (18)$$

3.1.2. 2D depth-averaged equation

$$\begin{aligned} \frac{\partial(hC)}{\partial t} + u \frac{\partial(hC)}{\partial x} + v \frac{\partial(hC)}{\partial y} - \frac{\partial}{\partial x} \left(D_x h \frac{\partial C}{\partial x} + D_{xy} h \frac{\partial C}{\partial y} \right) \\ - \frac{\partial}{\partial y} \left(D_{xy} h \frac{\partial C}{\partial x} + D_y h \frac{\partial C}{\partial y} \right) - khC \pm G = 0 \end{aligned} \quad (19)$$

3.1.3. 2D laterally averaged equation

$$\begin{aligned} \frac{\partial(BC)}{\partial t} + u \frac{\partial(uBC)}{\partial x} + v \frac{\partial(wBC)}{\partial z} - \frac{\partial}{\partial x} \left(BD_x \frac{\partial C}{\partial x} \right) - \frac{\partial}{\partial x} \left(BD_z \frac{\partial C}{\partial z} \right) \\ - khC \pm G = 0 \end{aligned} \quad (20)$$

3.1.4. 3D stratified equation

$$\begin{aligned} h \frac{\partial C}{\partial t} + h \frac{\partial(uC)}{\partial x} + h \frac{\partial(vC)}{\partial y} + (b-a) \frac{\partial(wC)}{\partial z} - (b-a) T_x \frac{\partial(uC)}{\partial z} \\ - (b-a) T_y \frac{\partial(vC)}{\partial z} - h \frac{\partial}{\partial x} \left(D_x \frac{\partial C}{\partial x} + D_{xy} \frac{\partial C}{\partial y} \right) + h \frac{\partial}{\partial x} \left[\frac{(b-a)}{h} (D_x T_x + D_{xy} T_y) \frac{\partial C}{\partial z} \right] \\ + (b-a) T_x \frac{\partial}{\partial z} \left(D_x \frac{\partial C}{\partial x} + D_{xy} \frac{\partial C}{\partial y} \right) - (b-a) T_x \frac{\partial}{\partial z} \left[\frac{(b-a)}{h} (D_x T_x + D_{xy} T_y) \frac{\partial C}{\partial z} \right] \\ - h \frac{\partial}{\partial y} \left(D_{xy} \frac{\partial C}{\partial x} + D_y \frac{\partial C}{\partial y} \right) + h \frac{\partial}{\partial y} \left[\frac{(b-a)}{h} (D_{xy} T_x + D_y T_y) \frac{\partial C}{\partial z} \right] \\ + (b-a) T_y \frac{\partial}{\partial z} \left[\frac{(b-a)}{h} (D_{xy} T_x + D_y T_y) \frac{\partial C}{\partial z} \right] \\ - (b-a) \frac{\partial}{\partial z} \left[D_z \frac{(b-a)}{h} \frac{\partial C}{\partial z} \right] - khC \pm G - (b-a) \frac{\partial(v_s C)}{\partial z} = 0 \end{aligned} \quad (21)$$

where C is the concentration of the contaminant or temperature, A is the cross-sectional area, A_s is the storage cross-sectional area, D_i is the turbulent diffusion coefficient in the i direction, G is a general term representing sources or sinks, and k is the first order decay or reproductive rate coefficient [23]. These equations represent the first order case; other reaction rates (such as zero order or second order) are described using different expressions for the source term. The terminology used for the other variables is same as that used in Section 2.

3.2. Boundary and initial conditions

Contaminants may be released into a water system via one of two modes: constant release or pulsed release. For both, the initial condition is $C(x, t = 0) = C_0$, where C_0 is the initial concentration that can be assigned as a constant such as the background concentration. The boundary condition for the free surface, bottom and side surfaces is the no flux condition, $\frac{\partial C}{\partial n} = 0$, where n represents the coordinates in the direction normal to the boundary. Other observed concentrations are assigned to the inflow and outflow boundaries.

3.3. Parameters and data for the water quality model

For a water quality model, numerous parameters and data are needed as input. Initial values for these parameters are obtained from the literature, measured directly, or determined via model calibration. The modeling results for various values of the parameter are then compared against the observed data, and the value that achieves the best match is selected for further modeling runs.

Water quality models are fairly complex due to the multiple interrelationships among the many processes controlling the fate and transport of contaminants. Many of these processes can only be described using empirical formulations, which need adequate data for verification and calibration. Data quantity and quality are thus keys for developing and applying a water quality model. In the remainder of this chapter, finite element model RMA10 is used as the hydrodynamic model and RMA11 as the water quality model in the discussion [23].

4. Case studies

Two case studies, the application of a hydrodynamic model in a lake and a water quality model in a river, are presented in this section to show how the respective models are applied for real world surface water systems.

4.1. Case study 1: Southern Lake Michigan

4.1.1. Background

Water quality in the nearshore region of southern Lake Michigan had a problem with contamination by fecal bacteria from various sources. For Great Lakes beaches, fecal pollution attracted a great deal of attention from both beach managers and the public due to its potential

risk to human health, triggering many beach closures and advisories every year with a consequent significant loss to local economies along the shoreline. Predictive modeling has been suggested as an effective approach to enhancing measurements of water quality both temporally and spatially, thus reducing the damage caused by improving the beach management. This case study was therefore conducted to develop a nearshore transport model for fecal pollution in Lake Michigan. The resulting model can be used to inform beach goers promptly in order to protect them from any potential exposure to waterborne pathogens and to help develop a better understanding of the key processes and factors influencing the fate and transport of fecal pollution in the nearshore reaches of the lake. As the indicators of fecal bacteria, *Escherichia coli* (EC) and enterococci (ENT) were used to evaluate the water quality at a recreational beach. In such environments, modeling nearshore, wind-driven circulation and the transport of EC and ENT are particularly challenging due to the interactions with complex lake-wide circulation. Originally, a 2D depth-averaged model was developed to simulate the entire lake with finer meshes close to the shoreline to emphasize the nearshore region [21]. The modeling results show that the current in nearshore region flew predominately along the shoreline direction and the cross-shoreline flow was fairly weak. Therefore, within an acceptable error tolerance range, the entire lake can be simplified as a narrow channel along the shoreline to significantly save computation efforts for nearshore process investigations. With this simplification, current flows only in clockwise or anticlockwise direction along the shoreline, and the exchanging process of mass and momentum in cross-shoreline direction only occur within the channel [26]. Later investigation indicates that the current in vertical direction sometimes cannot be neglected in such lake environment, and thus, a stratified 3D model may be necessary to explain the hydrodynamic and transport processes along the water depth. In this case study, a new 3D model for the domain model was developed based on the aforementioned channelized 2D model. Some 3D modeling results are reported in the following sections.

4.1.2. Investigation domain and model mesh

This case study focused on the nearshore regions along approximately 100 km of the shoreline of southern Lake Michigan. Based on the channelization simplification [26], the computational domain included a 5-km wide channel throughout the entire Lake Michigan shoreline (**Figure 1**). To fairly delineate the complex shoreline, a finite element model with a 3D nonuniform mesh was used. The mesh was gradually refined from a resolution of approximately 1–2 km at the locations far from the research domain to 100 m in the research area. Four streams are the primary tributaries discharging into southern Lake Michigan: Trail Creek (TC) at the Michigan City Harbor (USGS 04095380), Kintzele Ditch (KD) nearby Michigan City, Burns Ditch at Portage, IN (BD, USGS 04095090), and Indiana Harbor Canal (IHC) at East Chicago. As KD and TC both discharge combined sewer flows (CSOs), these are the most significant sources of EC and ENT so Mt. Baldy beach, which is located between the two, was chosen as the nearshore beach for this investigation (**Figure 1**).

4.1.3. Data collection

Major factors considered in the model included the bathymetry, the shape of the lake shoreline, wind stress, hydrological flows from the tributaries, and water temperature. Bathymetric data

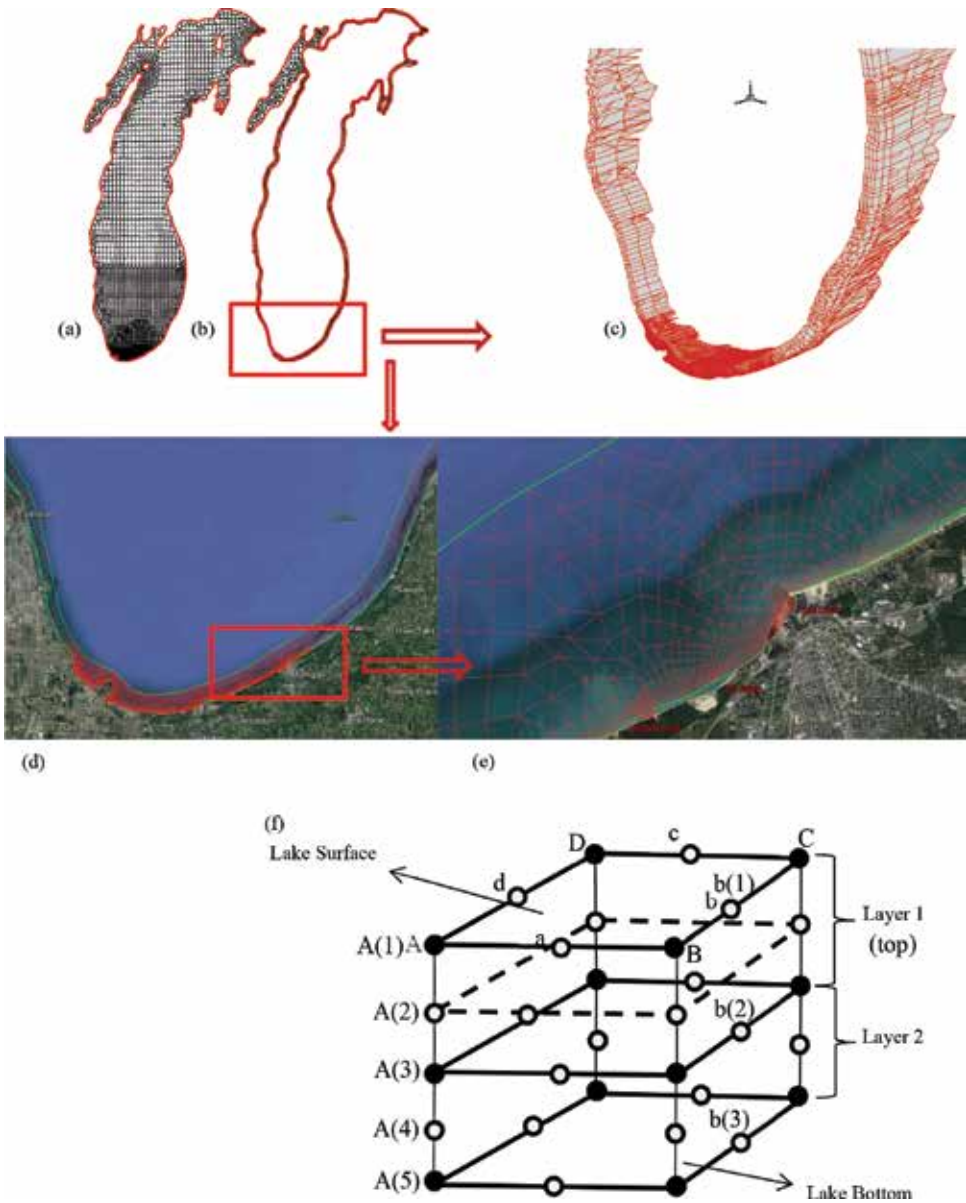


Figure 1. (a) Whole lake model mesh (2D), (b) channelized mesh (2D), (c) channelized mesh (3D), (d) Google Earth satellite image with the channelized mesh, (e) enlarged research domain with mesh, and (f) scheme of node distribution in quadratic a 3D element mesh.

with a resolution of 3 arc-seconds were obtained from the NOAA’s National Geophysical Data Center. As inputs of the model, hourly meteorological data, including wind speed and direction, air temperature, dew point temperature, air pressure, and sunlight insolation were obtained from six stations run by NOAA’s National Climatic Data Center and two buoys belonging to NOAA’s National Data Buoy Center (NDBC). Data on current velocity and WSE were also collected from several stations for model calibration.

4.1.4. Hydrodynamic and water quality model

4.1.4.1. Model description

Although a 2D depth-averaged model based on the finite element model RMA10 [21, 26] can well describe the wind-driven circulation at the particular location in Lake Michigan during the specific period, the transport phenomenon along the water depth is fairly significant for other contaminants at other locations [27]. Therefore, a stratified 3D hydrodynamic and water quality model was developed to address the vertical current and transport. The model was employed to simulate current velocity, water depth, water surface elevation, water temperature, and EC. The model principles and setup, including the governing equations, boundary conditions, and initial conditions, were those described earlier in Sections 2 and 3. The governing equations were thus Eqs. (11)–(16) for the hydrodynamic model and Eq. (21) for the water quality model. A constant value of 2.0 m²/s was used for both the eddy viscosity and the turbulent diffusion coefficient in the nearshore region. The water body was evenly divided into three layers, and thus, there are totally either five nodes (for the corner points in a finite element) or three nodes (for the mid-points in a finite element) at each location throughout the water depth. **Figure 1f** shows the nodes constituting a typical finite element in the 3D mesh. A quadratic finite element consists of corner nodes (solid dots such as A, B, C, and D) and middle nodes (empty dots such as a, b, c, and d). In this two-layer mesh, four and two nodes are placed under each corner and middle node at the water surface, respectively. Therefore, there are totally five (e.g., A(1)–A(5)) or three (e.g., a(1)–a(3)) nodes from the lake surface to the bottom.

4.1.4.2. Initial and boundary conditions

The initial conditions used to model EC were the lake at rest and a background value of 3 CFU/100 mL, based on general observations. The observed water temperatures at the different stations were interpolated into the mesh for the thermal model when $t = 0$. The boundary conditions for the hydrodynamic model included the no leakage condition across the surface and the bottom, zero pressure and wind stress at the free surface, drag at the bottom surface, and the flow loading from the tributaries. For the water quality model, EC and ENT data were loaded for both TC and KD, and the loading rates were monitored at the stream mouths.

4.1.4.3. Fate and transport of EC and ENT

In addition to determining the hydrodynamic transport processes in the water body, estimating the activation rate of EC and ENT is another key issue in the model. The common factors affecting the fate and transport of EC and ENT include sunlight, nutrient content, salinity, suspended solids, sedimentation, water temperature, pH, and predation. Based on the important inactivation mechanisms reported in the literature, a time-dependent inactivation rate was used, which considered solar insolation, sedimentation, and water temperature, as shown below:

$$\underbrace{k(I, T, v_s)}_{(1)} = \left[f_p \frac{v_s}{H} + k_l I(t) \right] \theta^{(T-20)} = \underbrace{f_p \frac{v_s}{H} \theta^{(T-20)}}_{(2)} + \underbrace{k_l I(t) \theta^{(T-20)}}_{(3)} \quad (22)$$

where $k(I, T, v_s)$ is the overall inactivation rate, k_l is the inactivation rate for light, $I(t)$ is the measured solar insolation, θ is the temperature correction factor (usually 1.07), f_p is the

fraction of pathogens attached to the suspended sediment, v_s is the settling velocity, and H is the water column depth.

4.1.5. Model calibration

The hydrodynamic model was calibrated by adjusting the Manning's roughness coefficient, n after examining the sensitivity of model currents to the horizontal viscosity. The modeling results were compared with Acoustic Doppler Current Profiler (ADCP) data collected at Burns Ditch (July 2–August 14). **Figure 2** shows these comparisons. A constant bed roughness value of 0.1 leading to a minimum root mean square error (RMSE, Eq. (23)) was finally used in the model. The modeling results for the current velocity and WSE were generally consistent with known circulation patterns in southern Lake Michigan.

$$RMSE = \sqrt{\frac{1}{N} \sum_{i=1}^N [\log_{10}(X_{sim}) - \log_{10}(X_{obs})]^2} \quad (23)$$

where X_{sim} , X_{obs} are the simulated results and the observed data, (referring to the concentrations in this case study), respectively.

4.1.6. Results and discussion

In addition to the previous published 2D modeling investigation of the domain, we examined the 3D modeling results. The modeling concentrations of EC and water temperatures at

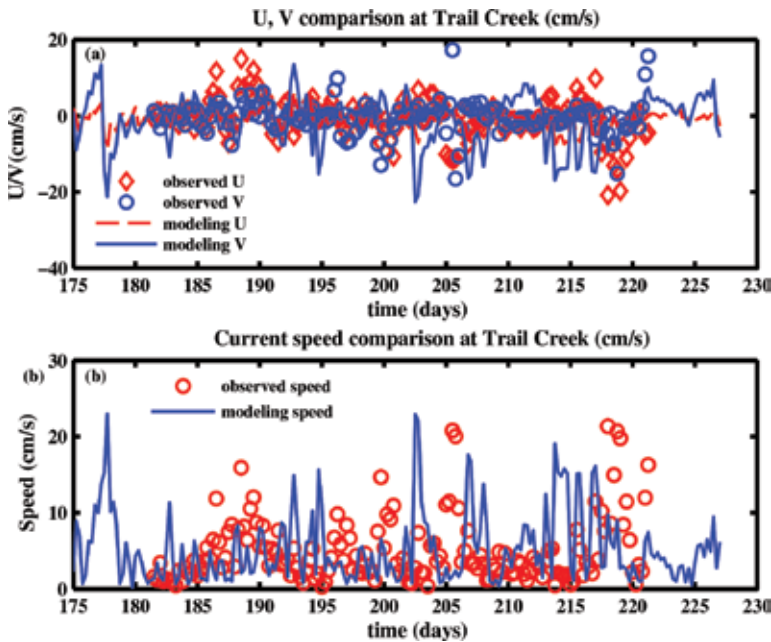


Figure 2. Comparison of (a) velocity component and (b) speed between data and 3D modeling results (lake surface).

different depth at the sampling locations were compared with the observed data (Figures 3 and 4). Time-dependent inactivation rate based on temperature, sedimentation, and observed solar insolation (Eq. (22)) was used to simulate EC inactivation. The same parameter values as those in the 2D models were used for the 3D model, which include a k_I value of $0.0026 \text{ W}^{-1}\text{m}^2\text{d}^{-1}$, a fraction f_p of 0.1, and a v_s value of 5 m per day. The modeling results at different depth showed a similar pattern of temporal variation, which can reasonably describe the data. Generally, both the speed and the magnitude of velocity components tend to decrease

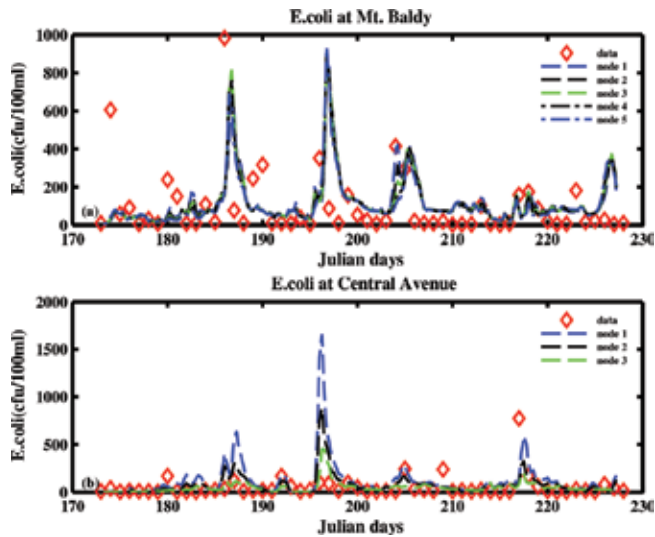


Figure 3. Comparison of *E. coli* between data and 3D modeling results at (a) Mt. Baldy and (b) Central Avenue.

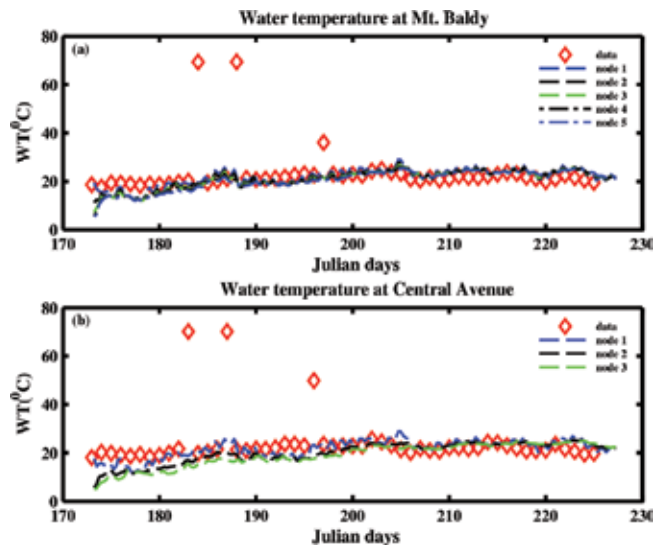


Figure 4. Comparison of temperature between data and 3D modeling results at (a) Mt. Baldy and (b) Central Avenue.

with depth (U, V, W and Speed in **Figures 5–7**). The water temperatures at water surface are higher than those below and the lake bottom has the minimum value. **Figures 8 and 9** show the contour of *E. coli* reflecting its transport and fate and water temperature distribution at different time. The model was able to reasonably describe the observed data.

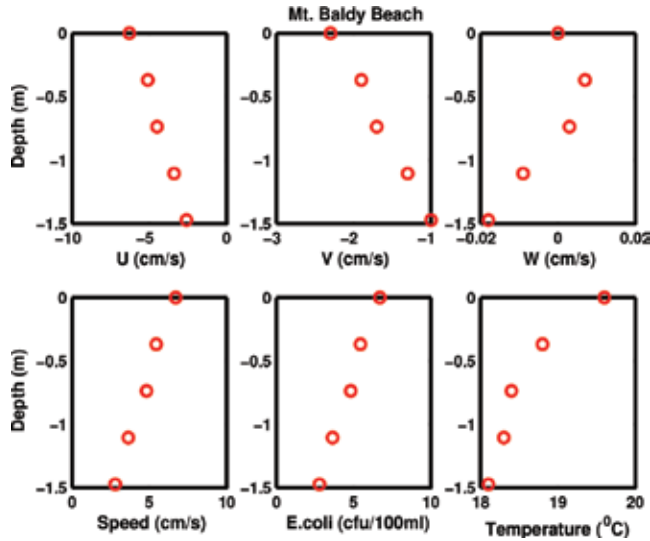


Figure 5. Distribution of calculated parameters along water depth at Julian day 210 at Mt. Baldy Beach.

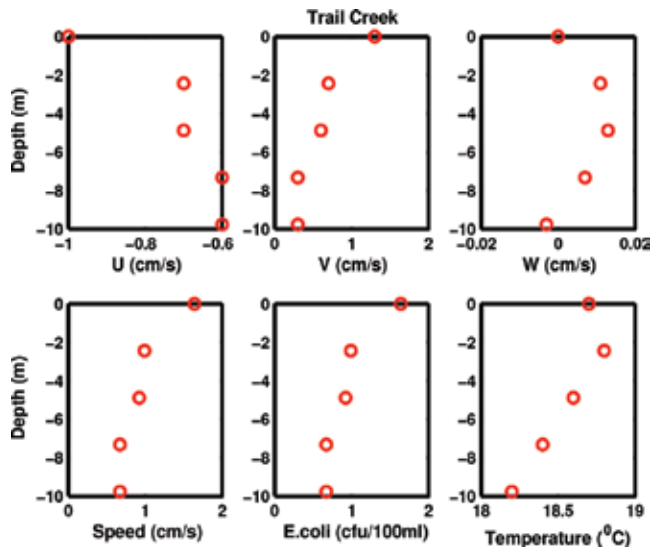


Figure 6. Distribution of calculated parameters along water depth at Julian day 210 at Trail Creek.

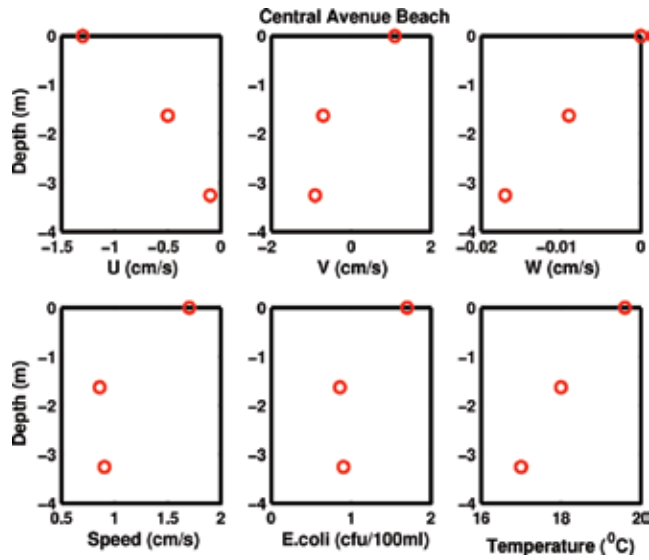


Figure 7. Distribution of calculated parameters along water depth at Julian day 210 at Central Avenue Beach.

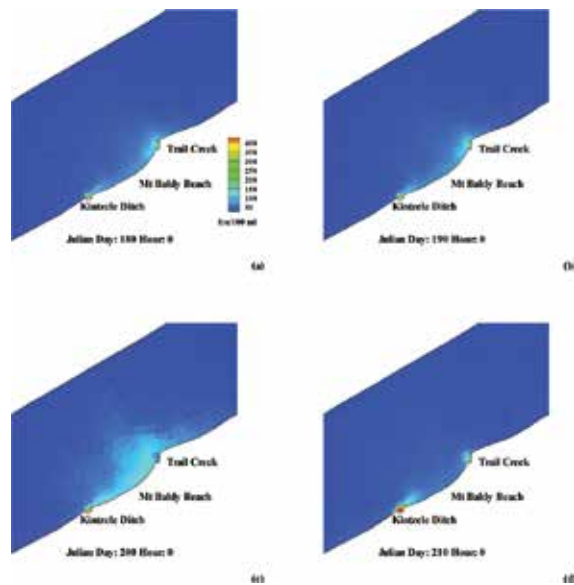


Figure 8. Spatial distribution of *E. coli* at 12:00 am on Julian day: (a) 180, (b) 190, (c) 200, and (d) 210.

4.2. Case study 2: Upper San Joaquin River

4.2.1. Background

The San Joaquin River (SJR) is the second longest river in California, and its watershed within the Central Valley is one of the California's most productive agricultural areas. The river

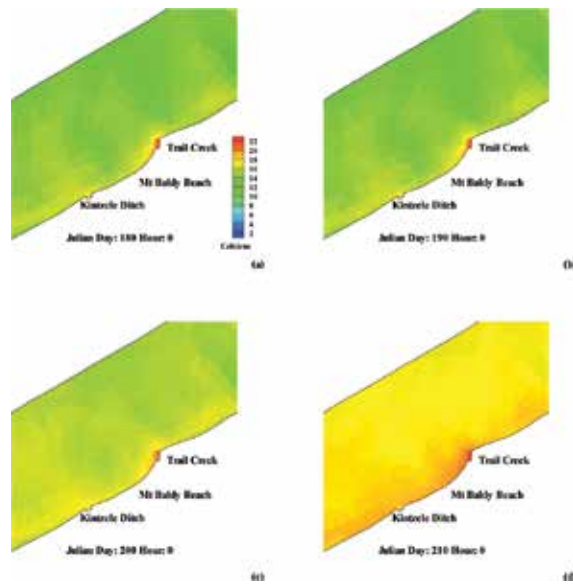


Figure 9. Spatial distribution of water temperature at 12:00 am on Julian day: (a) 180, (b) 190, (c) 200, and (d) 210.

originates mainly from snowmelt and runoff in the high Sierra Nevada, eventually converging with the Sacramento River in the Sacramento-San Joaquin Delta in Northern California. The SJR has experienced considerable low flow over the years, at times ceasing to flow completely. Chinook salmon was historically abundant in the SJR, but their populations have significantly decreased due to the insufficient flow. In order to restore and sustain salmon and other fish populations, the San Joaquin River Restoration Program (SJRRP) was established in 2006 to maintain continuous flow along the entire length of the river and improve its hydrodynamic conditions from Friant Dam to its confluence with the Merced River. Suitable hydrodynamic conditions, including flow velocity and water depth, are crucial for the safe passage of migrating salmon. Due to practical limitations, the flow has been rerouted along several alternative pathways specifically designed and created as part of the river restoration effort, modifying the traditional SJR channels. These alternatives were designed and compared to support the passage of fish by providing adequate hydrodynamic conditions throughout the river reach. The first objective of the research conducted for this case study was to model the stream conditions, including current velocity, depth, and WSE, for three alternatives proposed for the SJRRP given the same hydrologic/hydraulic boundary conditions. This part of hydrodynamic research has been done and published [28]. The second objective was to further investigate how the water quality at the upstream of the SJR affects the downstream. A 2D water depth-integrated water quality model was developed corresponding to the previous hydrodynamic model to simulate and predict the fate and transport of the contaminants in the upper SJR reach. The water quality model will provide a tool for the SJR restoration and management in the future.

4.2.2. Investigation domain and model mesh

The study area covered approximately 90 river kilometers from the SJR monitoring station near Dos Palos (SDP) to the SJR monitoring station at the Fremont Ford Bridge (FFB) near California Highway 140, which is located within the Middle San Joaquin-Lower Chowchilla

watershed. In this case study, alternative 3 was used for the water quality study. The water pathway is: Reach 4A—Eastside Bypass—Mariposa Bypass—Reach 4B2—Reach 5 [28].

The same finite element mesh employed in the hydrodynamic model with resolutions ranging from 0.5 to 50 m was used to delineate the complex boundaries of the SJR.

4.2.3. Data collection

Bathymetric data were collected during 2010 and 2011 by the US Bureau of Reclamation (USBR) using GPS and ADCP at a spatial interval of 6 m. The flow rate and WSE data (from January 1 to September 30 of 2011) used to verify and calibrate the model and as boundary conditions were obtained from the US Geological Survey (USGS), USBR, and the California Department of Water Resources (CADWR). The geographic boundary of the SJR was delineated using coordinates from Google Earth based on the WGS84 global reference system. The data collected from different coordinate systems were all converted and georeferenced using the same coordinate system and reference datum, namely the North American Vertical Datum NAVD 88 and California State Plane, Zone 3, North American horizontal Datum NAD 83. The water quality data are not available at this time.

4.2.4. Model setup

A vertically integrated hydrodynamic model has been employed using the finite element scheme RMA10 to simulate flow velocity, water depth, and WSE. The governing equations were Eqs. (5)–(8). Compared with the first case study, the Coriolis force and wind stress are insignificant and can thus be neglected for this small-scale river reach. For the initial conditions, the river was assumed to be at rest at the beginning and it took a considerable time (10 days) to reach the actual initial conditions. The boundary conditions included the upstream flow rates, the known downstream WSEs, no leakage across the surface and the bottom, a drag stress at the river bottom, no wind stress and zero pressure at the water surface.

4.2.5. Results and discussion

The hydrodynamic model has been calibrated using the 2011 discharge and WSE data set. The Manning roughness coefficient of the river reach was manually adjusted to calibrate the model using the RMSE (Eq. (23)). The optimum value of 0.035 of the coefficient led to the minimum RMSE.

The flow velocity and WSE obtained from the validated and calibrated model were then used to assess the habitat suitability of the SJR reach for the spring Chinook salmon. The detailed model calibration and engineering plan comparisons have been reported by Liu and Ramirez [28]. Due to the lack of observed water quality data, the developed water quality model was used to simulate a virtual scenario as follows: four chemical species, including NH_3 , NO_3 , Organic N, and Organic P, which are common in the SJR watershed, entered the SJR at the upstream entrance of the river reach (SDP). These contaminants transport to the downstream with water flow and also undergo their own deactivation. **Figure 10** shows the concentrations change with time during a 110-day period. The SDP curve represents the upstream boundary condition. EBM and FFB are the middle station and downstream station, respectively. The

modeling results indicate the similar transport patterns for all species with a time lag between the locations. Generally, it took about 20 days for a contaminant to transport from SDP to FFB for this case. Therefore, the model can also be used to effectively predict the downstream scenario once the upstream condition is known. **Figure 11** shows a spatial distribution of various parameters at some time (the 50th Julian day of 2011 in this example).

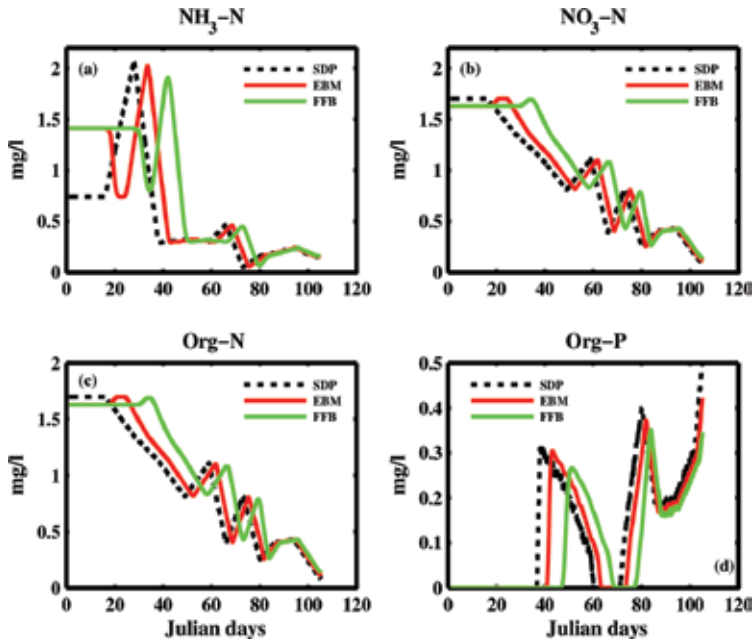


Figure 10. Calculated concentrations of: (a) NH₃-N, (b) NO₃-N, (c) organic N, and (d) organic P.

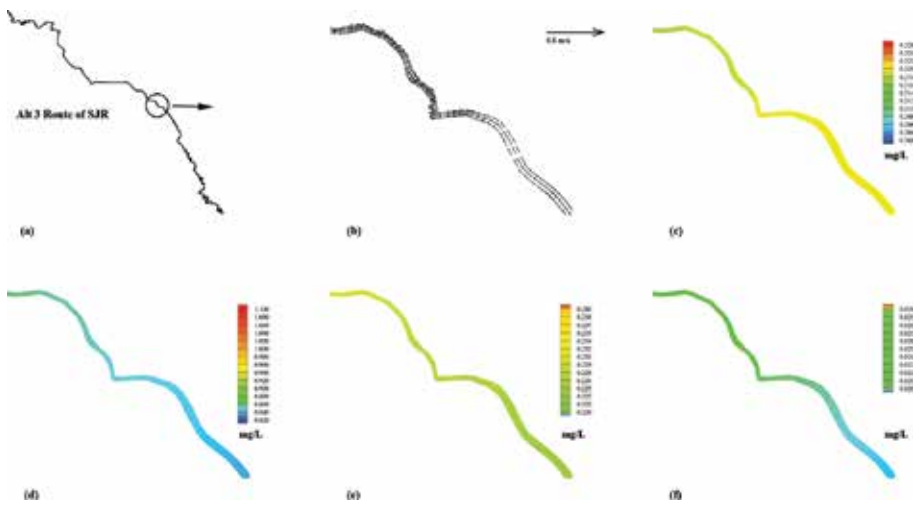


Figure 11. Scheme of (a) Alt3 route of SJR, spatial distributions of (b) velocity vector of Alt 3 of SJR, concentrations (contours) of: (c) NH₃-N, (d) NO₃-N, (e) organic N, and (f) organic P at Julian day 50, 2011.

5. Summary of hydrodynamic-water quality model applications

Based on the fundamental concepts, theories and principles, and the practical examples presented in the two case studies, the steps involved in developing and employing a hydrodynamic-water quality model to simulate or predict a surface water system can be summarized as follows:

1. Determine the modeling domain and identify the boundaries.
2. Develop an appropriate concept model. The dimensions, governing equations, and numerical methods (e.g., finite element method, FEM) are decided based on the goals to be achieved and the hydrodynamic characteristics of the target water body.
3. Create the grid or mesh and define the boundary conditions.
4. Collect data (bathymetry, flow rate, water surface elevation, concentrations of contaminants, etc.) required for the model input, verification, and calibration.
5. Run the model.
6. Calibrate the model using the observed data.
7. Apply the model to simulate a real world scenario or solve a practical problem.

Based on aforementioned theory and principles, a stratified 3D model was used to investigate the circulation and *E. coli* transport in the nearshore region of Lake Michigan. The modeling results show that stratified phenomenon exists in the near region, and a 3D model is necessary. A 2D depth-averaged water quality model was developed to estimate the fate and transport of four contaminants in the San Joaquin River (SJR) of California. These models can be effectively used for inland surface water restoration and management.

Author details

Lubo Liu

Address all correspondence to: llubo@csufresno.edu

Department of Civil and Geomatics Engineering, Lyles College of Engineering, California State University Fresno, USA

References

- [1] Stamou A, Polydera A, Papadonikolaki G, Martinez-Capel F, Munoz-Mas R, Papadaki C, Zogaris S, Bui MD, Rutschmann P, Dimitriou E. Determination of environmental flows in rivers using an integrated hydrological-hydrodynamic-habitat modelling approach. *Journal of Environmental Management*. 2018;**209**:273-285

- [2] Lee I, Hwang H, Lee J, Yu N, Yun J, Kim H. Modeling approach to evaluation of environmental impacts on river water quality: A case study with Galing River, Kuantan, Pahang, Malaysia. *Ecological Modelling*. 2017;**353**:167-173
- [3] Kim J, Lee T, Seo D. Algal bloom prediction of the lower Han River, Korea using the EFDC hydrodynamic and water quality model. *Ecological Modelling*. 2017;**366**:27-36
- [4] Shakibaeinia A, Kashyap S, Dibike YB, Prowse TD. An integrated numerical framework for water quality modelling in cold-region rivers: A case of the lower Athabasca River. *Science Total Environment*. 2016;**569-570**:634-646
- [5] Tang C, Yi Y, Yang Z, Zhang S, Liu H. Effects of ecological flow release patterns on water quality and ecological restoration of a large shallow lake. *Journal of Cleaner Production*. 2018;**174**:577-590
- [6] Khadr M, Elshemy M. Data-driven modeling for water quality prediction case study: The drains system associated with Manzala Lake, Egypt. *Ain Shams Engineering Journal*. 2017;**8**(4):549-557
- [7] Qi H, Lu J, Chen X, Sauvage S, Sanchez-Perez JM. Water age prediction and its potential impacts on water quality using a hydrodynamic model for Poyang Lake, China. *Environmental Science and Pollution Research International*. 2016;**23**(13):13327-13341
- [8] Liang S, Jia H, Xu C, Xu T, Melching C. A Bayesian approach for evaluation of the effect of water quality model parameter uncertainty on TMDLs: A case study of Miyun reservoir. *Science Total Environment*. 2016;**560-561**:44-54
- [9] Elshemy M, Khadr M, Atta Y, Ahmed A. Hydrodynamic and water quality modeling of Lake Manzala (Egypt) under data scarcity. *Environmental Earth Sciences*. 2016;**75**(19)
- [10] Donia N, Bahgat M. Water quality management for Lake Mariout. *Ain Shams Engineering Journal*. 2016;**7**(2):527-541
- [11] Xu C, Zhang J, Bi X, Xu Z, He Y, Gin KY. Developing an integrated 3D-hydrodynamic and emerging contaminant model for assessing water quality in a Yangtze estuary reservoir. *Chemosphere*. 2017;**188**:218-230
- [12] Alosairi Y, Pokavanich T, Alsulaiman N. Three-dimensional hydrodynamic modelling study of reverse estuarine circulation: Kuwait Bay. *Marine Pollution Bulletin*. 2018;**127**: 82-96
- [13] Silva Dos Santos E, Pinheiro Lopes PP, da Silva Pereira HH, de Oliveira Nascimento O, Rennie CD, da Silveira Lobo O'Reilly Sternberg L, and Cavalcanti da Cunha A, The impact of channel capture on estuarine hydro-morphodynamics and water quality in the Amazon delta. *Science Total Environment*, 2017;**624**:887-899
- [14] Mali M, Malcangio D, Dell' Anna MM, Damiani L, Mastrorilli P. Influence of hydrodynamic features in the transport and fate of hazard contaminants within touristic ports. Case study: Torre a Mare (Italy). *Heliyon*. 2018;**4**. DOI: 10.1016/j.heliyon.2017.e00494

- [15] Malcangio D, Petrillo AF. Modeling of brine outfall at the planning stage of desalination plants. *Desalination*. 2010;**254**(1–3):114-125
- [16] Ji ZG. *Hydrodynamics and Water Quality - Modeling Rivers, Lakes, and Estuaries*. 1st ed. Hoboken, New Jersey: John Wiley & Sons, Inc.; 2007. 676 p
- [17] Gill AE. *Atmosphere-Ocean Dynamics*. New York: Academic Press; 1982. 662 p
- [18] Cole TM, Buchak EM. CE_QUAL-W2: A Two-Dimensional, Laterally Averaged, Hydrodynamic and Water Quality Model, Version 2. Vicksburg, MS: Technical Report EI-95-X. US Army Corps of Engineers, Waterways Experiment Station; 1995
- [19] Ford DE, Johnson MC. An Assessment of Reservoir Mixing Processes. Vicksburg, MS: Technical report, E-86-7: US Army Engineer Waterways Experiment Station; 1986
- [20] Wu WM. *Computational River Dynamics*. London, UK: Taylor & Francis; 2008. 494 p
- [21] Liu L, Phanikumar MS, Molloy SL, Whitman RL, Shiverly DA, Nevers MB, Schwab DJ, Rose JB. Modeling the transport and inactivation of *E. coli* and enterococci in the near-shore region of Lake Michigan. *Environmental Science & Technology*. 2006;**40**:5022-5028
- [22] Smagorinsky J. General circulation experiments with the primitive equations I. The basic experiment. *Monthly Weather Review*. 1963;**91**:99-164
- [23] King IP. User Guide of RMA10-a Finite Element Model for Three-Dimensional Density Stratified Flow; User Guide of RMA11-a three Dimensional Finite Element Model for Water Quality in Estuaries and Stream. 2004
- [24] Phillips NA. A coordinate system having some special advantage for numerical forecasting. *Journal of Meteorology*. 1957;**14**:184-185
- [25] Mellor GL, Yamada T. Development of a turbulence closure model for geophysical fluid problems. *Reviews of Geophysics and Space Physics*. 1982;**20**(4):851-875
- [26] Liu L, Fu XD, Wang GQ. Simulation of wind-driven circulation and temperature in the near-shore region of southern Lake Michigan by using a channelized model. *Journal of Hydrodynamics*. 2013;**25**(1):99-111
- [27] Xia XS, Miller DH. The stratification analysis of sediment data for Lake Michigan. *Journal of Data Science*. 2011;**9**:181-203
- [28] Liu L, Ramirez J. Assessment of spring Chinook salmon habitat suitability in the San Joaquin River using a 2-D depth-averaged model. *International Journal of Water Sciences*. 2013. DOI: 10.5772/57437

Optical Methods Applied to Hydrodynamics of Cohesive Sediments

Juan Antonio Garcia Aragon,
Salinas Tapia Humberto, Diaz Palomarez Victor and
Klever Izquierdo Ayala

Additional information is available at the end of the chapter

<http://dx.doi.org/10.5772/intechopen.72347>

Abstract

Suspended sediment transport in large rivers is constituted mainly by cohesive sediments, which form aggregates or flocs with primary particles less than 65 μm . The removal of cohesive sediments in aquaculture tanks is a difficult problem. Due to its size, density, and shape, the hydrodynamic behavior of flocs is very different from that of non-cohesive sediments as they depend on the interaction with the water column. This chapter describes the experimental results obtained in sedimentation tanks, reduced models of aquaculture recirculation tanks, and a rotating circular flume with Plexiglas walls, in which optical methods were used to determine flocs' characteristics. These methods include particle tracking velocimetry (PTV) and digital holography for particle image velocimetry (DHPIV). Fractal models for floc density were successfully developed and validated with PTV experimental results in an aquaculture recirculation tank. Also, a model for the settling velocity of the flocs was validated using a permeable drag coefficient definition. Suspended sediments from Mexico's two largest rivers, Usumacinta and Grijalva, with a mean flow rate near mouth of 1700 and 650 m^3/s , respectively, were analyzed in a rotating circular flume. The shear velocity obtained in the field was reproduced in the circular flume and size and shape of flocs were obtained. This allowed to reproduce suspended sediment concentration profiles of rivers. DHPIV techniques were developed in order to obtain the actual size of the flocs based on Fresnel approximation for the reconstruction of holographic images.

Keywords: floc, settling velocity, suspended sediments, fractal dimension, PTV, DHPIV

1. Introduction

Hydrodynamic behavior of cohesive sediments is important in many fields of engineering. A large part of the suspended sediment charge in large rivers is constituted by cohesive sediments

as shown in the Amazon River sampling of suspended sediments [1]. A characteristic of cohesive sediments is to form aggregates (flocs) that behave in a very different way than non-cohesive sediments. Measuring *in-situ* flocs settling velocities in rivers is not possible with conventional sediment sampling instruments. Recently, *in-situ* optical instruments are being used for floc size measurement, particularly in the field of oceanography [2, 3]. Those instruments are very expensive because they use laser illumination and are not used in common river engineering practice. In this chapter, a method based on suspended concentration sampling and laboratory particle size analysis in a rotating annular flume is used to obtain flocs size, and with an appropriate settling velocity model deduce the settling velocity to be used in the Rouse equation. The method is validated with sediments from Usumacinta and Grijalva rivers, the two major rivers in México, whose basins are located in the states of Chiapas and Tabasco near the Guatemalan border.

The settling velocity of cohesive sediments is an important design parameter in aquatic environments such as water treatment plants, storm water ponds, sediment filling in lakes, sedimentation in estuaries, dredging in rivers, and sediment removal in aquaculture devices especially when shortage of water is a concern [4]. The reuse of water is the main characteristic of the latter systems.

The efficient removal of solids is a main concern in these systems because of the accumulation of non-used food and fish excreta. These solids are generally less than 65 μm in diameter and behave as cohesive sediments [5]. These sediments form flocs or aggregates, made of water, inorganic particles, and organic particles [6–8]. To obtain adequate settling models for these particles is an active field of research [9]. Some researchers include variable fractal dimension functions that depend on a characteristic size of flocs that is difficult to obtain over a large population of flocs [10]. Other authors use geometrical parameters of flocs like floc perimeter, which is not easy to measure in engineering practice [11, 12]. The flocs' settling velocity model proposed in this study uses parameters that are possible to average, using optical methods with some floc samples.

The tanks most widely used are circular [13, 14]. Water is supplied in these tanks by means of diffusers at the walls. In this project, a small scale circular water recirculation tank was used in order to study the solids behavior in the tank. There is a central settling device in order to remove the solids (**Figure 1**). The settling device functions according to the hydrocyclons principle [15].

Two optical techniques were used in this work, Particle Image Velocimetry (PIV) and Particle Tracking Velocimetry (PTV), to measure fluid and particle velocities, respectively. Polyamide tracers 25 μm in diameter were used to obtain fluid velocities using PIV, and flocs were tracked as particles in the PTV technique. PTV also allowed us to measure particle size and shape. Digital holography for particle image velocimetry (DHPIV) has also been used to determine the size and shape of flocs considering their volumetric nature.

The attempts to model settling velocity as a function of floc size, shape, and density demonstrated that density varies with floc size. Later work demonstrated that floc density depends on the fractal nature of flocs [16]. Recently, the effect of shear rate on floc density was demonstrated [11].

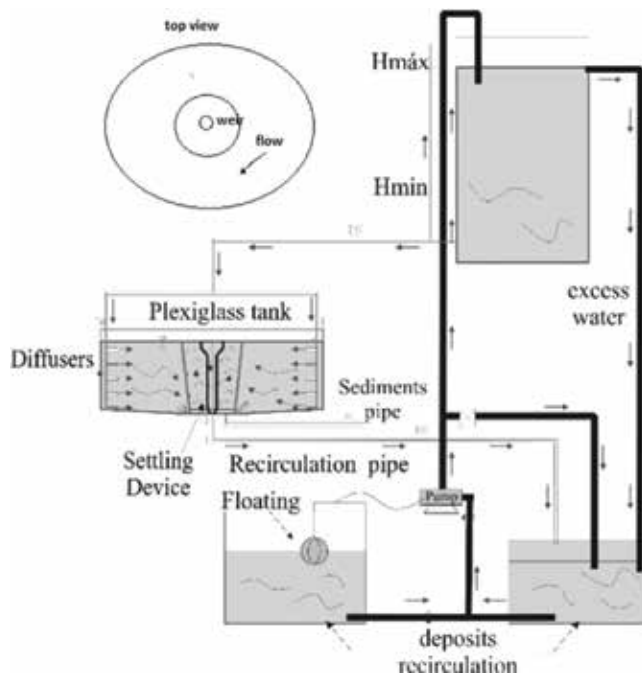


Figure 1. Reduced model of an aquaculture recirculation tank.

In this study, the results were used to calibrate settling velocity models using fractal theory and by including an adequate definition of the drag coefficient for permeable flocs. The proposed model is shown to provide reproducible results if a calibration of the parameters in the density vs. diameter model is properly done.

Suspended sediment samples obtained near the mouth of the Grijalva and Usumacinta rivers were analyzed in a rotating annular flume using PTV. It was possible to obtain appropriate values of the Rouse parameter Z_R , which was shown to be difficult to obtain with classical granulometric and Coulter counter methods used in river studies [1].

2. Methods

2.1. Experiments using PTV and sediments coming from aquaculture recirculation tanks

Initial experiments were performed with fish food in order to have a better control of primary particles. The sediments were sieved and only those passing sieve 200 (0.075 mm), with a mean density of 1430 kg/m^3 were used. A Plexiglas settling column was realized in order to allow the use of PIV and PTV optical methods. The set up consisted of a rectangular tank of cross section $15.5 \times 15.5 \text{ cm}$ and 100 cm height. A laser sheet was introduced from above using a double

pulsed Nd:Yag laser (15 mJ), high-speed CCD cameras JAI (250 fps and resolution and 1600×1400 pixels) were mounted laterally to the column and synchronized by means of a NI-PCIE-1430 card with laser pulses. Both cameras were equipped with 50 mm NIKKON lenses. The cohesive sediments were introduced manually and images were captured at the 30, 60, and 90 cm marks from the bottom of the tank. The resulting frequency histograms are presented in the following of the paper. For the processing of the images, the software used was PTV-SED v2.1, developed at CIRA to analyze the fall velocity of sedimentary particles in two-phase flows. PTV operation comprises of two sequential procedures. The first procedure implies improving image quality through spatial filtering. The second procedure implies detecting particles in each pulse following the five stages proposed: (i) identify maximum and minimum intensity (black or white) over the particle image to determine its size; (ii) from the intensity of pixels of the evaluated particle, a circular area is formed which can be used to determine the cross-sectional particle area (A), and then the equivalent diameter (d) can be estimated using $d = 2\sqrt{A/\pi}$; (iii) from the cross-sectional particle area (A) and pixel intensity, the coordinates (x, y) of the drop centroid are determined; (iv) pairs of double-pulsed particle are identified and the distance separating their centroids ($\Delta x, \Delta y$) is determined; and (v) Particle velocity (v_x, v_y) is obtained as follows:

$$(v_x, v_y) = \left(\frac{\Delta x}{\Delta t}, \frac{\Delta y}{\Delta t} \right) \quad (1)$$

Then a small scale water recirculation tank made of Plexiglas 35 cm in depth and with 1.03 m diameter was used in the experiments with the same cohesive sediments from fish food. A complete system for water recirculation (**Figure 1**) was implemented. Water is obtained by a high rise tank with a constant water level in order to supply a constant flow rate by using gravity. Diffusers at different levels on the tank wall control the flow rate and tank water velocity, together with the generation of the circular flow. A settling device in the center of the tank allows solids removal.

Using this recirculation tank settling velocities and sizes of sediments were obtained from commonly used fish food and excreta coming from experimental station El Zarco, which cultivates trout. It is owned by Semarnap, the Mexican state agency of environment, natural resources, and fisheries, and is located at 2800 masl in Salazar Estado de México, México.

The next stage consisted to analyze suspended cohesive sediments coming from the Usumacinta and Grijalva rivers in México. In order to reproduce hydrodynamic conditions prevailing in the river and to analyze the flocculation process during long range experiments, an annular rotating flume, 1.3 m diameter and 15×15 cm flume cross section made of Plexiglas, was used (**Figure 2**). The cohesive sediments were analyzed using PTV, during 1.5 h. long experiments and images were taken every 15 min. From this experiment floc sizes and settling velocities were obtained.

2.2. Theoretical settling velocity models

The greatest challenge in the proposal of a settling velocity model for flocs is the adequate definition of their density. Many models have been formulated for floc density [17], in this research the adopted model is the one proposed by Kranenburg [18], as shown in Eq. (2)

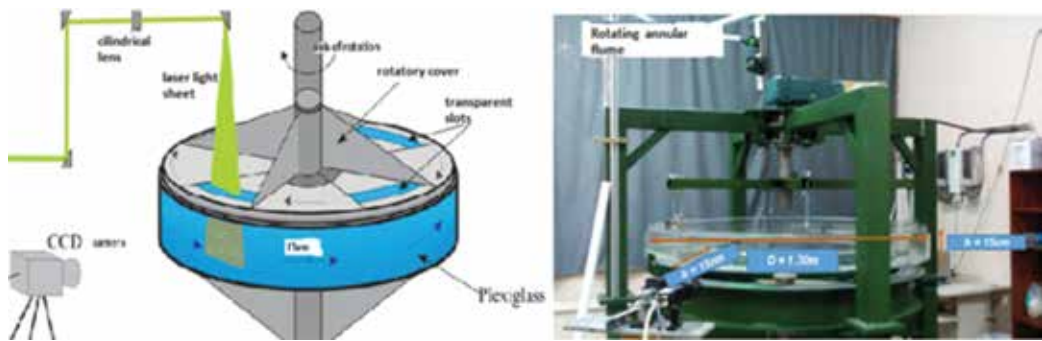


Figure 2. Rotating annular flume and PTV set up.

$$\rho_f - \rho_w = (\rho_p - \rho_w) \left(\frac{D}{d}\right)^{F-3} \quad (2)$$

where ρ_f , ρ_w , and ρ_p are densities of floc, water, and primary particles, respectively, D is the floc diameter and d is the primary particles diameter. F is the fractal dimension and the model assumes that the floc is constituted of spherical primary particles of equal diameter. The model can be used for non-spherical particles with equivalent diameters.

A balance of drag forces and gravitational forces gives Eq. (3)

$$W_s^2 = \frac{4(\rho_f - \rho_w)gD}{3C_{Df}\rho_w} \quad (3)$$

where W_s is the floc settling velocity and C_{Df} is the permeable particle drag coefficient. Using Eqs. (2) and (3), the following relationship for the settling velocity is obtained

$$W_s = \sqrt{\frac{4(S-1)g(D)^{F-2}}{3C_{Df}(d)^{F-3}}} \quad (4)$$

with S is the primary particles relative density.

Using Particle Tracking Velocimetry methods (PTV), Garcia Aragon et al. [19] have shown that a useful relationship for the drag coefficient of a permeable floc has the following form:

$$C_{Df} = \frac{15}{R_{ep}^n} \quad (5)$$

where the coefficient n depends on the kind of floc and varies, according to a comparison of results of different authors [20], between 1.1 and 1.25. R_{ep} is the particle Reynolds number defined as $R_{ep} = W_s D / \nu$ where ν is the kinematic viscosity of the fluid.

Replacing the relationship from Eq. (5) in Eq. (4), the following relationship for the settling velocity is obtained:

$$W_s = \frac{[13.08(S-1)]^{\frac{1}{2-n}} D^{\frac{F+n-2}{2-n}}}{15^{\frac{1}{2-n}} \sqrt{2-n} d^{\frac{F-3}{2-n}}} \quad (6)$$

where W_s is in m/s and D and d in m.

As the fractal dimension changes with floc diameter, in this paper, we used a relationship proposed by Garcia-Aragon et al. [16] that has a form similar to the following:

$$F = 3 - \alpha \left[\frac{D}{d} \right]^\beta \quad (7)$$

where α and β are constants that depend on the kind of cohesive sediment. Maggi et al. [21] used flocculated kaolinite minerals in experiments in a settling column and found that the exponent β varies between -0.092 and -0.112 .

2.3. Application to suspended load estimation in large rivers

Authors working with the Mississippi river sediment transport Colby [22, 23], realized that the predicted Rouse number was not equal to the measured Rouse number in a series of sampled vertical profiles of the Mississippi. Also, researchers working in the three Gorges Reservoir in the Yangtze River show that settling velocities calculated with diameters obtained from particle size analyzers do not reproduce observed settling velocities, which indicate the existence of flocculation [24]. The formation of flocs in large rivers is the reason why Rouse equation cannot be used with particle sizes from classical granulometric measurements in conjunction with non-cohesive settling velocity equations. Recently, researchers working in the Amazon River and tributaries made similar observations [1]. Their conclusion was that granulometric measurements performed did not represent the real particle size because cohesive sediments agglomerate to form flocs [5, 6, 9] and after sampling, these flocs are destroyed and could not be measured appropriately in laboratory. On a related note, other researchers have shown that particle sizes in the Amazon River are lower than $70 \mu\text{m}$ [25, 26], which are in the size range of cohesive sediments.

To estimate the suspended sediment profile in stationary flows, the following Rouse equation is generally accepted [27]

$$\left(\frac{C(y)}{C(a)} \right) = \left(\frac{H-y}{y} \cdot \frac{a}{H-a} \right)^{Z_R} \quad (8)$$

where the Rouse parameter is $Z_R = W_s/Ku^*$, $C(y)$ is the suspended sediment concentration at height y above bed, H is flow depth, a is a reference depth above bed, and K is Von-Karman's constant that for low sediment concentration is equal to 0.41.

In this project, Eq. (6) is used to estimate the settling velocity W_s , in conjunction with the Rouse Eq. (8) for the evaluation of the suspended sediment profiles in the Grijalva and Usumacinta rivers, the two largest rivers in Mexico.

2.4. Application of digital holography for PIV (DHPIV) for cohesive sediments characterization

Even if there are enormous advances in PIV and PTV techniques, there are shortcomings for 2D applications. The latter is observed in some physical phenomena, for example for the volume determination of a floc, which is only possible with 3D optical techniques. One of these techniques is digital holography for particle image velocimetry (DHPIV). This technique has been shown appropriate, for size distribution, volume determination, and particle velocity in fluids [30].

The DH method consists of specific steps as shown in **Figure 3**. Most experiments in scientific literature record a hologram following the so called in line system [28–30]. In this configuration, a coherent and collimated laser beam is sent, this is divided in two beams, one is directed toward the particles suspended in the fluid and is called the reference beam, while the dispersed light is called object beam. The two beams interfere to form a hologram which is recorded by the CCD digital camera (**Figure 3**). A typical particle hologram contains a succession of circular concentric interference strips which define the object in three dimensions.

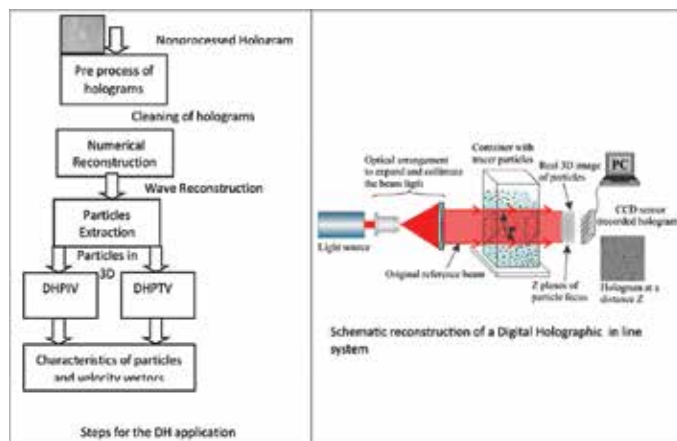


Figure 3. In line digital holographic system.

Green light laser diode	532 nm wave length, 50 mW power
Microscope objective	40×
Pinhole to expand and collimate beam	10 and 5 μm
Lens to collimate the wave front	Focal distance $f = 75 \text{ mm}$, 7 cm diameter
Polarizing filters	
Glass container	5 × 5 × 10 cm, glass width 3 mm
Digital camera Lumenera	100 fps, pixel size $D_x = D_y = 5.2 \mu\text{m}$, 1200 × 1400 px
Sample of fluid to analyze	

Table 1. Physical components of digital holographic system.

For application and calibration of a DH optical system, cohesive sediments from a waste water plant were used. A coagulant was added in order to allow floc formation in the rotating annular flume.

The physical components of the digital holographic system used are described in **Table 1**.

Holographic images acquired and improved are reconstructed numerically in order to obtain 3D characteristics of flocs. The Fresnel method was used for image reconstruction [31].

3. Results

3.1. Experiments with cohesive sediments coming from food for fish

A first analysis of particles coming from fish food, using a Coulter counter analyzer, which destroys flocs, is shown below. The pellets were previously sieved and only those passing sieve 200 (0.075 mm) were conserved. It is observed (see **Figure 4**) that an average diameter of primary particles is 28 μm .

Using the same fish food sediments optical methods were developed in a sedimentation tank. The following settling velocities were obtained at 60 cm from the top of the sedimentation tank by using PTV. It is observed in **Table 2** that the settling velocity increases until a certain value ($D = 200 \mu\text{m}$) and then decreases for larger floc diameters. This behavior is not reflected in classical settling velocity models.

3.2. Experiments with real flocs from an aquaculture recirculation tank

Next long-term experiments were performed in a reduced model of an aquaculture recirculation tank (**Figure 1**), flocs diameters and the corresponding settling velocities were measured for different times using PTV. The sediments used were real flocs coming from a large aquaculture recirculation tank (El Zarco). Some selected samples of the experiments were analyzed by Transmission Electron Microscopy (TEM) (**Figure 5**), at the beginning of the experiment ($t = 0$),

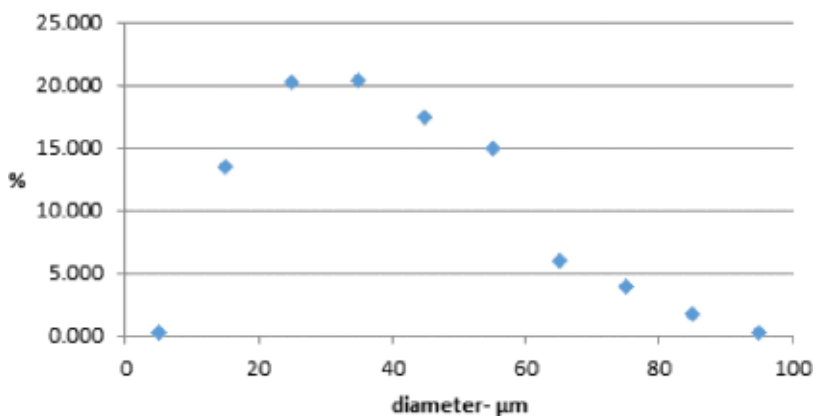


Figure 4. Fish food particle sizes from coulter counter (LS 100Q) analysis.

Floc size	75	100	150	200	250	300	350	400
W_s (cm/s)	0.51	0.62	0.68	0.8	0.79	0.74	0.66	0.54

Table 2. Average settling velocities for fish food in a sedimentation tank (cm/s).

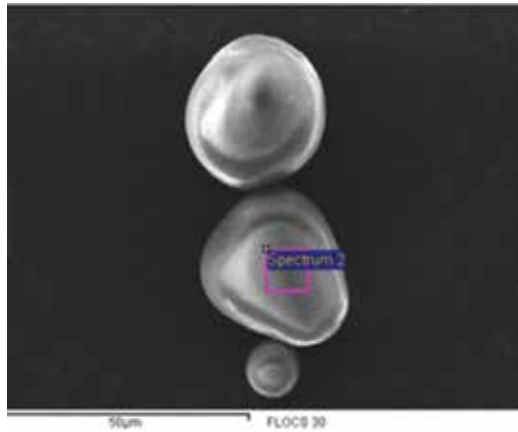


Figure 5. Representative values of fish food primary particles obtained by TEM.

at 15 min ($t = 15$), at 45 min ($t = 45$) and at 1 h ($t = 60$). An average diameter of primary particles of 28 μm was confirmed. Thus, this result was used in the statistical analysis.

In the experiments using the reduced model of an aquaculture recirculation tank, Eqs. (6) and (7) were used for the statistical analysis in order to define the parameters n , α and β . These parameters were defined according to the best correlation coefficient in the relationships W_s vs. D and F vs. D/d . **Figure 6** shows the best fit of F vs. D/d according to Eq. (7). **Table 3** shows the values of α and β obtained at each time.

The average value for the coefficient α was 0.077 and the average value of the coefficient β was 0.726. The latter exponent value is larger than the one obtained by [22] for a similar model, which can be explained with the structure of aquaculture flocs compared to Kaolinite, which is completely different.

Figure 7a–d shows the best fit relationship between W_s and D using the F vs. D/d relationship previously obtained. The resulting n values at different time steps are specified in **Table 4**.

Table 4 shows that the value of n increases as the time of the experiment increases. This observation can be related to the increasing loss of density of the floc. As time increases, the flocs are increasing their volume absorbing water. The latter has two implications; the drag coefficient decreases because the floc becomes more porous and its density decreases.

An interesting feature observed in **Figure 7a–d** is that the settling velocity of the flocs increases for values of floc diameter up to 600 μm and then decreases as floc diameter continues to increase. The settling velocity model proposed in this research is able to reproduce this behavior.

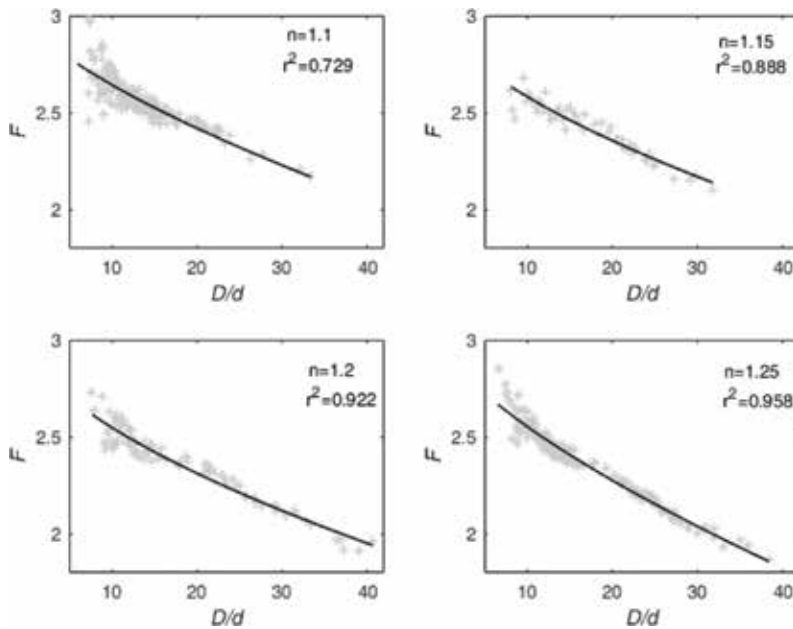


Figure 6. Fractal dimension vs. D/d : (a) at time 0 (upper left), (b) at time 15 min (upper right), (c) at time 45 min (lower left), and (d) at time 60 min (lower right).

Time (min)	α	β
0	0.070	0.703
15	0.049	0.863
45	0.111	0.609
60	0.077	0.727

Table 3. Best fit coefficients for the relationship F vs. D .

This behavior has been shown to occur in nature for different kind of flocs, coming from estuaries, waste water treatment plants, and rivers [10, 19]. Most of the settling velocity models for cohesive sediments show an increase of settling velocity for all diameters which is not observed in this research. The larger flocs are formed after a long experimental period. In **Figure 7a** and **b**, there are few flocs larger than 600 μm , which is not the case for experimental periods of 45 and 60 min (**Figure 7c** and **d**). The practical implication of this phenomenon for aquaculture recirculation tanks is that residence times should not be very long because the larger flocs formed are even more difficult to settle down.

3.3. Experiments with suspended cohesive sediments of Grijalva and Usumacinta rivers

A sampling of suspended cohesive sediments in the Grijalva and Usumacinta rivers was done during high river level on the month of December 2016. The sampling location for the Grijalva

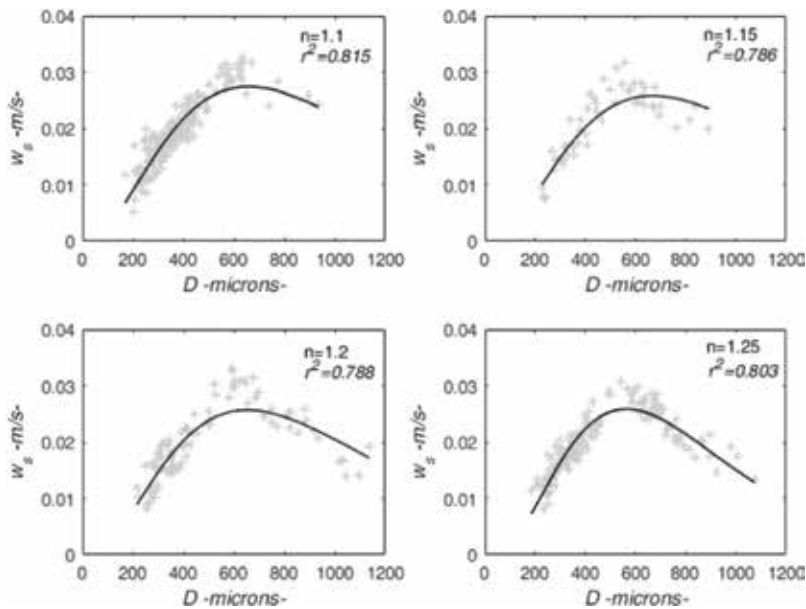


Figure 7. Settling velocity vs. D : (a) at time 0 (upper left), (b) at time 15 min (upper right), (c) at time 45 min (lower left), and (d) at time 60 min (lower right).

Time (min)	n
0	1.1
15	1.15
45	1.2
60	1.25

Table 4. Values of n for best fit relationship between W_s vs. D .

was located before the junction with the Usumacinta, and in the Usumacinta, it was located 20 km upstream of the junction with the Grijalva. Samples were obtained at three vertical water columns in each cross section. For the Grijalva River, the samples were obtained at levels varying from 0.5 to 11 m (maximum water depth) each 1 m. At the Usumacinta River, samples were obtained at levels varying from 0.5 to 17 m (maximum water depth) each 1 m. **Figures 8 and 9** show the suspended sediment concentration profiles for the Grijalva and Usumacinta Rivers, respectively. In these figures, the vertical axis refers to the level z adimensionized with the flow depth H , while the horizontal axis refers to the ratio of the concentration C to a reference concentration C_a .

An average value of Rouse parameter $Z_R = 0.214$ was obtained in the Grijalva River, which is representative of a small increase of suspended sediment charge near the bottom.

An average value of $Z_R = 0.069$ was obtained in the Usumacinta river. This value is representative of near constant suspended sediment charge in the water column.

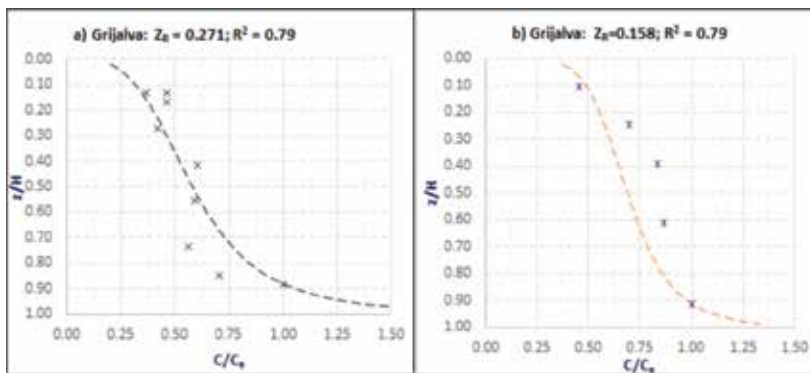


Figure 8. Suspended sediment concentration profiles for the Grijalva River. (a) 55 m from left bank and (b) 90 m from left bank.

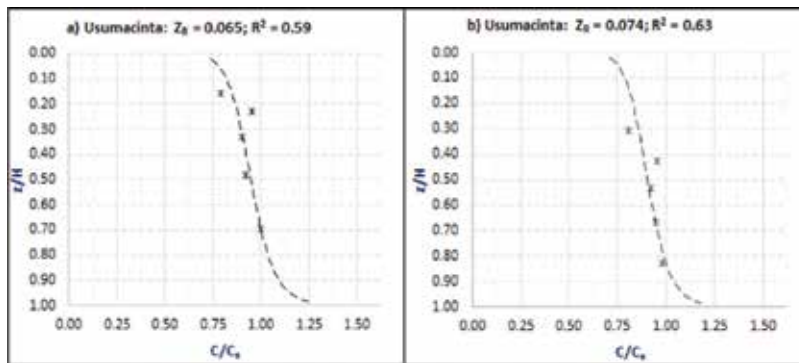


Figure 9. Suspended sediment concentration profiles for Usumacinta river. (a) 25 m from left bank and (b) 140 m from left bank.

Experiments in the rotating annular flume using 50 L samples for the Grijalva and Usumacinta rivers were performed at shear rates similar to those encountered in the field. **Table 5** shows the values of shear velocity (u_*) obtained in the sampling stations of the Grijalva (width 180 m) and Usumacinta (width of 340 m) rivers. The value of u_* was obtained by the horizontal u' and vertical fluctuating velocities w' ($u_*^2 = \overline{u'w'}$), where the over bar indicates an average over the water depth. The velocities were measured the same day of suspended sediment sampling with an Acoustic Doppler Current profiler (ADCP).

Images of flocs after experimental runs of 1.5 h in the Grijalva river samples and 3.5 h in the Usumacinta river samples, in the annular flume using PTV, gave us an average size of flocs of 307 μm in the Grijalva and 209 μm in the Usumacinta. **Table 6** shows the statistical values of flocs obtained in large runs at a shear velocity $u_* = 0.070$ m/s (the average value in the Usumacinta river see **Table 5**) and **Table 7** at $u_* = 0.043$ m/s (the average value at the Grijalva river, see **Table 5**).

Also, microscopic images of some representative flocs were obtained with 40 \times magnification. An average value of primary particle, after a statistical analysis of 50 flocs images for each

River	Distance from left bank (m)	u_* (m/s)
Grijalva	55	0.048
	90	0.045
	195	0.036
Usumacinta	25	0.064
	140	0.082
	210	0.065

Table 5. Shear velocity in Usumacinta and Grijalva rivers.

Time (min)	D (μm)	Number of data
5	217	33,200
20	188	17,254
50	172	21,542
120	164	12,232
150	242	32,560
180	247	25,441
210	232	23,450
Mean	209	

Table 6. Average floc size at the Usumacinta River from PTV experiments in the rotating annular flume.

Time (min)	D (μm)	Number of data
0	306	33,434
5	308	25,550
20	313	22,652
50	311	21,321
85	297	23,460
Mean	307	

Table 7. Average floc size at the Grijalva River from PTV experiments in the rotating annular flume.

river, gave an estimated value of 1.2 μm for the Grijalva river and 3.8 μm for the Usumacinta. Two representative images are shown in **Figures 10** and **11**.

When Eq. (6) is used along with the already found average values of D and d, the values of settling velocity are obtained for different floc sizes (**Table 8**) using Eq. (7), with values of $\alpha = 0.07$ and $\beta = 0.72$. The values of S were 1.29 for the Usumacinta river and 1.55 for the Grijalva river. Different values of n (**Table 8**) were used to show the sensitivity of the model to this compaction index.

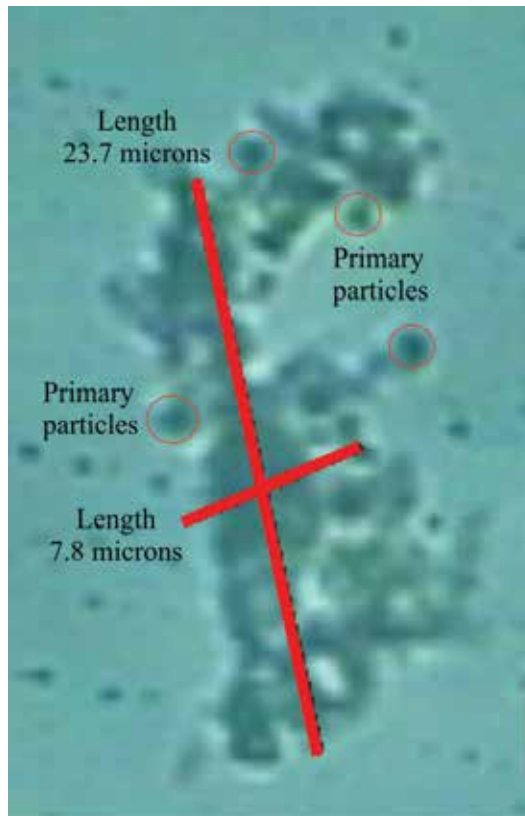


Figure 10. Primary particles and flocs representative of the Grijalva river.

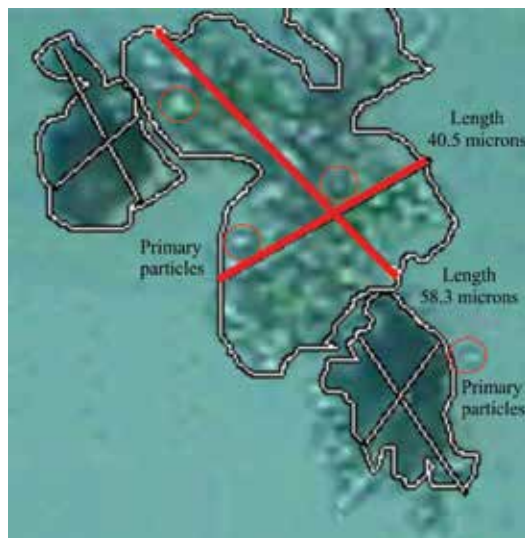


Figure 11. Primary particles and flocs representative of the Usumacinta river.

Table 8 shows that the best estimation of Z_R for the Usumacinta river is obtained with $n = 1.1$ because the average measured Z_R (see **Figure 8**) was $Z_R = 0.069$. Similarly, the best estimation of Z_R for the Grijalva river is also obtained with $n = 1.1$ because the average measured Z_R (see **Figure 9**) was $Z_R = 0.214$. The larger concentrations near the bottom for the Grijalva river are explained by the larger size of flocs in this river ($307 \mu\text{m}$ compared to $209 \mu\text{m}$ for the Usumacinta).

These results indicate that flocs of both rivers are strong flocs (low values of n), which is logical because shear rates at the Usumacinta and Grijalva rivers are high (for comparison u^* at Amazon River varies between 0.07 and 0.1 [1]). It is also observed that the value of Z_R in the Usumacinta river is more sensitive to changes in the value of n . It was observed that for large depths it is more difficult to define the n value as it can change even in the same cross section of the river at different levels.

3.4. Experiments using digital holography for PIV

Figure 12 shows the hologram reconstruction of a spherical particle of $50 \mu\text{m}$. **Figure 12a** shows the particle's hologram already filtered, where the different patterns of diffraction are observed; **Figure 12b** provides greater detail. The relative intensity profile (I/I_{max}) vs. reconstruction distance (z) is shown in **Figure 12c**. The maximum intensity is shown where the particle is in focus.

Figure 13a shows the digital hologram of flocs, while **Figure 13b** shows a preprocess in order to avoid noise in the hologram. Rings of interference are observed in both figures, which define the 3D characteristics of the flocs. **Figure 13c** shows the reconstruction of the binary image. This image only shows the particles that are in the best focus, i.e., where the shape of the particle is clearly defined. In order to find the position in the plane, the diameter, and shape of

n	Ws (mm/s)		Z_R	
	Usumacinta	Grijalva	Usumacinta	Grijalva
1.1	0.19	3.84	0.07	0.223
1.15	0.16	3.87	0.05	0.225
1.2	0.13	3.91	0.04	0.227
1.25	0.10	3.95	0.03	0.229

Table 8. Estimated values of W_s and corresponding values of Z_R .

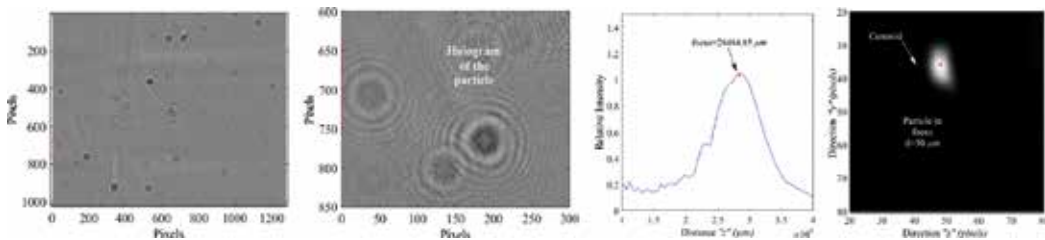


Figure 12. Results of a reconstruction of hologram process. (a) Originally filtered hologram; (b) one particle hologram; (c) relative intensity profile, and (d) reconstructed particle.

the particle, the PTV algorithm for non-spherical particles was applied. **Figure 13d** shows particles pair detection and its centroid, which allows us to determine particles' velocity for a sequence of holograms.

A settling column was used in order to observe the hologram evolution over time. Almost 100 holograms were processed each recording time. The times recorded were $t = 0, 10, 20, 30, 45,$ and 60 min. **Figure 14a** shows particles distribution for holograms at time $t = 0$, and it can be observed that maximum size is $160 \mu\text{m}$, with a mean diameter of $70 \mu\text{m}$.

Figure 14c shows the distribution of particles at time 30 min, where an increase in size of flocs is observed attaining a maximum of $180 \mu\text{m}$ and a mean value of $80 \mu\text{m}$. It is also observed that the shape of the distribution is log-normal, similar to theory. **Figure 14d** shows clearly a non-uniform distribution of particles in a hologram.

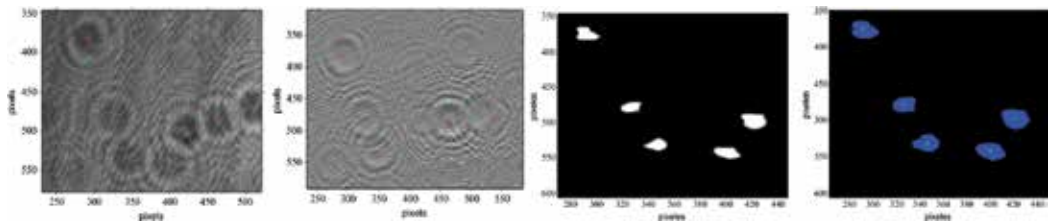


Figure 13. Results of analysis of a digital hologram. (a) Original digital hologram; (b) processed digital hologram; (c) reconstructed hologram, and (d) size and shape of detected particles.

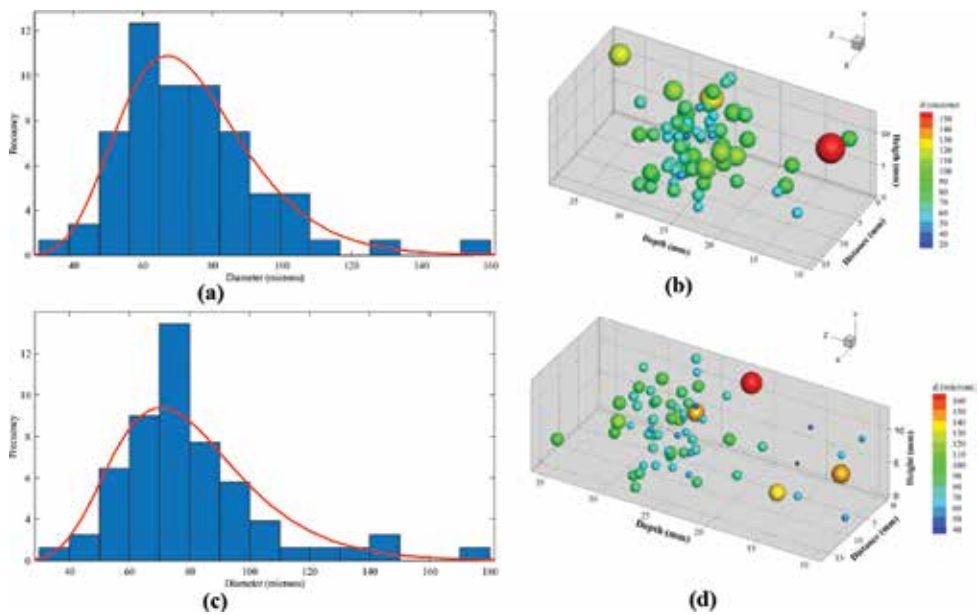


Figure 14. Characteristics of flocs in settling column (a) frequency distribution of sizes at $t = 0$ min; (b) spatial distribution of flocs at $t = 0$ min; (c) frequency distribution of sizes $t = 30$ min; (d) spatial distribution of flocs at $t = 30$ min.

4. Conclusions

A model to estimate the floc settling velocity was calibrated for flocs obtained from aquaculture recirculation tanks that cultivate trout. The model was able to reproduce the values of settling velocity which varies between 0.01 and 0.025 m/s. For all the recording times analyzed there is a maximum settling velocity for flocs of diameter of 600 μm .

The representative values of the parameters used to determine fractal dimension are proposed in this research according to the experimental results. These values depend on floc density and vary with experimental time as flocs become more porous. The values found in this research apply to flocs coming from trout cultures in high level locations, i.e., 2800 masl.

The practical findings for aquaculture recirculation tanks design is that residence times should be short in order to minimize the presence of very large flocs. Middle size flocs settle faster. In designing the central settling device, which functions according to the hydrocyclons principle, the up flow velocity should be less than 0.01 m/s in order to diminish the flow of sediments toward the recirculation deposit.

A method to obtain the suspended sediment concentration profiles for rivers with mainly cohesive sediments was presented. It is necessary to take some representative samples and using a rotating annular flume defines a steady state of flocculation after long-term runs. The most suitable method to analyze size and settling velocity of flocs are optical methods, PTV and microscopy. This research shows that the settling velocity can be accurately calculated with Eq. (6) in order to obtain an appropriate estimation of the Rouse number Z_R . This allows us to properly determine the suspended sediment concentration profiles in rivers carrying a large amount of cohesive sediments.

Non-intrusive optical techniques are a suitable tool to characterize cohesive sediments, because they do not destroy flocs and allow for microscopic analysis. More advanced optical methods, like DHPIV, are showing good results for floc size and shape determination, thus in the future they will be the best method for cohesive sediment analysis.

Author details

Juan Antonio Garcia Aragon*, Salinas Tapia Humberto, Diaz Palomarez Victor and Klever Izquierdo Ayala

*Address all correspondence to: jagarciaa@uaemex.mx

CIRA-Faculty of Engineering, Universidad Autónoma del Estado de México, Toluca, Mexico

References

- [1] Bouchez J, Metivier F, Lupker M, Maurice L, Perez M, Gaillardet J, France-Lanord C. Prediction of depth-integrated fluxes of suspended sediment in the Amazon River: Particle aggregation as a complicating factor. *Hydrological Processes*. 2011;25:778-794

- [2] Mikkelsen OA, Milligan T, Hill P, Moffatt D. INSSECT—An instrumented platform for investigating floc properties close to the seabed. *Limnology and Oceanography: Methods*. 2004;**2**:226-236
- [3] Nimmo Smith WAM, Atsavapraneep P, Katz, Osborn TR. PIV measurements in the bottom boundary layer of the coastal ocean. *Experiments in Fluids*. 2002;**33**:962-971
- [4] Wheaton FW. *Aquaculture Engineering*. New York: Wiley-Interscience; 1977. p. 708
- [5] Droppo IG. Rethinking what constitutes suspended sediment. *Hydrological Processes*. 2001;**14**:653-667
- [6] Droppo IG, Ongley ED. Flocculation of suspended sediment in rivers of south-eastern Canada. *Water Research*. 1994;**28**:1799-1809
- [7] Nicholas AP, Walling DE. The significance of particle aggregation in the overbank deposition of suspended sediment on river floodplains. *Journal of Hydrology*. 1996;**186**:275-293
- [8] Droppo IG. Suspended sediment transport-Flocculation and particle characteristics. In: Anderson MG, editor. *Encyclopedia of Hydrological Sciences*. New Jersey, USA: John Wiley & Sons, Ltd; 2005
- [9] Garcia-Aragón J, Droppo I, Krishnappan B, Trapp B, Jaskot C. Erosional characteristics and floc strength of Athabasca river cohesive sediments. *Journal of Soils and Sediments*. 2011;**11**(2):679-689
- [10] Khelifa A, Hill PS. Models for effective density and settling velocity of flocs. *Journal of Hydraulic Research*. 2006;**44**(3):390-401
- [11] Maggi F. The settling velocity of mineral, biomineral, and biological particles and aggregates in water. *Journal of Geophysical Research, Oceans*. 2013;**118**(4):2118-2132
- [12] Maggi F, Tang FH. Analysis of the effect of organic matter content on the architecture and sinking of sediment aggregates. *Marine Geology*. 2015;**363**:102-111
- [13] Watten BJ, Beck LT. Comparative hydraulics of rectangular cross flow rearing unit. *Aquaculture Engineering*. 1987;**6**:127-140
- [14] Summerfelt SG, Wilton G, Roberts D, Rimmer T, Fonkalrsrud K. Developments in recirculating systems for arctic char culture in North America. *Aquacultural Engineering*. 2004;**30**:31-71
- [15] Timmons M.B., Summerfeld S.T. y Vinci B.J. Review of circular tank technology and management. *Aquacultural Engineering* 1998;**18**:51-69
- [16] Garcia-Aragon JA, Droppo I, Krishnappan B, Trapp B, Jaskot C. Experimental assessment of Athabasca River cohesive sediment deposition dynamics. *Water Quality Research Journal of Canada*. 2011b;**46**(1):87-96
- [17] Li DH, Ganczarczyk JJ. Stroboscopic determination of settling velocity, size and porosity of activated sludge flocs. *Water Research*. 1987;**21**(3):157-262

- [18] Kranenburg C. The fractal structure of cohesive sediment aggregates. *Estuarine, Coastal and Shelf Science*. 1994;**39**:1665-1680
- [19] Garcia-Aragon JA, Salinas-Tapia H, Moreno-Vega J, Diaz-Palomarez V, Tejada-Vega S. A model for the settling velocity of flocs; application to an aquaculture recirculation tank. *International Journal of Computational Methods and Experimental Measurements*. 2014;**2**(3):313-322. DOI: 10.2495/CMEM-V2-N3-313-322
- [20] Johnson CP, Xiaoyan LI, Logan BE. Settling velocities of fractal aggregates. *Environmental Science & Technology*. 1996;**30**:1911-1918
- [21] Maggi F, Mietta F, Winterwerp JC. Effect of variable fractal dimension on the floc size distribution of suspended cohesive sediment. *Journal of Hydrology*. 2007;**343**:41-55
- [22] Jordan PR. Fluvial sediment of the Mississippi River at St. Louis, Missouri. USGS Water-Supply Paper No. 1802. <http://pubs.er.usgs.gov/djvu/WSP/wsp1802.djvu>. 1965
- [23] Scott CH, Stephens HD. Special sediment investigations: Mississippi river at St. Louis, Missouri, 1961–1963. 1966. USGS Water-Supply Paper No. 1819-J. <http://pubs.er.usgs.gov/djvu/WSP/wsp1819-J.djvu>
- [24] Li W, Wang J, Yang S, Zhang P. Determining the existence of the fine sediment flocculation in the three gorges reservoir. *Journal of Hydraulic Engineering*. 2015;**141**(2):05014008
- [25] Meade RH, Nordin CF, Curtis WF. Sediment in Rio Amazonas and some of its principal tributaries during the high water seasons of 1976 and 1977. In: *Proceedings of the III Simposio Brasileiro de Hidrologia (Brasília)*; Vol. 2; ABRH; Brazil; 1979. pp. 472-485
- [26] Meade RH. Suspended sediment in the Amazon River and its tributaries in Brazil, during 1982–1984. US Geol. Survey Open File Report 85-492. US Geol. Survey, Denver, Colorado, USA. 1985
- [27] Chien N, Wan Z. *Mechanics of Sediment Transport*. Reston, Virginia, USA: ASCE Press; 1999. p. 913
- [28] Vikram CS. *Particle Field Holography*. Cambridge, UK: Cambridge University Press; 1992
- [29] Satake S, Kunugi T, Sato K, Ito T. Digital holographic particle tracking velocimetry for 3-D transient flow around an obstacle in a narrow channel. *Optical Review*. 2004;**11**: 162-164
- [30] Sheng J, Malkiel E, Katz J, Adolf J, Belas R. Digital holographic microscopy reveals prey-induced changes in swimming behavior of predatory dinoflagellates. *Proceedings of the National Academy of Sciences*. 2007;**104**(44):17512-17517
- [31] Schnars U, Jüptner W. *Digital Holography: Digital Hologram Recording, Numerical Reconstruction, and Related Techniques*. Berlin Heidelberg: Springer; 2005

Edited by Daniela Malcangio

With the growth of urbanization, industrialization, and intensive agricultural practices, all superficial, inland, and marine water bodies have become the repository for large quantities of every type of substance extraneous to the natural aquatic environment. The knowledge of hydrodynamics becomes crucial in this context, as it is the driving mechanism for the movement and transport of these matters and of sediments that become collectors of these substances, in a surface water system. The best way to understand these natural processes is via examples and case studies. This book deals with practical studies of hydrodynamic processes through physical and numerical models. Researchers, together with practicing engineers, will find this book useful in making a rapid assessment of different environmental water body problems.

Published in London, UK

© 2018 IntechOpen
© dolnikow / iStock

IntechOpen

